Machining of Novel Devices with 3D Microstructures in Bulk Materials by Femtosecond Pulsed Laser Ablation

By

Yinggang Huang

A dissertation submitted in partial fulfillment of

the requirements for the degree of

Doctor of Philosophy

(Electrical Engineering)

at the

UNIVERSITY OF WISCONSIN-MADISON

2017

Date of final oral examination: August 11th, 2017

The dissertation is approved by the following members of the Final Oral Committee:
Hongrui Jiang, Professor, Electrical and Computer Engineering
Zongfu Yu, Assistant Professor, Electrical and Computer Engineering
Nader Behdad, Professor, Electrical and Computer Engineering
Xudong Wang, Associate Professor, Materials Science and Engineering
Wenxiao Pan, Assistant Professor, Mechanical Engineering

© Copyright by Yinggang Huang 2017

All Rights Reserved

Acknowledgments

This Ph.D. dissertation is the culmination of my research work over the past several years on the topics I am truly passionate about and could not have been accomplished without the help of many people.

First and foremost, I would like to express my deepest thanks to my Ph.D. advisor, Prof. Hongrui Jiang, for his continuous support and research guidance during the past few years. It has been my privilege to work under his supervision. His encouragement, talent, immense knowledge, integrity and enthusiasm have been the invaluable source for me to persevere despite the obstacles I encountered in my research while his insightful discussions and suggestions bolstered my confidence and inspired me tremendously for the experiments. He is the best mentor one could ever find.

I would like to extend my gratitude to other members of my dissertation committee, Prof. Zongfu Yu, Prof. Nader Behdad, Prof. Xudong Wang and Prof. Wenxiao Pan for generously offering their time for my defense and helpful suggestions for my dissertation.

I am also greatly indebted to my colleagues in the research group for the numerous inspiring discussions and technical assistance: Dr. Hewei Liu, Dr. Xi Zhang, Dr. Xuezhen Huang, Dr. Mohammad Moghimi, Dr. Jae-Jun Kim, Dr. Alireza Ousati Ashtiani, Dr. Aditi Kanhere, Dr. Hao Bian, Kari Van Grinsven, Xiudong Wu, Yousuf Al-Moallem, Jayer Fernandes, Yong Ho (Eric) Kwon. I particularly thank Dr. Hewei Liu for his instruction on the operation and maintenance of the femtosecond laser system and useful advice for my research experiments. I appreciate the time Yousuf Al-Moallem dedicated to my defense presentation practice.

This work would not have been possible without the assistance from other people and

research facility at the University of Wisconsin-Madison. I gratefully acknowledge use of instrumentation supported by NSF through the University of Wisconsin Materials Research Science and Engineering Center (DMR-1121288, 0079983 and 0520057) and the University of Wisconsin Nanoscale Science and Engineering Center (DMR-0832760 and 0425880). In addition, I am thankful to the Wisconsin Center for Applied Microelectronics (WCAM) and their staff members for training and granting me access to the cleanroom equipment. I appreciate the help from Xuan Zhang for the measurement work in the cleanroom for my SiC microfluidics project. Thanks to Richard Noll who was instrumental in training me for and troubleshooting problems with the various characterization tools such as SEM and FIB.

I am grateful for the funding sources as well that allowed me to pursue my doctoral study and research. My work was supported by the National Institutes of Health (Grant Number: 1DP2OD008678-01), the National Science Foundation (Grant Number: 1329481), College of Engineering at the University of Wisconsin-Madison, and Prof. Hongrui Jiang's Lynn H. Matthias and Vilas Distinguished Achievement professorships.

Moreover, the friendship is an indispensable part along my journey of the Ph.D. pursuit. I would like to thank all my friends who made my life at the University of Wisconsin-Madison an enjoyable one. They are the precious source of emotional support whenever I am distressed and perfect companions for out-of-lab activities. Some special thanks are given to my best high school classmate, Dr. Zheng Shen, who shed light on many issues I had in academics and life while he was also in the United States. I also thank Jiangnan Qu who lives in the United Kingdom for his friendship and encouragement over countless phone conversations. I give my gratitude to Erica F. Fleming, one of my best American friends, who passed away unexpectedly while on vacation. Her optimism, kindness, generosity, contagious smile and big heart to always put everyone else first

had the profound impact on me.

Last but certainly not least, I am eternally grateful to my family. It is unimaginable for me to achieve this milestone without the unparalleled support and unconditional love from my father, Chunhua Huang and my mother, Fenyun Jiang, who are my role models. I dedicate this dissertation to the memory of my grandmother, Xiu Zeng, who had passed away before this dissertation was completed. My grandmother was the first one who taught me basic arithmetic. The last words of this acknowledgment are reserved for my wife, Zhu Ding, and my daughter, Chelsea Ding Huang. The unwavering love, spiritual support and sacrifices from Zhu are vital for me to reach this point. The birth of Chelsea last year has brought immense happiness to me and my family and further motivated me to complete this dissertation.

Table of Contents

Acknowledgments i

List of Figures vi

Chapters

1. Introduction 1

- 1.1 Femtosecond Laser Ablation 1
  - 1.1.1 Overview of Physics of Pulsed Laser Ablation 3
  - 1.1.2 Introduction to Femtosecond Pulsed Laser 7
  - 1.1.3 Ablation Mechanism of Femtosecond Pulsed Laser 9
  - 1.1.4 Femtosecond Laser Sources 12
- 1.2 Femtosecond Laser Micromachining 15
  - 1.2.1 Background 15
  - 1.2.2 Experimental System 19
  - 1.2.3 Advantages of Femtosecond Laser Micromachining 21
  - 1.2.4 Applications 23
- 1.3 Chapter Overview 26
- 1.4 References 29

2. Fabrication of Through-Wafer 3D Microfluidics in Silicon Carbide Using Femtosecond Laser 40

- 2.1 Introduction 41
- 2.2 Experimental Details 43
  - 2.2.1 Fabrication of Microchannels and Vias on Bulk SiC Substrates 43
  - 2.2.2 Preparation and Characterization of the SiC Samples 45
  - 2.2.3 Measurement of Contact Angle on the SiC Surfaces 45
  - 2.2.4 Assembly and Characterization of the SiC Microfluidic Device 45
- 2.3 Results and Discussion 47
  - 2.3.1 Comparison of Machining Microstructures in Air and DI Water 47
  - 2.3.2 Influence of Laser Parameters on Ablation Rate 49
  - 2.3.3 Wettability of the Femtosecond Laser-Ablated Surface 54
  - 2.3.4 Control of Cross-Sectional Shape of Microchannels 56
  - 2.3.5 Fabrication of Microchannels and Via Holes on SiC 59
  - 2.3.6 Z-Shaped Through-Wafer Microfluidic Device 60
- 2.4 Conclusion 62
- 2.5 References 63

3. Lateral Dye-Sensitized Microscale Solar Cells via Femtosecond Laser Patterning.... 68

3.1 Introduction 69
3.2 Fabrication and Sample Morphology 73
3.3 Results and Discussion 80
3.4 Conclusion 83
3.5 References 84

4. Artificial Eye for Scotopic Vision based on Bioinspired All-Optical Photosensitivity Enhancer with Super-Resolution Image Reconstruction Technique 86

4.1 Introduction 87
4.2 Structures of the artificial eye, BPE and μ-PCs 90
4.3 Device Performance 93
4.3.1 Visible Spectral Response 93
4.3.2 Imaging Results 94
4.3.3 Iterative-Back-Projection (IBP) Super-Resolution for High-Resolution Image Reconstruction 98
4.3.4 Image Quality Assessment Based on the Method of Structural Similarity (SSIM) Index 104
4.4 Conclusion 107
4.5 References 108

5. Conclusion and Future Work 110

5.1 Conclusion 110
5.2 Future Work 112

Appendix A: Matlab Code for the Main Program Reconstructing the High-Resolution Images Shown in Figure 4.13 114

Appendix B: Matlab Code that Implements Iterative-Back-Projection Super-Resolution Algorithm 117

List of Figures

Figures

1.1 Pulse width, peak power, and peak-to-peak time of periodic laser pulses 3

1.2 A schematic diagram for the steps of chirped pulse amplification (CPA) technique 9

1.3 Laser ablation craters in a 100 µm thick steel foil with (a) 200 fs, 780 nm and 120 µJ; and (b) 3.3 ns, 780 nm and 1 mJ laser pulses 11

1.4 Photon absorption mechanisms in solid materials with band gap by (a) single photon absorption and (b) multiphoton absorption 12

1.5 CPA-Series Ti:Sapphire Ultrashort Pulse Laser from Clark-MXR, Inc 13

1.6 A simple illustration of an erbium-doped femtosecond fiber laser 14

1.7 Diagram of the operation principle of Electrical Discharge Machining (EDM) process 18

1.8 Schematic diagram of an example experimental setup of the fs laser micromachining system. HWP denotes half-wave plate; P denotes polarizer; R denotes reflector 21

2.1 Schematic diagrams of the femtosecond laser micromachining. (A) Optical setup of the laser micromachining system. (B) Laser scanning strategy for the surface channel. (C) Laser scanning strategy for the via hole 44

2.2 Structural design of the Z-shaped microfluidics on SiC. (A) Schematic diagram of the microfluidic device. (B) Dimensions of the microchannels and via hole on the SiC substrate 47

2.3 Surface SEM images of microchannels with cross-sectional shape of semicircle and diameter of 100 µm with the parameters of scanning speed of 2 mm/s and pulse energy of ~2.23 µJ in (A) Air. (B) Deionized water 48

2.4 Surface SEM images of through-wafer via microstructures with diameter of 125 µm and

parameters of scanning speed of 2 mm/s and pulse energy of ~2.23 μJ in (A) Air. (B) Deionized water 49

2.5 Cross-sectional SEM images for trenches formed by fs laser in DI water with scanning speed of 1 mm/s and pulse energy 4.32 μJ using objective lenses of (A) 20X. (B) 100X 50

2.6 Optical images for the ablated grooves with different pulse energy and scanning speed. (from top to bottom: 0.83 μJ, 1.40 μJ, 2.23 μJ, 3.17 μJ, 3.80 μJ, 4.32 μJ; from left to right: 0.1 mm/s, 0.5 mm/s, 1 mm/s, 2 mm/s, 5 mm/s, 10 mm/s, 20 mm/s) 51

2.7 Dependence of the femtosecond laser ablation width and depth on the laser pulse energy (A) and scanning speed (B) 53

2.8 Ablated feature after a single ablation with different pulse energy and scanning speed. (A) Pulse energy: 4.32 μJ; speed: 20 mm/s. (B) Pulse energy: 1.4 μJ; speed: 0.5 mm/s 54

2.9 Surface morphology of SiC substrate (A) before and (B) after laser ablation. Inserts in (A) and (B) show the contact angle of mineral oil measured on the SiC surfaces 55

2.10 (A)–(C) Surface images of the microchannels with rectangular, triangular, and semicircular shapes, respectively. (D)–(F) Cross-sectional images of the microchannels with rectangular, triangular, and semicircular shapes, respectively. (G)–(I) Steady-state cross-sectional velocity profiles of microchannels with rectangular, triangular, and semicircular shapes, respectively ...58

2.11 Fabricated surface microchannels and via hole on the SiC substrates. (A) and (B) Optical microscopic and SEM images of a Y-shaped microchannel, respectively. (C) Cross-sectional image of the via hole. (D) and (E) Top- and bottom-view SEM images of the via hole, respectively 60

2.12 Z-shaped microchannel device demonstrated with mineral oil flowing with red fluorescent dye. (A) Photo of the Z-shaped microchannel device. (B) Image of the microchannels and via

hole on the SiC substrate. (C) and (D) Images of the mineral oil flow with red fluorescent dye for bottom and top channels, respectively 61

3.1 a) Conventional sandwich-structured DSSC, b) lateral DSSC with patterned PE (−) and CE (+), c) monolithic back-contact DSSC, d) back-contact DSSC with patterned CE, e) lateral DSSC with hierarchical PE and CE. Photogenerated positive and negative charges are shown in each structure 72

3.2 Schematics of the fabrication process of the lateral DSSC: a) nanostructured TiO_2 film deposited on FTO glass, b) TiO_2/FTO patterned by femtosecond laser ablation, c) electrodeposition of Pt on CE fingers, d) dye-loading on PE fingers, e) electrolyte filling and device sealing. f) SEM image of the tilted top view of the laser-patterned TiO_2 film, where the widths of patterned fingers are labeled 74

3.3 Microscopic image of laser-patterned TiO_2 film on FTO glass with CE deposited with Pt for lateral DSSC 75

3.4 a) Cross-sectional SEM image of laser-patterned TiO_2 film, where CE fingers are deposited with Pt. Cross-sectional and top view images of one ablation channel are shown in b,c), respectively. d) Top view SEM image of patterned TiO_2 film with Pt, where the line-scanning curve of EDS is shown, with the atomic ratio of Pt/Ti as the y-axis. After the laser ablation process, the Pt and organic dye were loaded to CE and PE electrodes, respectively 76

3.5 XRD spectra of nanostructured TiO_2 film before and after laser ablation with pulse energy of 4.2 μJ 77

3.6 Effect of different laser pulse energy (4.2 μJ pulse vs. 3.4 μJ pulse) on the width of the ablated channels (a) & (b), Pt deposition (c) & (d) for 4.2 μJ and 3.4 μJ, respectively and (e) resultant performance of the two lateral DSSCs 79

3.7 a) J–V curves and b) IPCE spectra of a conventional DSSC and a lateral DSSC with back incident light 82

4.1 Schematic illustrations of (A) An apposition compound eye, (B) A superposition compound eye. (C) A superposition eye with misaligned optics 88

4.2 Schematic illustrations and images of a natural eye of elephantnose fish and an artificial eye. (A) Illustrations of the anatomical structure of the elephantnose fish eye and a crystalline cup in the retina (Inset). (B–D) Images of the artificial eye, its front view, and the BPE on the rear side, respectively. (E) Exploded illustration of the artificial eye. (Inset, Right) The structure of μ-PCs is shown 89

4.3 Schematic of the design of the artificial eye. (A and B) 3D layout of the artificial eye 91

4.4 Surface SEM image of a part of fabricated BPE indicating high-quality micromachining by fs laser ablation 92

4.5 Multiplication of light intensity M (blue dots) at wavelengths ranging from 380 to 900 nm. The red line is obtained by a cubic polynomial fit 94

4.6 The image of the original distortion-free image of Bucky badger 95

4.7 Four raw images obtained by CCD sensor with the BPE applied to the upper-left, upper-right, bottom-left and bottom-right parts of Bucky, respectively 96

4.8 (left) Combined image from the 4 raw images; (middle) Processed image by taking the maximum gray value in every block of 14x14 pixels of the left image as a single pixel, and then stitching them together; (right) simply zoomed-in middle image 97

4.9 Observation model of the super-resolution image reconstruction 99

4.10 Flow chart of the iterative super-resolution reconstruction algorithm used 100

4.11 Schematic illustration of the image acquisition process 101

4.12 (a) 16 LR images, resolution: 96 x 96; (b) Sub-pixel displacement (x, y) for each LR image (unit: pixel) 102

4.13 HR images with resolution of 384 x 384 obtained from the IBP super-resolution algorithm based on the initial guesses of (a). blank image; (b). expanded first LR image; (c). average of the 16 expanded LR images 104

4.14 SSIM index maps and their average SSIM values using the original distortion-free image as the reference for the HR images obtained by IBP super-resolution algorithm with the initial guesses of (a). completely blank image; (b). expanded first LR image; (c). average of the 16 expanded LR images 106

CHAPTER 1. Introduction

1.1 Femtosecond Laser Ablation

Laser ablation (LA), in the broadest sense, is the process of removing material from a target sample by irradiating it with a focused laser beam. It is more common to utilize pulsed lasers for the LA although it is possible to accomplish ablation with continuous wave (CW) lasers if the intensity is high enough [1]. The ablation process is achieved by the interaction of the laser and target material in which the photon energy is absorbed and then converted to thermal or photochemical energy. The ablation is activated above the threshold laser fluence that depends on various factors such as target material properties, photon absorption mechanism, surface morphology as well as the laser parameters, e.g. wavelength and pulse width. The threshold may also decrease due to defect activated ablation when the irradiated zone is affected with an extended period of time. The amount of materials removed also depends on the laser fluence, pulse duration, number of pulses applied, laser wavelength, and the material properties of the target sample. In general, the material removal depth per pulse can be estimated by laser fluence and absorption coefficient and is governed by the Beer-Lambert's law [2]:

$$D_{abl} = \alpha^{-1}\ln(\frac{F_l}{F_{th}}) \tag{1.1}$$

where D_{abl} is the ablation depth per pulse, α is the absorption coefficient of the target material, F_l is the actual laser fluence applied, and F_{th} is the threshold laser fluence.

Albeit the dependence of ablation mechanisms on the inherent material property and laser source parameters, laser fluence and pulse duration have been widely used to gauge the distinct material removal characteristics. Thermal energy plays the crucial role when the pulse duration is

long enough regardless of the value of laser fluences above the ablation threshold. The irradiated zone of target material typically evaporates or sublimates at relatively low laser flux and may alter the composition of existing material if it consists of multiple substances. At high laser flux, swift movement of vapor bubbles and the phenomenon of nucleation generate chunks and fragments from the target [3]. In the case that the pulse width is short enough so that the surrounding area of laser affected zone (LAZ) is not thermally affected, photochemical ablation process, such as Coulomb explosion, becomes dominant. In this regime, direction ionization plays the major role that generates bright plasma resulting in chemical bond breaking and removal of ions due to Coulomb repulsion from the sample surface followed by the ballistic removal of neutral particles on the ultrashort (e.g., ~picosecond for semiconductors) time scale [4]. In the ablation process, whether in air or liquid-assisted environment, an apparent plume can be observed in the region with the laser irradiation that may contain the removed fragments from the target material. At high laser flux, most of the fragments are directly ionized, therefore the plume is represented by the bright plasma. After the absorbed energy is released or dissipated, the material pieces in the plume solidify and then nanoparticle clusters form on the surface. In the case that the target material is ablated in liquid, the by-product of nanoparticles may float onto the liquid surface and the cleaner surface after the processing is obtained.

As a matter of fact, the interaction of laser and target material is complex and can include surface melting and thermally related processes in addition to the ablation, that causes irreversible changes to the sample surface morphology, texture, chemical structure and composition. However, under some processing conditions for the given material, some material removal mechanism becomes dominant. Therefore, precise control of final processed features and structures and thus the desired properties can be accomplished if appropriate laser parameters and ablation

environment are used.

1.1.1 Overview of Physics of Pulsed Laser Ablation

Laser ablation usually refers to removing material with a pulsed laser beam due to the high peak power and significantly reduced thermal effects induced. The typical pulse duration is in the range of naonosecond (~10^{-9} s) to femtosecond (~10^{-15} s), and this laser parameter has a significant effect on the ablation mechanism. Ultra-short pulsed laser with duration of several picoseconds or femtoseconds in general has no effect on the lattice since the removed material in the irradiated zone has less time to transfer the energy to its surrounding area hence the thermal effect is minimal. As a result, the irradiated zone is precisely defined with given laser parameters and material properties since the heat affected zone is greatly limited [5]. However, the longer pulse length that exceeds the target material's thermal relaxation time (~ nanoseconds) generates residual thermal energy that is spread to the surrounding area of the irradiated zone leading to low-quality ablation. Figure 1.1 illustrates the pulse duration, peak power intensity and the peak-to-peak time that is inverse of the pulsed laser repetition rate. Pulse width is defined as the duration of the pulse at full width at half maximum (FWHM).

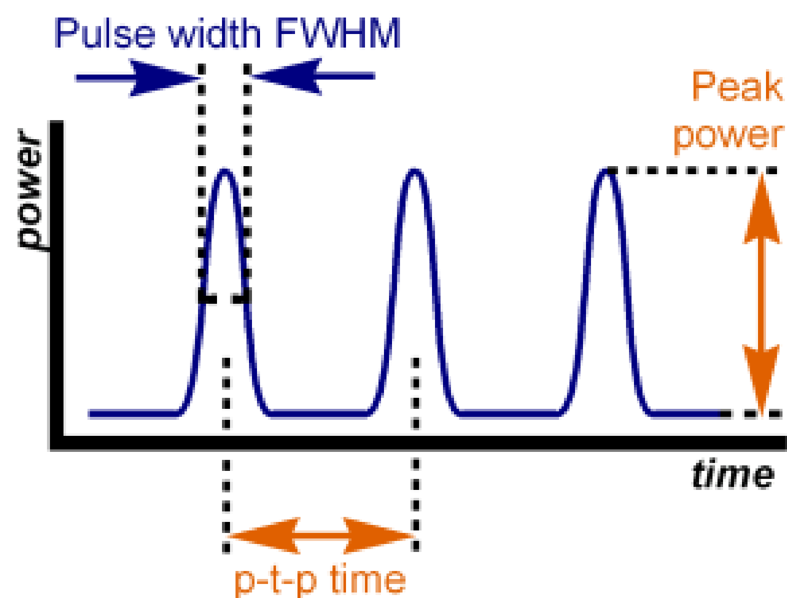

Figure 1.1 Pulse width, peak power, and peak-to-peak time of periodic laser pulses [6]

While the laser and solid material interaction is complicated, it generally involves the following steps. First the laser energy with photons of which the energy is above the material's band gap (unless impurity states or multiphoton absorption exist) is absorbed by free electrons due to inverse bremsstrahlung [7], then the thermalization within the electrons and energy transfer to the lattice occur followed by the phonon energy loss with the heat dissipated in the target material. With the assumption of fast thermalization in the electrons, electron temperature T_e and lattice temperature T_i, the energy from the laser to the target sample can be determined by the one dimensional, two-temperature diffusion model [8]:

$$C_e \frac{\partial T_e}{\partial t} = -\frac{\partial Q(z)}{\partial z} - \gamma(T_e - T_i) + S \tag{1.2}$$

$$C_i \frac{\partial T_i}{\partial t} = \gamma(T_e - T_i) \tag{1.3}$$

$$Q(z) = -k_e \left(\frac{\partial T_e}{\partial z}\right) \tag{1.4}$$

$$S = I(t) A \alpha e^{-\alpha z} \tag{1.5}$$

where z is the direction perpendicular to the target sample surface, Q(z) is the heat flux along z, S is the laser heating source term, I(t) is the laser intensity, A is the target surface transmissivity, α is absorption coefficient of the target sample, C_e and C_i are the heat capacities per unit volume of the electron and lattice subsystems, respectively, γ is the term describing the electron-lattice coupling, and k_e is the electron thermal conductivity.

As can be seen, the first two equations describe the cooling characteristics over time for electrons and lattice, respectively, that is responsible for the phonon energy transfer and is related to the material's inherent thermal property [9]. Rearrange the equations (1.2) – (1.4), the following equation can be obtained:

$$C_e \frac{\partial T_e}{\partial t} = k_e \left(\frac{\partial^2 T_e}{\partial z^2}\right) - C_i \frac{\partial T_i}{\partial t} + I(t)A\alpha e^{-\alpha z} \tag{1.6}$$

Electron heat capacity is much smaller than that for the lattice, and thus the electron cooling time that is proportional to its heat capacity is much less than the lattice thermal response time. The laser pulse width with its relation to the electron and lattice thermalization time has a major impact in the underlying ablation mechanism. With the typical range of electron and lattice heating times for solid materials, the three distinct regimes in terms of the laser pulse duration for different ablation dynamics can be defined: nanosecond, picosecond and femtosecond [8].

Nanosecond Pulsed Laser

Pulsed laser in the nanosecond scale has been used in various applications such as nanomaterial fabrication [10, 11] and material ablation [12]. For materials with long thermalization time such as certain polymers and bio-materials, photochemical ablation can be achieved with nanosecond pulsed lasers with negligible heat affected zone [13]. However, nanosecond pulses are too long to yield high-quality features on materials such as metals, most semiconductors. In such case, the electrons and lattice will reach the same temperature, i.e. $T_e = T_i = T$ since the laser pulse is much longer than the lattice heating time ($\tau_p >> \tau_i$) [14], therefore Eq. (1.6) can be reduced and rewritten as

$$C_i \frac{\partial T}{\partial t} = k_e \left(\frac{\partial^2 T}{\partial z^2}\right) + I\alpha e^{-\alpha z} \tag{1.7}$$

where $I(t) = I_0$ is constant, $I = I_0 A$.

In the regime of nanosecond pulses, the laser irradiated zone and its immediate surrounding area are heated and then melted leading to material vaporization, hence most energy is lost in form of heat spread into the sample. In addition, the overall ablation penetration depth is largely determined thermally rather than optically [15]. The melted layer on the sample surface will form as the phonon energy transfers to other areas [8] which makes nanosecond laser not suitable for

applications demanding high-resolution and precise features [15].

Picosecond Pulsed Laser

Ablation process with picosecond pulsed lasers (1-100 ps) lies in the transitional state from thermally activated material removal with nanosecond pulses to direct multiphoton ionization based damage with femtosecond pulses. In this regime, it is assumed the laser pulse width is between the electron and lattice thermalization times, i.e. $\tau_e << \tau_p << \tau_i$, therefore most of the photon energy is absorbed by the electrons with only small amount of thermal energy transfer into the lattice. Unlike the case of nanosecond laser, the electron temperature is greater than the lattice temperature in this regime. Due to the fact that electron thermalization time is much shorter than pulse width, electrons reach a thermal equilibrium, hence the Eq. (1.6) can be rewritten as [8]

$$k_e\left(\frac{\partial^2 T_e}{\partial z^2}\right) - \gamma(T_e - T_i) + I\alpha e^{-\alpha z} = 0 \tag{1.8}$$

$$T_i = \frac{1}{\tau_i}\int_0^t T_e(\theta) e^{-\frac{t-\theta}{\tau_i}} d\theta + T_0 \tag{1.9}$$

where $T_0 = T_e(0)$ is the initial temperature.

When also considering the condition of $t << \tau_i$, i.e. the pulse width much shorter than the lattice thermal relaxation time, Eq. (1.9) can be further simplified due to the quasi-stationary state of the electron temperature. Furthermore, neglecting the constant T_0, we obtain [8]

$$T_i \approx T_e\left(1 - e^{-\frac{t}{\tau_i}}\right) \approx \frac{t}{\tau_i} T_e \tag{1.10}$$

In the picosecond scale, the electron temperature is much higher than that of the lattice, hence the lattice temperature T_i in Eq. (1.8) is negligible. If the electron cooling is caused by the energy transfer to the lattice, i.e. $k_e T_e \alpha^2 << \gamma T_e$, then from Eq. (1.8) and (1.10), we obtain [8]

$$T_e \approx \frac{I\alpha}{\gamma} e^{-\alpha z}, \qquad T_i \approx \frac{F\alpha}{C_i} e^{-\alpha z} \tag{1.11}$$

Femtosecond Pulsed Laser

In the regime of femtosecond laser, the pulse duration becomes shorter than both the electron and lattice thermalization times, i.e. $\tau_p << \tau_e$ and $\tau_p << \tau_i$. In such situation, it is assumed that no electron-coupling occurs during the ablation process and thus the thermal energy transfer between the electrons and the lattice is negligible. Then Eq. (1.2) can be reduced to [8]:

$$C_e'\left(\frac{\partial^2 T_e}{\partial t^2}\right) = 2I\alpha e^{-\alpha z} \tag{1.12}$$

which yields

$$T_e(t) = \sqrt{T_0^2 + \frac{2I\alpha}{C_e'} t e^{-\alpha z}} \tag{1.13}$$

Since no thermal conduction into the target material occurs, the target temperature after the laser pulse ends can be described as [16]

$$T(z, \tau_p) = \frac{\alpha A F_L}{\rho c} e^{-\alpha z} \tag{1.14}$$

where F_L is the laser pulse fluence, ρ is the mass density of the target, c is the specific heat.

The ablation depth per laser pulse for femtosecond laser is given by [8, 17]

$$L \approx \alpha^{-1} \ln\left(\frac{F_\alpha}{F_{th}}\right) \tag{1.15}$$

where F_{th} is the laser fluence threshold and F_α is the applied laser fluence. As can be seen, ultrashort laser pulses has predictable ablation results compared with longer ones affected by various factors, indicating ultrashort pulsed laser is the better candidate for ablation with minimal collateral damage and precision micromachining.

1.1.2 Introduction to Femtosecond Pulsed Laser

Since the inception of the laser in the 1960s, the field of laser ablation has been growing rapidly. Traditionally nanosecond pulsed lasers were used extensively for various applications including ablation and microstructure machining, however, nanosecond pulses gradually are not

able to meet the demands of high-quality, high-resolution microstructure fabrication or precise cutting from such industries as microelectronics and biomedical sector due to the high thermal effect. Moreover, the peak intensity of traditional laser sources is not high enough for some applications requiring ultra-high power to ablate hard materials. This is where femtosecond (fs) pulsed laser comes into play.

A fs pulsed laser generates optical pulses with duration of less than 1 picosecond in the realm of femtoseconds (10^{-15} s) which is usually referred to as ultrashort pulses. Over the last two decades, the rapid development of fs lasers has spurred various new applications in science, research and industry. Unlike the nanosecond pulses, fs pulsed laser almost causes no thermal damage to the surrounding area of irradiated zone. For a given material, energy above its atom's binding energy must be applied in order to remove it, therefore it is required to generate higher peak intensity for shorter pulse width to remove same number of atoms from a given material. For instance, the laser intensity for a 200fs pulse should reach ~10^{13} W/cm^2 [18] to initiate the ablation process for fused silica whereas only ~10^8 W/cm^2 is required with 28ns pulses [19]. At such a high laser intensity, almost all atoms within the irradiated zone are ionized as soon as the laser beam is applied. The energy is then absorbed by the free electrons regardless of the target material properties making fs laser suitable for ablating almost any solid materials.

The increase of laser peak intensity reached its bottleneck for decades after the early development of the laser system. However, this problem was resolved by the groundbreaking invention of chirped pulse amplification (CPA) for lasers by Donna Strickland and Gérard Mourou at the University of Rochester in the mid-1980s [20]. With the technique of CPA, a laser pulse is first stretched in time by a large factor prior to sending it to a specifically designed gain medium where the stretched pulse with much lower intensity is again amplified by more than six orders of

magnitude [21]. In order to achieve ultrashort laser pulse with much higher peak intensity, the amplified laser pulse is recompressed back with equal pulse duration with the original one. A simple illustration of this process is shown in Figure 1.2.

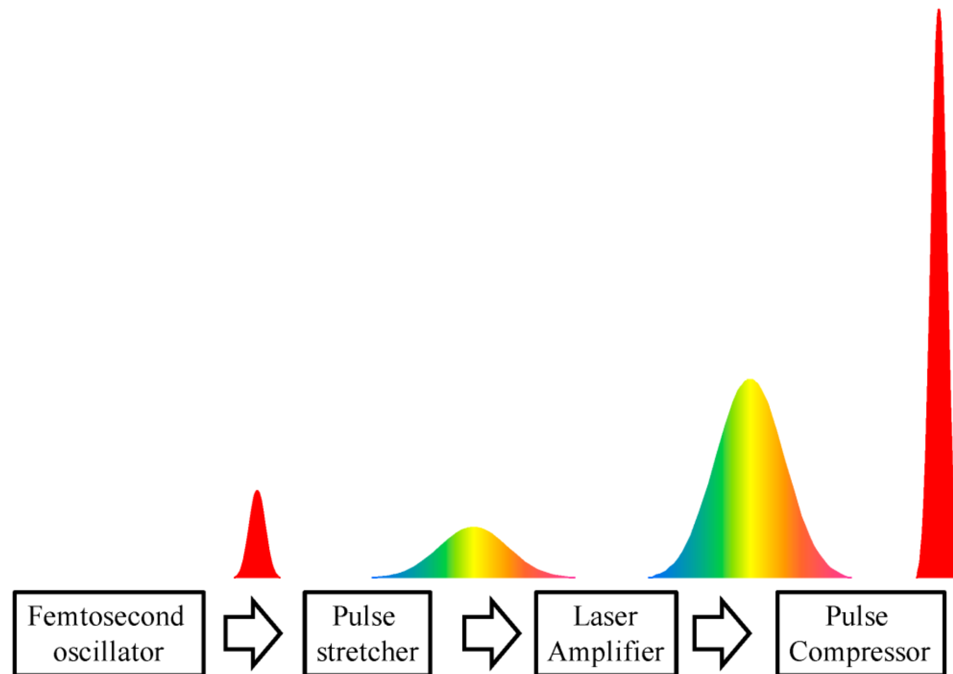

Figure 1.2 A schematic diagram for the steps of chirped pulse amplification (CPA) technique [22]

The fs laser system has been used widely in both research and industry and has been greatly improved over that last two decades giving rise to more cost-effective and user-friendly laser systems that can be controlled effortlessly by computers. It has been used in a plethora of applications that nanosecond lasers can or cannot achieve, including the nanoparticle preparation [23], thin film deposition [24, 25], machining of functional microstructures [26-28], and analytical chemistry [29].

1.1.3 Ablation Mechanism of Femtosecond Pulsed Laser

The material removal process from solids occurs when a pulsed laser with energy density higher than the ablation threshold is focused onto the sample surface. In the regime of nanosecond

pulses, the duration of pulses is too long so that the thermal energy is spread into the bulk, and the ablation process occurs simultaneously with the pulse. However, since the fs laser pulses are shorter than the electron and lattice thermalization times, the material removal typically occurs after the ultrashort pulses. In general, fs laser has the advantage of precise micromachining and minimal thermally induced damage. It can be thought that the light-matter interaction is frozen in the duration of an ultrashort laser pulse. At high laser intensity, fs laser ablation process is accompanied by a highly directed bright plasma above the irradiated zone that transforms from solid to vapor and plasma due to the extreme local temperature.

Depending on the value of laser intensity, fs laser pulses possess two ablation mechanisms, namely the Coulomb explosion that occurs quickly after the laser pulse and thermal vaporization that has long latency after the laser pulse applies [4]. When the fs laser has a relatively low intensity above the given target material's ablation threshold, Coulomb explosion is the main mechanism in which the outer valence electrons are excited by laser energy higher than the band gap, and then extracted from their atoms, leaving the positively charged ions. If the binding energy of ions is exceeded, the created electric field will extract the ions out of the target materials as well [30]. The ablation depth can be described as [31]

$$L = \delta \ln\left(\frac{F_a}{F_{th}^{Skin}}\right) \text{ where } \delta = \alpha^{-1} \text{ is the skin depth} \tag{1.16}$$

However, thermal vaporization dominates the ablation mechanism if the input laser intensity is much higher than the threshold, and the ablation depth can be described as [31]

$$L = l ln\left(\frac{F_a}{F_{th}^{thermal}}\right) \text{ where } l = \sqrt{D\tau_p} \tag{1.17}$$

l is called the electron thermal diffusion length, D is the thermal diffusivity, an intrinsic property of the target material, τ_p is the pulse width. The thermal diffusion length can be construed as the distance the energy can spread for a given target material with thermal diffusivity of D in the

duration of pulse irradiation.

Figure 1.3 (a) and (b) shows an example of comparison of craters processed by fs and ns laser pulses, respectively [30]. As can be clearly seen, the holes formed by fs laser ablation is much cleaner, smoother with well-defined edges, whereas the one processed by ns laser shows severe collateral thermal damage and irregularities around the crater due to the resolidification of splashed melt layers [8].

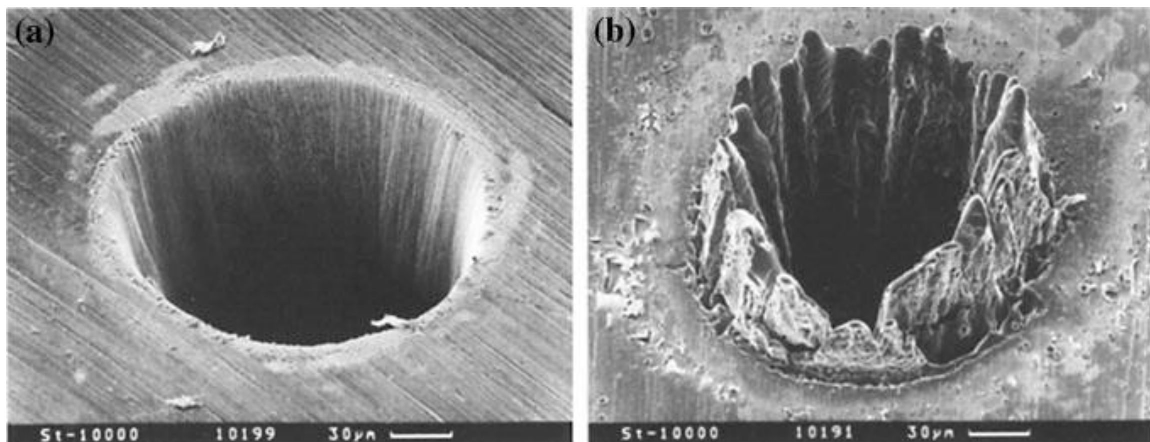

Figure 1.3 Laser ablation craters in a 100 µm thick steel foil with (a) 200 fs, 780 nm and 120 µJ; and (b) 3.3 ns, 780 nm and 1 mJ laser pulses [30]

The amount of laser energy needed to achieve the ablation process depends on the intrinsic properties of the target materials. For example, for metals, the optical absorption is usually achieved by the free electrons that abundantly exist. In semiconductors, the electrons absorb the energy and are excited to conduction band if the laser energy is greater than the band gap. Therefore, linear absorption (single photon absorption) is dominant in metals and semiconductors. In dielectrics, however, band gap is usually larger than the photon energy, therefore no energy absorption occurs in the stationary state, in such case nonlinear absorption such as multiphoton absorption of optical energy becomes the main mechanism [32]. Figure 1.4 (a) and (b) depict the single and multiphoton absorption processes in materials with band gap, respectively [33]. In

multiphoton absorption, multiple photons are absorbed by the material with band gap greater than the energy of a single photon resulting in the excitation of an electron which occurs when extremely high density of photons are incident on the target material simultaneously. It can be viewed as the electron being excited by photons via virtual states and eventually reaching the conduction band. This process can be easily realized by the fs laser pulses due to the ultra-high peak intensity.

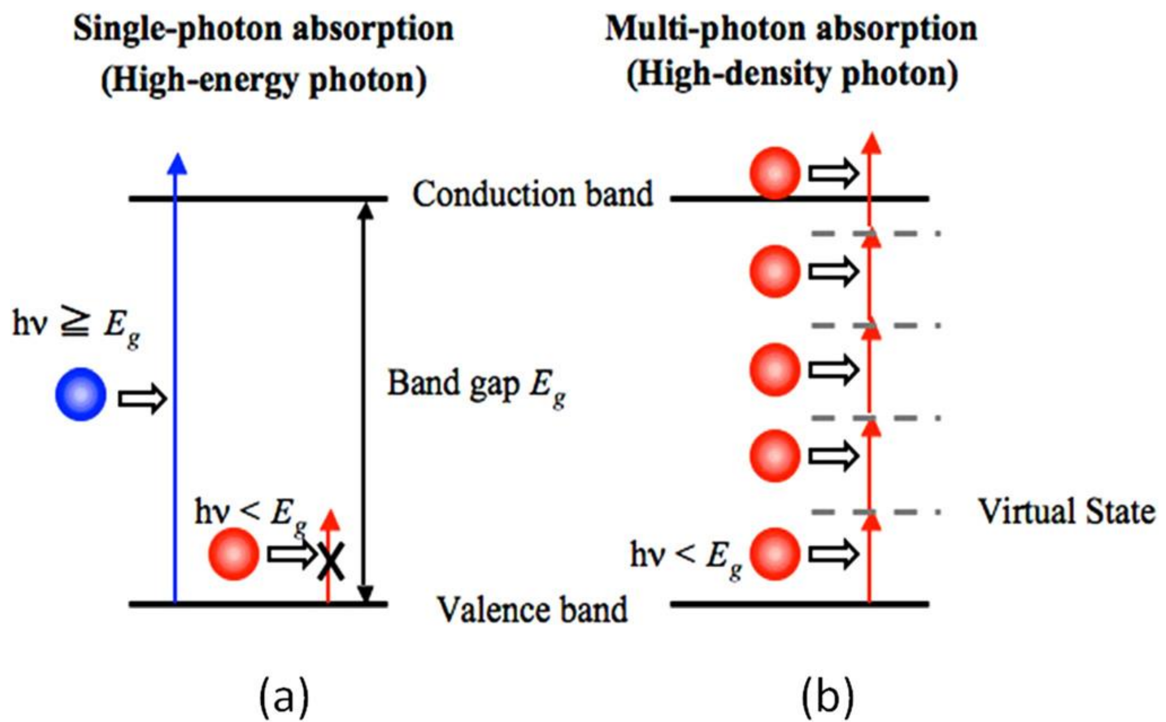

Figure 1.4 Photon absorption mechanisms in solid materials with band gap by (a) single photon absorption and (b) multiphoton absorption [33]

1.1.4 Femtosecond Laser Sources

Various types of laser sources for material processing have been developed for generating ultrashort laser pulses (less than several picoseconds), however, they can be broadly divided into

two groups: solid-state lasers and fiber lasers.

Solid-State Lasers

Solid-state pulsed lasers are used widely nowadays in laser cutting, welding, drilling, scribing and micromachining. The typical gain media used in solid-state pulsed lasers are Titanium-doped sapphire (Ti:Sapphire), Ytterbium-doped yttrium aluminum garnet (Yb:YAG), Ytterbium-doped potassium gadolinium tungstate (Yb:KGW), Ytterbium-doped potassium yttrium tungstate (Yb:KYW).

Ti:Sapphire is a common transition-metal doped gain medium with broad spectra for fs pulsed lasers. Since it was invented in 1986 [34], it has gained popularity in the application of ultrashort laser pulse generation and is the most common material for making commercial tunable lasers in the range of 660nm to 1180nm [35]. Ti:Sapphire is capable of generating pulses of several femtoseconds through Kerr-lens modelocking and has high saturated fluence. The other three types of solid-state lasers are relatively more compact and more cost-effective. The Figure 1.5 shows an example of Ti:Sapphire ultrashort pulsed laser system which has relatively large size [36].

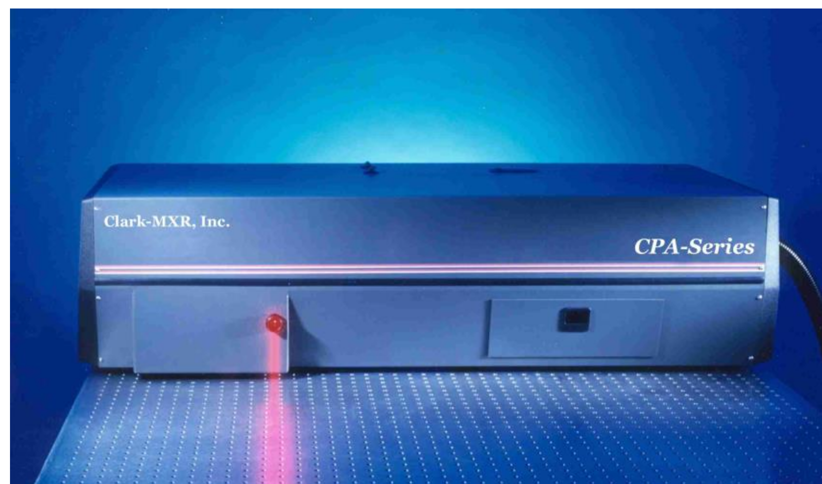

Figure 1.5 CPA-Series Ti:Sapphire Ultrashort Pulse Laser from Clark-MXR, Inc [36]

There are also some other improvements to the components of solid-state lasers that offer

many advantages. For example, Saturable absorber mirrors based on quantum dots (QD's) were developed with short-time response leading to higher repetition rates [37], and the saturable absorbers have been made of carbon nanotubes [38] and graphene [39] enabling broad wavelength range to mid-infrared regime.

Fiber Lasers

Fiber laser has also been widely used in research and industry since the early research in this field in 1980s, due to the advantages of small size, high stability, fast heat-dissipation capability and possibility of pumping with laser diodes. At early days Er^{+3} ions were typically used as the dopant for the silica fibers with working wavelength of 1.55 µm which is a good candidate in the telecommunication applications, however more rare elements such as Yb^{+3} [40] and Ho^{+3} [41] have also been used in fibers with different working wavelength. Either active or passive mode locking is employment to generate the fs pulse lasers. The commercially available Yb-doped-based fiber lasers with silica fibers as the gain media has the wavelength of around 1.03 µm.

A simple type of Er-doped fiber laser is shown in Figure 1.6 [42]. The initial low-intensity laser is generated from the semiconductor laser diode, a saturable absorber mirror is placed before the dichroic coupler as a passive mode locker. Then the laser is pumped by the erbium-doped fiber and eventually is transmitted out of the doped fiber as the output.

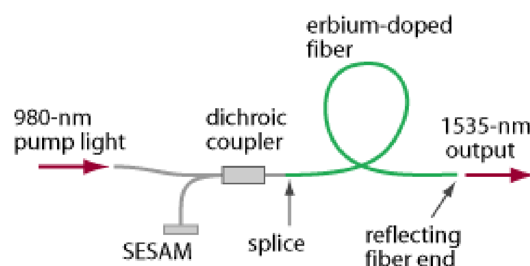

Figure 1.6 A simple illustration of an erbium-doped femtosecond fiber laser [42]

1.2 Femtosecond Laser Micromachining

Laser micromachining is one of the prominent applications of pulsed laser ablation that revolutionized the precision manufacturing industry. It is a contactless and direct-writing technique in which a laser beam is focused on a target sample usually placed on a motion stage. The laser beam can be focused into the material if it is transparent for the given laser wavelength. With the precise control of the movement of the motion stage, the irradiated area is either removed or influenced with material properties altered therefore the desired features are achieved. In contrast to most other micromachining methods, short pulsed laser micromachining is an ideal candidate in applications demanding ultra-precise defined patterns, flexibility in machining of 3D structures and choice of target materials as well as minimal impact to the environment.

Femtosecond (fs) laser micromachining, also referred to as ultrashort pulsed laser micromachining (pulse duration $\tau_p < 1$ ps), has drawn tremendous attention from scientists and manufacturing industry. As mentioned in Section 1.1.3, fs laser ablation results in high-quality, clean features whereas the nanosecond counterpart induces apparent thermal damage on the edges which is attributed to their ablation mechanisms. With CPA technique, the amplified laser pulses are re-compressed back to the fs regime making the pulse peak power reach the order of petawatts (10^{15} W). With such high peak power and thus photon density, the ablation process can be initiated for almost any solid materials via either linear or nonlinear absorption.

1.2.1 Background

It is not a secret that our daily life has intertwined with high-tech products such as smart phones, tablets and GPS navigation systems. These devices cannot function without their numerous components, for example CPU, wireless network adapters, accelerometers, motion sensors and so on. Due to the trend of compact electronic devices, miniaturization of all these

components is inevitable leading to rapid development of micro- and nanotechnology. In fact, the micro-components are not only utilized in the handheld personal electronic devices, but also in equipments of all sizes demanded by scientific research and industry. In addition to the conceptualization and design of the aforementioned components, it is imperative to develop suitable manufacturing techniques in order to realize the actual products. While manufacturing techniques such as photolithography, chemical etching etc. are used extensively in the microelectronic device manufacturing, they become infeasible in the manufacturing application of critical components with complex 3D structures. As a result, various micromachining approaches have been conceived and developed to meet this demand that that are the foundation for Micro-Electro-Mechanical-Systems (MEMS).

Conventional micromachining usually refers to micro-cutting technique via turning, milling or drilling with a cutting chip harder than the intended target materials installed on a precision cutting machine [43]. The main feature of the conventional micromachining techniques is that the cutting tool has the physical contact with the workpiece and they have been used to cut various materials including copper [44], stainless steel [45] and silicon [46]. While these direct-contact machining methods are still used in some applications due to the advantages of low cost and simple setup, they are posing some challenges. The brute force and thus mechanical pressure on the target material induced by the cutting tool can cause wear or even crack in the surrounding area of cutting zone to certain hard and brittle materials. Furthermore, the cutting mechanism determines that they are not appropriate when machining materials harder than the cutting tools.

In contrast, unconventional micromachining techniques achieve the material removal by means such as electrical, optical, thermal, chemical and mechanical energy rather than physical contact force with the machining tools. While the tools employing these techniques are usually

much more costly than conventional ones, the advantages of less contact-induced crack and wear, and the versatility in machining wider range of materials justify their usage. Examples of some widely used techniques are electron-beam machining that removes the affected area of the target material by a flux of high-speed electrons thereby generating heat and vaporizing the sample [47], photochemical machining that is a chemical mill process with the help of UV-sensitive material to etch target materials [48], and water jet machining that utilizes a jet of water with high speed and pressure to shape the target samples [49]. In addition, Electrical Discharge Machining (EDM) and Electrochemical Machining (ECM) are also two unconventional machining techniques capable of processing most hard materials that electrically conductive.

In EDM, electrical energy in electrode is used to generate sparks that in turn induces thermal energy that eventually the affected zone in the target materials is washed away by the dielectric fluid. Figure 1.7 illustrates the basic setup of an EDM machining system [50]. The workpiece is placed on the table of the machine tool and the electrode is installed as the tip of the tool. An automated motion stage can precisely position the electrode so that the desired work zone is placed near the electrode. During the operation, the sample is placed directly below but never touches the electrode followed by an electrical spark to transfer from electrode to the material via ionization of the dielectric fluid.

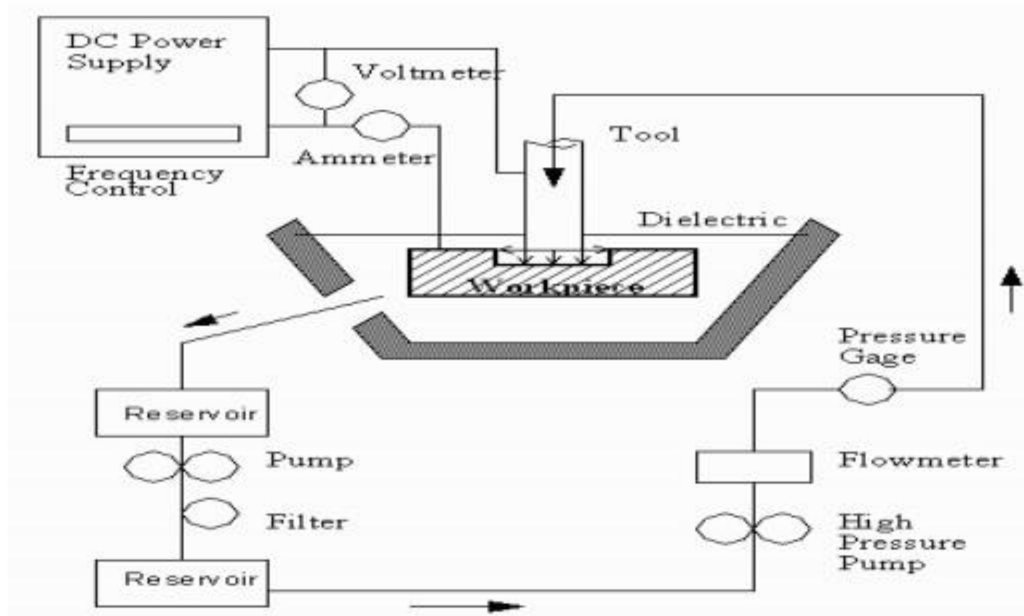

Figure 1.7 Diagram of the operation principle of Electrical Discharge Machining (EDM) process [50]

The ECM works similarly as the EDM in that strong current is passed from the tool to the workpiece through the electrolytic material followed by the dissolution of the target material locally. The electrolyte, generally a concentrated salt solution, is pumped at high speed through a gap to remove the debris and dissipate the generated heat [51]. The advantages of ECM compared with EDM are minimal thermal or mechanical stresses applied on the workpiece and less tool wear, hence high-quality surface finish can be accomplished.

The techniques described above rely on the electrical power to achieve the material removal. While there are extensive applications with these machining methods, drawbacks still exist due to the inherent working mechanism based on the electron system. Due to the heat generated by the electron beams, the heat affected zone (HAZ) is still considerable (several microns or more) in the realm of ultraprecision micromachining. Moreover, as charged particles, electrons inevitably induce, although small in macroscopic view, attractive or repulsive forces

described by Coulomb's Law which may negatively affect the results required by ultraprecision micromachining as well. Consequently, recently more research has been directed toward photon-based micromachining scheme, i.e. pulsed lasers, that ameliorates those problems substantially. The options of pulsed lasers are highly flexible in the range of wavelengths (UV to IR), pulse duration (fs to ms), peak power (up to petawatts) and pulse repetition rates (one pulse to MHz) which should be considered thoroughly for desired applications.

Femtosecond laser micromachining has emerged as a powerful method for advanced material processing and remains the laser machining technique with the shortest pulses on the market. It was first demonstrated in micromachining structures on fused silica [52]. As explained in Section 1.1.3, the nonlinear absorption process due to high peak pulse intensity and the minimal collateral damage due to ultrashort pulse width make it the ideal choice for ultraprecision ablation and micromachining any solid substance, despite its relatively lower speed of removing bulk materials. In the past two decades, it has been used to manufacture novel devices and structures in a wide range of applications in photonics, electronics, biomedical, micro- and nanofluidics among many others.

1.2.2 Experimental System

The tools and components used in a femtosecond laser machining system are quite delicate and sensitive to the ambient environment, therefore it is indispensable to carefully choose, install and tune them in the correct way. In addition, in order to meet the goal of high-quality micro-manufacturing for desired materials, it is mandatory to pay meticulous attention of various laser parameters as well such as wavelength, average power, repetition rate, laser fluence, pulse duration, laser beam focus. During the operation of machining process, the relative moving speed

between sample and the laser beam is also a crucial factor for the quality of the final structures.

Figure 1.8 shows an example of experimental setup for the fs micromachining system [53]. The output of fs laser source travels through the half-wave plate shifting its polarization direction by 90°, then the polarizer selecting only laser light with predefined polarization followed by a pulse shaper that manipulates the pulse shapes. These 3 components are used in applications requiring specific polarization and pulse shapes and are not the required components for the most basic machining system. The laser beam is then directed to a dichroic mirror that has high transmittance for the fluorescence light, but high reflectance for the fs laser beam. Therefore, the lamp light with sample imaging information can be transmitted up to the CCD enabling us to monitor the machining process on a computer screen, whereas the laser beam is mostly reflected and directed toward sample surface. An objective lens with some magnification and aperture is used to tightly focus the laser beam to further increase the power density. Depending on the desired micromachining environment, a vessel may or may not be needed. It is usually placed to accommodate the target sample immersed in a liquid, i.e. the liquid-assisted laser micromachining that could clean the ablated debris and/or induce chemical effect on the sample material. To maintain the continuous ablation on the workpiece, a positioning stage on which the sample or sample holder is placed should be employed that can move the workpiece in different directions. The stage is usually manipulated by a multiple-axis motion controller connected to a computer to achieve automation by software programs which enables micromachining with possibility of various structures restricted merely by imagination.

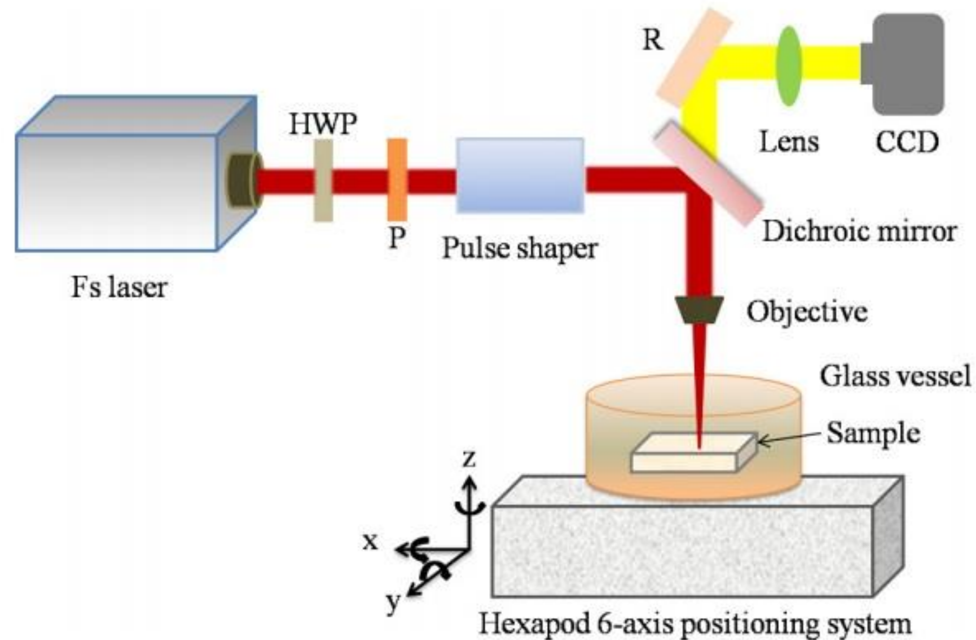

Figure 1.8 Schematic diagram of an example experimental setup of the fs laser micromachining system. HWP denotes half-wave plate; P denotes polarizer; R denotes reflector. (extracted from [53])

1.2.3 Advantages of Femtosecond Laser Micromachining

Femtosecond laser micromachining is endowed with unique advantages due to the inherent properties and distinct laser-matter interaction mechanisms from those of longer pulsed lasers for the fs laser pulses. With the CPA technique, ultrashort laser pulses possess very high pulse peak intensity, while in the meanwhile have minimal heat-affected zone due to the ultrashort pulse duration. The cost of the fs laser sources is also declining thanks to the mass production and continuing reduced cost of essential components thereby making fs laser system a highly competitive alternative on the market.

Insusceptibility to Materials

Femtosecond laser pulses possess very high peak power and nonlinear photon energy absorption process can occur in the case that the energy of a single photon cannot excite the electrons to the conduction band, therefore the dielectric materials with high band gap and ultrahard materials with quite high melting point can easily be ablated by fs pulses. Femtosecond pulsed lasers have been demonstrated to ablate ultrahard and high bandgap materials such as diamond [54], metals with high melting point such as tungsten [55], semiconductors such as silicon [56], polymers such as poly(ε-caprolactone) (PCL) and poly (glycolic acid) (PGA) [57]. Theoretically, virtually any materials can be machined by the fs pulsed lasers.

Normal Ambient Condition

Since the fs laser micromachining is a maskless, contactless, direct-writing process to accomplish desired microstructures with no requirements of special ambient light, extra material such as photoresist and chemicals, the entire system can be placed in a normal lab and thus there is no need for stringent environment, clean room for example. This in turn greatly reduces the operating cost for the system and also manifests the fact that it is environmentally friendly as well.

Suppression of Heat-Affected Zone

Femtosecond laser micromachining can be considered non-thermal process, in sharp contrast to that with long pulses. The pulse width of a fs laser is much less than the minimum time it takes for the thermal wave to propagate into the lattice of the bulk materials. However, the electrons can be heated up relatively faster causing almost no HAZ surrounding the irradiated zone resulting in high-quality machined structures. This even applies in the case of materials with high thermal conductivity [33]. As can be evidenced from Figure 1.3, the crater created by fs laser ablation presents a smooth edge and steep wall whereas the one created by ns counterpart has apparent collateral damage at the edges.

Nanoscale Precision [33]

Since the propagation of thermal energy into the lattice is negligible, the spatial resolution achievable for fs laser micromachining theoretically better than longer pulses assuming they possess same wavelengths. Moreover, micromachining spatial resolution can be further improved if only the central part of a pulse is above ablation threshold in which case the machined laser spot size becomes smaller than the laser spot. With the unique nonlinear multiphoton energy absorption, the spatial resolution can be even improved further since the distribution of the absorbed energy becomes narrower as the order of the absorption increases due to the fact that the effective absorption cross section for n-photon absorption is proportional to the nth power of the original laser intensity. The effective beam size ω for n-photon absorption can be described as

$$\omega = \frac{\omega_0}{\sqrt{n}} \tag{1.18}$$

where ω_0 is the laser spot size determined by the diffraction limit. As can be seen, multiple factors collectively contribute to the capability of nanoscale precision for fs laser micromachining. In reality, however, unstable fs laser output makes fabrication with such high resolution difficult therefore diffraction limit still plays a role in achievable precision.

Energy-Efficient

Femtosecond laser micromachining is efficient in terms of energy consumption as almost no thermal energy transport to the lattice occurs. Quite recently researchers further increased the material removal efficiency by an order of magnitude over previously used laser parameters through ultrafast bursts of laser pulses making ablation cooling possible, that in turn lowers the pulse energy required to activate ablation [58].

1.2.4 Applications

The unique ablation mechanisms and the distinct advantages of fs laser micromachining

described in the preceding section paves the avenue for realizing a wide range of applications that have been demonstrated by numerous researchers and in countless commercial products. In addition, the development of more user-friendly fs laser machining tools facilitates the more acquisition of those instruments in research labs and fabrication facility in the manufacturing industry.

Photonics

Despite some other manufacturing techniques for photonic devices, fs laser micromachining has its own merits. The multiphoton absorption process yields precise and extremely small focal point resulting in smooth edges that is critical for photonic applications. Besides, ablation of dielectric transparent materials such as glass and crystals is extremely hard with long pulsed laser due to the high bandgap and lack of nonlinear absorption process. Furthermore, the capability of micromachining virtually any materials makes laser bonding or joining possible that opens up opportunity for more novel structures with versatile functionality that may not be readily accomplished by other techniques.

When intense and tightly focused ultrashort laser pulses are applied inside transparent materials, optical breakdown with the phenomenon of a microplasma within a tightly confined volume take place, therefore the permanent structural and refractive-index modifications are induced. With the programmable movement of the control stage, arbitrary position on the sample can be chosen as the target zone for irradiation, making complex 3D optics with great flexibility a reality. One of the first uses of fs laser micromachining technique is for making optical waveguide [59]. The photonic structures have been manufactured based on various glasses and other crystals, such as Er:Yb-doped glass [60], fused-silica glass [61], borosilicate glass [62] and strontium barium niobate (SBN) crystals [63]. Some conventional photonic devices or structures have also

been demonstrated by fs laser micromachining such as directional coupler [64], Mach-Zehnder interferometer [65], fiber gratings [66] and waveguide amplifier [67]. The 3D photonic crystal structures have been realized by two-photon-absorption photopolymerization of resin [68].

Microfluidics

The manipulation of fluids in microchannels, the so-called microfluidics, has emerged as an important field that has impact in diverse applications such as chemical analysis, particle sorting and separation, cell manipulation and drug screening. Conventional photolithography-based approach has the limitation to 2D channel fabrication, nevertheless, 3D microfluidic devices require time-consuming multilayer processing steps along with other procedures such as bonding, sealing etc [69].

Due to the reasons described above, the application of fs laser micromachining in biochip fabrication such as microfluidics and optofluidics has drawn much attention. There are two mainstream approaches exist for machining 3D microfluidics by fs pulsed lasers, namely, laser-assisted wet chemical etching and liquid-assisted laser drilling. The former method relies on the laser-induced material property change followed by applying chemical etching, typically acid solution [70] that usually achieves smooth inner walls while the latter one removes the debris by placing the sample in liquid environment during the micromachining process [71] that has the advantage of possibility of smaller dimension of the features. Numerous 3D microfluidic structures have been demonstrated such as micro-mixers [72], micro-valves [73] and micropumps [74].

Others

There is vast amount of other more specific and novel applications of fs laser micromachining. An interesting process called two-photon polymerization (TPP) has found widespread applications [33]. TPP transforms small unsaturated molecules in the liquid state to

macromolecules in the solid state because of polymerization reactions based on two-photon absorption. Only the irradiated regions are converted to solid state and the rest part can be washed away easily by specific solvent resulting in the inscribed 3D structure that has super high resolution since the diffraction limit can be exceeded.

Recently, fs laser-induced nanostructures are being extensively investigated due to the potential application in photonics, microfluidics, biomedical sector among others. It has been experimented on semiconductors [75], glasses [76], metals [77], among others. The fs laser-induced surface nanostructures have many applications, for example, color change of materials as evidenced in black silicon [78] and modification of target's wetting property as in metals [79].

In the past decade, another technique named Laser Ablation–Inductively Coupled Plasma–Mass Spectrometry (LA-ICP-MS) has been used extensively for quantitative chemical analysis that provides quantitative data for containing elements in the analyzed workpiece in which chemical element diagrams can be extracted. Femtosecond (fs) LA-ICP-MS offers more benefits for the chemical analysis: almost non-thermal with laser fluences not much higher than threshold; independence of material selections; modal distribution close to ~0.1-0.2 μm for generated particles with increased chance of decomposition [80]. Since R. E. Russo, X. Mao, J. Gonzalez and S. S. Mao demonstrated fs LA-ICP-MS analysis for the first time [81], it has been investigated for the mechanism and characteristics extensively. With minimal heat-affected zone, fs laser processing can extract chemical information with high spatial resolution and sensitivity [82].

1.3 Chapter Overview

In this body of research, three distinct microstructures fabricated by femtosecond laser micromachining technique in disparate applications are demonstrated, each of which exploits the unique advantages of the chosen machining approach and thus is not readily achievable with other

existing manufacturing methods. The presented novel devices, i.e. through-wafer 3D microchannels in silicon carbide (SiC), lateral dye-sensitized solar cells (DSSCs) and bioinspired photosensitivity enhancer (BPE), find their merits and great potential in the fields of microfluidics, photovoltaics and imaging science, respectively. Basic background, structural design, principle of operation, testing, and/or fabrication of the devices are described.

Chapter 1, the current chapter, states the broad background of the manufacturing technique, namely femtosecond (fs) laser micromachining, that is used to fabricate the microstructures listed in this dissertation. As the foundation of this micro-manufacturing approach, femtosecond laser ablation is explained in detail. Comparison of the aforementioned machining technology with the conventional competitors and its unique advantages are narrated as well. A brief literature review of the past work based on the approach of fs laser micromachining with the emphasis of the research and industrial applications is also conducted.

In Chapter 2, a through-wafer all-SiC fluidic microstructure fabricated by deionized (DI) water-assisted fs laser micromachining is demonstrated for the first time. Due to the unusual physical and chemical material properties of silicon carbide, the proposed prototype microfluidic structure is capable of operating in a harsh environment with elevated temperature, intense radiation and corrosive surroundings. Furthermore, through-wafer design opens the possibility of SiC wafer bonding that has a foreseeable potential for more novel microelectromechanical (MEMS) devices. The parameters of the fs laser pulses such as laser fluence and ablation speed are experimentally studied. Wettability modification with the water and mineral oil due to the laser-induced nanostructures is verified. With 3D machinability of the fs laser system, microchannels with different cross-sectional shapes are made in which the liquid flow characteristics are computationally simulated and compared. Visual liquid flow is presented in the surface

microchannels and through-wafer micro-via with the assistance of fluorescent dye.

Chapter 3 delves into the photovoltaic world and focuses on a dye-sensitized solar cells (DSSC's) with lateral structures based on nano-TiO_2/Fluorine-doped tin oxide (FTO) photoelectrode. The fill factor (FF) is more than double and the photon-to-electron conversion efficiency (η) is improved tremendously compared with the lateral solar cells previously reported. The fs pulsed laser is used to cut through TiO_2 film to create an interdigital pattern thereby forming two electrodes, one of which is deposited with platinum as the counter electrode (CE) while the other is covered by dye molecules as the photoelectrode (PE). The compact design of such lateral structure considerably simplifies the solar cell modules that enables hybrid solar energy harvesting/storage devices. The design, fabrication process, surface morphology and performance of the lateral DSSC's are presented and discussed.

Chapter 4 reports an artificial eye for scotopic vision consisting of an array of all-optical parabolic microstructures formed by fs laser micromachining inspired by the interesting features of superposition compound eyes and retinal structure of elephantnose fish. The artificial eye is realized through a passive optical device, i.e. biologically inspired photosensitivity enhancer (BPE) made of thousands of so-called microphotocollectors (μ-PCs) that can significantly increase the photosensitivity and hence it is particularly useful for image capturing in dim environment. Work principle along with structural design of the BPE is explained briefly followed by the introduction of a software-based image restoration strategy called super-resolution image reconstruction algorithm adopted to greatly increase resolution of the obtained images since the spatial resolution of the BPE is reduced inherently by the unique μ-PC structure. The high-resolution image is evaluated quantitatively by the image assessment method of structural similarity (SSIM) index indicating that the reconstructed high-resolution (HR) image with the initial guess of average of

expanded low-resolution (LR) images presents the closest approximation to the original distortion-free HR image.

Chapter 5 summarizes the generic conclusions drawn from research work described in this dissertation and suggests possible future work.

Appendix A lists the Matlab code for the main program that reconstructs the high-resolution images shown in figure 4.13 while Appendix B includes the Matlab code for a function implementing the iterative-back-projection super-resolution algorithm and returning a reconstructed high-resolution image and it is called by the main program in Appendix A.

1.4 References

[1] G. L. LeCarpentier, M. Motamedi, L. P. McMath, S. Rastegar and A. J. Welch, "Continuous wave laser ablation of tissue: analysis of thermal and mechanical events," IEEE Transactions on Biomedical Engineering, Volume 40, Number 2, pp. 188-200, (1993).

[2] Y. M. Tsipenyuk, “Physical methods, Instruments and Measurements”, Volume 4, ISBN 978-1-905839-57-5, EOLSS Publishers (2009).

[3] N. M. Bulgakova, and A. V. Bulgakov, “Pulsed laser ablation of solids: transition from normal vaporization to phase explosion”, Applied Physics A: Materials Science & Processing, Volume 73, Issue 2, pp. 199-208 (2001).

[4] R. Stoian, D. Ashkenasi, A. Rosenfeld, and E. E. B. Campbell, “Coulomb explosion in ultrashort pulsed laser ablation of Al_2O_3”, Physical Review B, Volume 62, Number 19, pp. 13167-13173 (2000).

[5] R. Le Harzic, N. Huot, E. Audouard, C. Jonin, and P. Laporte, “Comparison of heat-affected zones due to nanosecond and femtosecond laser pulses using transmission electronic

microscopy", Applied Physics Letters, Volume 80, Number 21, pp. 3886-3888 (2002).

[6] http://www.calctool.org/CALC/phys/optics/pulsed_source.

[7] R. E. Russo, "Laser Ablation", Applied Spectroscopy, Volume 49, Number 9, pp. 14-28 (2009).

[8] B. N. Chichkov, C. Momma, S. Nolte, F. von Alvensleben, A. Tünnermann, "Femtosecond, picosecond and nanosecond laser ablation of solids", Applied Physics A: Materials Science & Processing, Volume 63, Issue 2, pp. 109-115 (1996).

[9] X. Y. Wang, D. M. Riffe, Y. S. Lee, M. C. Downer, "Time-resolved electron-temperature measurement in a highly excited gold target using femtosecond thermionic emission", Physical Review B, Volume 50, Issue 11, pp. 8016-8019 (1994).

[10] T. Sasaki, Y. Shimizu, N. Koshizaki, "Preparation of metal oxide-based nanomaterials using nanosecond pulsed laser ablation in liquids", Journal of Photochemistry and Photobiology A: Chemistry, Volume 182, Issue 3, pp. 335–341 (2006).

[11] M. Barry, B. Ding, Y. Jung, B.V.K. Reddy, T. X. Phuoc, M. K. Chyu, "Pulsed nanosecond laser ablation of gold in deionized water and aqueous chitosan solution", Optics and Lasers in Engineering, Volume 55, pp. 59–68 (2014).

[12] R. Karimzadeh, J. Zamir Anvari, N. Mansour, "Nanosecond pulsed laser ablation of silicon in liquids", Applied Physics A: Materials Science & Processing, Volume 94, Issue 4, pp. 949-955 (2009).

[13] B. J. Garrison, R. Srinivasan, "Laser ablation of organic polymers: microscopic models for photochemical and thermal processes", Journal of Applied Physics, 57(8), pp. 2909-2914 (1985).

[14] J. G. Fujimoto, J. M. Liu, and E. P. Ippen, "Femtosecond Laser Interaction with Metallic Tungsten and Nonequilibrium Electron and Lattice Temperatures", Physical Review Letters,

Volume 53, Number 19, pp. 1837-1840 (1984).

[15] M. Stafe, A. Marcu, N. N. Puscas, “Pulsed Laser Ablation of Solids: Basics, Theory and Applications”, ISBN: 978-3-642-40977-6 (2014).

[16] S. Amoruso, R. Bruzzese, N. Spinelli, and R. Velotta, “Characterization of laser-ablation plasmas”, Journal of Physics B: Atomic, Molecular and Optical Physics, Volume 32, Number 14, pp. 131-172 (1999).

[17] Y. Izawa, Y. Setuhara, M. Hashida, M. Fujita and Y. Izawa, “Ablation and amorphization of crystalline Si by femtosecond and picosecond laser irradiation”, Japanese Journal of Applied Physics, Volume 45, Number 7, pp. 5791–5794 (2006).

[18] M. D. Perry, B. C. Stuart, P. S. Banks, M. D. Feit, V. Yanovsky, and A. M. Rubenchik, “Ultrashort-pulse laser machining of dielectric materials”, Journal of Applied Physics, Volume 85, Issue 9, pp. 6803-6810 (1999).

[19] J. Ihlemann, “Excimer laser ablation of fused silica”, Applied Surface Science, Volume 54, pp. 193-200 (1992).

[20] D. Strickland, G. Mourou, “Compression of amplified chirped optical pulses”, Optics Communications, Volume 56, Issue 3, pp. 219–221 (1985).

[21] P. Maine, D. Strickland, P. Bado, M. Pessot, and G. Mourou, “Generation of ultrahigh peak power pulses by chirped pulse amplification”, IEEE Journal of Quantum Electronics, Volume 24, Issue 2, pp. 398-403 (1988).

[22] K. Nakajima, J. Yuan, L. Chen, and Z. Sheng, “Laser-Driven Very High Energy Electron/Photon Beam Radiation Therapy in Conjunction with a Robotic System”, Applied Sciences, Volume 5, Issue 1, pp. 1-20 (2015).

[23] N. Marquestaut, Y. Petit, A. Royon, P. Mounaix, T. Cardinal, L. Canioni, “Three-

Dimensional Silver Nanoparticle Formation Using Femtosecond Laser Irradiation in Phosphate Glasses: Analogy with Photography", Advanced Functional Materials, Volume 24, Issue 37, pp. 5824–5832 (2014).

[24] X. L. Tong, D. S. Jiang, Z. M. Liu, M. Z. Luo, Y. Li, P. X. Lu, G. Yang, and H. Long, "Structural characterization of CdS thin film on quartz formed by femtosecond pulsed laser deposition at high temperature", Thin Solid Films, Volume 516, Issue 8, pp. 2003–2008 (2008).

[25] M. Womack, M. Vendan, P. Molian, "Femtosecond pulsed laser ablation and deposition of thin films of polytetrafluoroethylene", Applied Surface Science, Volume 221, pp. 99–109 (2004).

[26] Y. Jia, F. Chen, J. R. Vázquez de Aldana, Sh. Akhmadaliev, S. Zhou, "Femtosecond laser micromachining of Nd:GdCOB ridge waveguides for second harmonic generation", Optical Materials, Volume 34, Issue 11, pp. 1913–1916 (2012).

[27] K. Tada, G. A. Cohoon, K. Kieu, M. Mansuripur, and R. A. Norwood, "Fabrication of High-Q Microresonators Using Femtosecond Laser Micromachining", IEEE Photonics Technology Letters, Volume 25, Number 5, pp. 430-433 (2013).

[28] Z. Deng, Q. Yang, F. Chen, X. Meng, H. Bian, J. Yong, C. Shan, and X. Hou, "Fabrication of large-area concave microlens array on silicon by femtosecond laser micromachining", Optics Letters, Volume 40, Issue 9, pp. 1928-1931 (2015).

[29] R. E. Russo, X. Mao, H. Liu, J. Gonzalez, S. S. Mao, "Laser ablation in analytical chemistry—a review", Talanta, Volume 57, Issue 3, pp. 425–451 (2002).

[30] S. S. Harilal, J. R. Freeman, P. K. Diwakar, and A. Hassanein, "Femtosecond Laser Ablation: Fundamentals and Applications", book chapter 6, Publisher: Springer, Editor: Musazzi S. and Perini U., ISBN: 978-3-642-45084-6 (2014).

[31] P. Gonzales, R. Bernath, J. Duncan, T. Olmstead and M. Richardson, "Femtosecond

ablation scaling for different materials", Proc. SPIE 5458, Optical Micro- and Nanometrology in Manufacturing Technology, 265 (August 17, 2004), doi:10.1117/12.545927.

[32] B. Rethfeld, D. S. Ivanov, M. E. Garcia, and S. I. Anisimov, "Modelling ultrafast laser ablation", Journal of Physics D: Applied Physics, Volume 50, Number 19, pp. 193001-193039 (2017).

[33] K. Sugioka, and Y. Cheng, "Femtosecond laser three-dimensional micro- and nanofabrication", Applied Physics Reviews, Volume 1, Issue 4, p. 041303 (2014).

[34] P. F. Moulton, "Spectroscopic and laser characteristics of Ti:Al2O3", Journal of the Optical Society of America B, Volume 3, Issue 1, pp. 125-133 (1986).

[35] K. F. Wall, and A. Sanchez, "Titanium Sapphire Lasers", The Lincoln Laboratory Journal, Volume 3, Number 3, pp. 447-462 (1990).

[36] http://www.cmxr.com/Products/LaserProducts/CPA-Series.html

[37] A. A. Lagatsky, C. G. Leburn, C. T. A. Brown, W. Sibbett, S. A. Zolotovskaya, and E. U. Rafailov, "Ultrashort-pulse lasers passively mode locked by quantum-dot-based saturable absorbers", Progress in Quantum Electronics, Volume 34, Issue 1, pp. 1–45 (2010).

[38] T. R. Schibli, K. Minoshima, H. Kataura, E. Itoga, N. Minami, S. Kazaoui, K. Miyashita, M. Tokumoto, and Y. Sakakibara, "Ultrashort pulse-generation by saturable absorber mirrors based on polymer-embedded carbon nanotubes", Optics Express, Volume 13, Issue 20, pp. 8025-8031 (2005).

[39] Z. P. Sun, T. Hasan, F. Torrisi, D. Popa, G. Privitera, F. Q. Wang, F. Bonaccorso, D. M. Basko, and A. C. Ferrari, "Graphene mode-locked ultrafast laser", ACS Nano, Volume 4, Number 2, pp. 803–810 (2010).

[40] H. M. Pask, R. J. Carman, D. C. Hanna, A. C. Tropper, C. J. Mackechnie, P. R. Barber,

and J. M. Dawes, “Ytterbium-Doped Silica Fiber Lasers: Versatile Sources for the 1-1.2 μm Region”, IEEE Journal of Selected Topic in Quantum Electronics, Volume 1, Issue 1, pp. 2–13 (1995).

[41] R. M. Percival, D. Szebesta, S. T. Davey, N. A. Swain, and T. A. King, “High-efficiency CW operation of 890 nm pumped holmium fluoride fibre laser”, Electronics Letters, Volume 28, Issue 22, pp. 2064 - 2066 (1992).

[42] https://www.rp-photonics.com/mode_locked_fiber_lasers.html

[43] P. Cardoso and J. P. Davim, “A brief review on micromachining of materials”, Reviews on Advanced Materials Science, Volume 30, Number 1, pp. 98-102 (2012).

[44] T. Moriwaki, and K. Okuda, “Machinability of Copper in Ultra-Precision Micro Diamond Cutting”, CIRP Annals - Manufacturing Technology, Volume 38, Issue 1, pp. 115-118 (1989).

[45] S. Thamizhmanii and H. Sulaiman, “Machinability of hard stainless steel and alloy steel using PCBN tools”, Journal of Achievements in Materials and Manufacturing Engineering, Volume 46, Issue 2, pp. 169-174 (2011).

[46] X. P. Li, T. He, and M. Rahman, “Tool wear characteristics and their effects on nanoscale ductile mode cutting of silicon wafer”, Wear, Volume 259, Issues 7-12, pp. 1207–1214 (2005).

[47] P. S. Spinney, D. G. Howitt, R. L. Smith and S. D. Collins, “Nanopore formation by low-energy focused electron beam machining”, Nanotechnology, Volume 21, Number 37, p. 375301 (2010).

[48] R. Roy, D. Allen, and O. Zamora, “Cost of photochemical machining”, Journal of Materials Processing Technology, Volume 149, Issues 1-3, pp. 460–465 (2004).

[49] R. Kovacevic, M. Hashish, R. Mohan, M. Ramulu, T. J. Kim and E. S. Geskin, “State of the Art of Research and Development in Abrasive Waterjet Machining”, Journal of Manufacturing

Science and Engineering, Volume 119, Issue 4B, pp. 776-785 (1997).

[50] D. N. Mishra, A. Bhatia, and V. Rana, “Study on Electro Discharge Machining (Edm)”, International Journal of Engineering and Science, Volume 3, Issue 2, pp. 24-35 (2014).

[51] B. Bhattacharyya, J. Munda, and M. Malapati, “Advancement in electrochemical micro-machining”, International Journal of Machine Tools & Manufacture, Volume 44, Issue 15, pp. 1577–1589 (2004).

[52] D. Du, X. Liu, G. Korn, J. Squier, and G. Mourou, “Laser-induced breakdown by impact ionization in SiO_2 with pulse widths from 7 ns to 150 fs”, Applied Physics Letters, Volume 64, Issue 23, pp. 3071-3073 (1994).

[53] X. Li, G. Zhang, L. Jiang, X. Shi, K. Zhang, W. Rong, Ji’an Duan, and Y. Lu, “Production rate enhancement of size-tunable silicon nanoparticles by temporally shaping femtosecond laser pulses in ethanol”, Optics Express, Volume 23, Issue 4, pp. 4226-4232 (2015).

[54] M. D. Shirk and P. A. Molian, “Ultrashort pulsed laser ablation of diamond”, Journal of Laser Applications, Volume 10, Issue 2, pp. 64-70 (1998).

[55] J. Byskov-Nielsen, J. M. Savolainen, M. S. Christensen, and P. Balling, “Ultra-short pulse laser ablation of copper, silver and tungsten: experimental data and two-temperature model simulations”, Applied Physics A, Volume 103, Issue 2, pp. 447–453 (2011).

[56] X. Zeng, X. L. Mao, R. Greif, and R. E. Russo, “Experimental investigation of ablation efficiency and plasma expansion during femtosecond and nanosecond laser ablation of silicon”, Applied Physics A, Volume 80, Issue 2, pp. 237–241 (2005).

[57] C. A. Aguilar, Y. Lu, S. Mao, and S. Chen, “Direct micro-patterning of biodegradable polymers using ultraviolet and femtosecond lasers”, Biomaterials, Volume 26, Issue 36, pp. 7642–7649 (2005).

[58] C. Kerse, H. Kalaycıoğlu, P. Elahi, B. Çetin, D. K. Kesim, Ö. Akçaalan, S. Yavaş, M. D. Aşık, B. Öktem, H. Hoogland, R. Holzwarth, and F. Ö. Ilday, "Ablation-cooled material removal with ultrafast bursts of pulses", Nature, Volume 537, Issue 7618, pp. 84–88 (2016).

[59] K. M. Davis, K. Miura, N. Sugimoto, and K. Hirao, "Writing waveguides in glass with a femtosecond laser", Optics Letters, Volume 21, Issue 21, pp. 1729–1731 (1996).

[60] G. Cerullo, R. Osellame, S. Taccheo, M. Marangoni, D. Polli, R. Ramponi, P. Laporta, and S. De Silvestri, "Femtosecond micromachining of symmetric waveguides at 1.5 µm by astigmatic beam focusing", Optics Letters, Volume 27, Issue 21, pp. 1938–1940 (2002).

[61] D. Homoelle, S. Wielandy, A. L. Gaeta, N. F. Borrelli, and C. Smith, "Infrared photosensitivity in silica glasses exposed to femtosecond laser pulses", Optics Letters, Volume 24, Issue 18, pp. 1311-1313 (1999).

[62] C. B. Schaffer, A. Brodeur, J. F. García, and E. Mazur, "Micromachining bulk glass by use of femtosecond laser pulses with nanojoule energy", Optics Letters, Volume 26, Issue 2, pp. 93-95 (2001).

[63] D. Jaque, N. D. Psaila, R. R. Thomson, F. Chen, L. M. Maestro, A. Ródenas, D. T. Reid, and A. K. Kar, "Ultrafast laser inscription of bistable and reversible waveguides in strontium barium niobate crystals", Applied Physics Letters, Volume 96, Issue 19, p. 191104 (2010).

[64] A. M. Streltsov and N. F. Borrelli, "Fabrication and analysis of a directional coupler written in glass by nanojoule femtosecond laser pulses", Optics Letters, Volume 26, Issue 1, pp. 42-43 (2001).

[65] Y. Wang, M. Yang, D. N. Wang, S. Liu, and P. Lu, "Fiber in-line Mach–Zehnder interferometer fabricated by femtosecond laser micromachining for refractive index measurement with high sensitivity", Journal of the Optical Society of America B, Volume 27, Issue 3, pp. 370-

374 (2010).

[66] Q. Huang, Y. Yu, S. Ruan, X. Li, X. Chen, Y. Zhang, W. Zhou, and C. Du, "In-Fiber Grating Fabricated by Femtosecond Laser Direct Writing for Strain Sensing", IEEE Photonics Technology Letters, Volume 27, Issue 11, pp. 1216-1219 (2015).

[67] G. Della Valle, R. Osellame, N. Chiodo, S. Taccheo, G. Cerullo, P. Laporta, A. Killi, U. Morgner, M. Lederer, and D. Kopf, "C-band waveguide amplifier produced by femtosecond laser writing", Optics Express, Volume 13, Issue 16, pp. 5976-5982 (2005).

[68] H. Sun, S. Matsuo, H. Misawa, "Three-dimensional photonic crystal structures achieved with two-photon-absorption photopolymerization of resin", Applied Physics Letters, Volume 74, Issue 6, pp. 786-788 (1999).

[69] C.-W. Tsao, and D. L. DeVoe, "Bonding of thermoplastic polymer microfluidics", Microfluidics and Nanofluidics, Volume 6, Issue 1, pp. 1–16 (2009).

[70] A. Marcinkevičius, S. Juodkazis, M. Watanabe, M. Miwa, S. Matsuo, H. Misawa, and J. Nishii, "Femtosecond laser-assisted three-dimensional microfabrication in silica", Optics Letters, Volume 26, Issue 5, pp. 277-279 (2001).

[71] K. Ke, E. F. Hasselbrink, and A. J. Hunt, "Rapidly Prototyped Three-Dimensional Nanofluidic Channel Networks in Glass Substrates", Analytical Chemistry, Volume 77, Issue 16, pp. 5083-5088 (2005).

[72] Y. Liao, J. Song, E. Li, Y. Luo, Y. Shen, D. Chen, Y. Cheng, Z. Xu, K. Sugioka and K. Midorikawa, "Rapid prototyping of three-dimensional microfluidic mixers in glass by femtosecond laser direct writing", Lab on a Chip, Volume 12, Issue 4, pp. 746-749 (2012).

[73] M. Masuda, K. Sugioka, Y. Cheng, T. Hongo, K. Shihoyama, H. Takai, I. Miyamoto, and K. Midorikawa, "Direct fabrication of freely movable microplate inside photosensitive glass by

femtosecond laser for lab-on-chip application”, Applied Physics A, Volume 78, Issue 7, pp. 1029–1032 (2004).

[74] S. Maruo, and H. Inoue, “Optically driven micropump produced by three-dimensional two-photon microfabrication”, Applied Physics Letters, Volume 89, Issue 14, p. 144101 (2006).

[75] G. Miyaji, K. Miyazaki, K. Zhang, T. Yoshifuji, and J. Fujita, “Mechanism of femtosecond-laser-induced periodic nanostructure formation on crystalline silicon surface immersed in water”, Optics Express, Volume 20, Issue 14, pp. 14848-14856 (2012).

[76] S. Höhm, A. Rosenfeld, J. Krüger, and J. Bonse, “Femtosecond laser-induced periodic surface structures on silica”, Journal of Applied Physics, Volume 112, Issue 1, p. 014901 (2012).

[77] Y. Huang, S. Liu, W. Li, Y. Liu, and W. Yang, “Two-dimensional periodic structure induced by single-beam femtosecond laser pulses irradiating titanium”, Optics Express, Volume 17, Issue 23, pp. 20756-20761 (2009).

[78] C. Wu, C. H. Crouch, L. Zhao, J. E. Carey, R. Younkin, J. A. Levinson, E. Mazur, R. M. Farrell, P. Gothoskar, and A. Karger, “Near-unity below-band-gap absorption by microstructured silicon”, Applied Physics Letters, Volume 78, Issue 13, pp. 1850-1852 (2001).

[79] P. Bizi-Bandoki, S. Benayoun, S. Valette, B. Beaugiraud, and E. Audouard, “Modifications of roughness and wettability properties of metals induced by femtosecond laser treatment”, Applied Surface Science, Volume 257, Issue 12, pp. 5213–5218 (2011).

[80] F. Poitrasson, and F.-X. d'Abzac, “Femtosecond laser ablation inductively coupled plasma source mass spectrometry for elemental and isotopic analysis: are ultrafast lasers worthwhile?”, Journal of Analytical Atomic Spectrometry, Advance Article (2017).

[81] R. E. Russo, X. Mao, J. J. Gonzalez, and S. S. Mao, “Femtosecond laser ablation ICP-MS”, Journal of Analytical Atomic Spectrometry, Volume 17, Issue 9, pp. 1072-1075 (2002).

[82] B. Fernández, F. Claverie, C. Pécheyran, O. F.X. Donard, “Direct analysis of solid samples by fs-LA-ICP-MS”, Trends in Analytical Chemistry, Volume 26, Issue 10, pp. 951-966 (2007).

CHAPTER 2

Fabrication of Through-Wafer 3D Microfluidics in Silicon Carbide Using Femtosecond Laser

Part of the contents in this chapter has been published as:

Y. Huang, X. Wu, H. Liu, and H. Jiang, "Fabrication of through-wafer 3D microfluidics in silicon carbide using femtosecond laser," ***Journal of Micromechanics and Microengineering*****, Vol. 27, No. 6, Article No. 065005, 2017.**

In this chapter, a prototype through-wafer microfluidic structure in bulk silicon carbide (SiC) fabricated by femtosecond laser micromachining is demonstrated. The comparison of micromachining quality in the environment of air and deionized (DI) water is presented. The effects of laser fluence, scanning speed and different objective lenses on the laser-affected zone (LAZ) are also investigated. Furthermore, the wettability of the laser-affected surface for the target liquid, mineral oil, is examined. Microchannels of various cross-sectional shapes are fabricated by the femtosecond laser and their effects on the liquid flow are simulated and compared. This fabrication approach offers a fast and efficient route to implement SiC-based through-wafer micro-structures, which are not able to be realized using other methods such as chemical etching. The flexibility of manufacturing 3D structures based on this fabrication method enables more complex structures as well. Smooth liquid flow in the microchannels of the bulk SiC substrate is presented. The work shown here paves a new avenue for various applications such as reliable microfluidic systems in a high-temperature, high-radioactivity, and corrosive environment, and could be

combined with SiC wafer-to-wafer bonding to realize a plethora of novel microelectromechanical (MEMS) structures.

2.1 Introduction

Microfluidics has witnessed tremendous growth over the last two decades in applications ranging from biochemical analysis and medical research to microelectronics and optics. It has realized numerous devices such as gas chromatography [1], micro-mixers [2–4], micro-valves [5], micropumps [6], etc. Widely used fabrication techniques for 3D microfluidic devices include soft photolithography [7], thermo-forming such as injection molding [8], and etching, i.e. dry etching with plasma [9] and wet etching with chemical solutions [10]. At present, silicon [11], glass [12], and polymers such as polydimethylsiloxane (PDMS) [13] are the most common materials used in microfluidic systems. They are, however, unable to survive or function satisfactorily in a harsh environment with high temperature [14], and intense radiation [15], and/or corrosive substance [16].

Currently, silicon carbide (SiC) is the most established material for device applications in harsh environments as it is hard, temperature tolerant, chemically inert, resistant to high electric field, and biocompatible [17, 18] due to its wide band gap [17]. SiC has been extensively investigated and used in various applications such as MEMS resonators capable of wider operating frequencies than the polysilicon-based ones [19] and pressure sensors [20]. Most of the SiC-based MEMS devices developed are realized by crystalline SiC thin film deposited on other easy-to-etch bulk substrates, particularly silicon substrate [21]. However, it is still immature to fabricate directly on the bulk SiC substrates that are required for various applications such as all-SiC microsystem devices and through-wafer bonding tailored for a harsh environment. The high thermal stability

and chemical inertness make SiC extremely difficult to be etched compared with silicon: for example, potassium hydroxide slightly below 100 °C is widely used to fabricate Si-based devices, whereas the process is not suitable for SiC [22]. Furthermore, both wet- and dryetching techniques require hard masks such as metal that has high selectivity. However, such masks may contaminate the chambers of plasma etch systems and roughen the surface of a SiC substrate [23], as metal masks, despite being chemically inert, are still etched by the flux of ions in a plasma etching chamber over the long term. Then, micromasking occurs in which the non-volatile by-products generated are redeposited on the sample or in the chamber, thereby reducing the quality of the transferred patterns and gradually degrading the quality of the etch tools. In addition, the etching technique is not applicable for complex 3D device fabrication. The laser direct writing technique has been proposed as an alternative to reactive-ion dry etching due to its simplicity, low-cost, capability of fabricating complex 3D structures, and fast ablation rate for hard materials [24, 25]. Recently, femtosecond laser micromachining has drawn more attention than its longer-pulsed counterparts owing to the advantages of precision micromachining capability, lower thermal and material damage, less sensitivity to target materials, and high repeatability with accurate ablation threshold [26]. Therefore, femtosecond pulsed laser ablation is superior when ablating ultrahard and hard-to-etch materials such as SiC. So far, the femtosecond laser micromachining technique has shown success in ablating SiC films on Si substrates for MEMS devices [27], optical ridge waveguide formation [28], in-air through-hole fabrication in SiC substrates [29], and alcohol-assisted through-hole drilling in SiC [30]. However, the SiC MEMS devices fabricated by femtosecond laser micromachining were restricted to the surface thin film and the SiC through-wafer studies were focused merely on the characterization of the via holes by single shot ablation.

Here, we present a through-wafer fluidic structure consisting of microchannels in bulk 4H–

SiC wafer fabricated by deionized water-assisted femtosecond laser micromachining for the first time. It has been reported that the water-assisted near-infrared laser drilling of SiC generates better quality and much less debris than ablating the material in air [31]. High-quality microchannels were achieved with minimal thermal effect around the laser affected zones (LAZs) in which the liquid could flow smoothly. Morphological qualities of microchannels machined by the fs pulsed laser in air and DI water are compared. The effects of laser fluence, ablation speed and different objective lenses on the dimensions of the trenches that resulted from a single ablation were characterized. In addition, it was found that the surface of the LAZ of SiC is highly attractive to mineral oil with a contact angle of less than 5°. Moreover, the surface morphology of the microchannels comprising the microfluidic structure was characterized by a scanning electron microscope (SEM), while the depth and width of the grooves generated by single ablation were measured by a high-resolution surface profilometer.

2.2 Experimental Details

2.2.1 Fabrication of Microchannels and Vias on Bulk SiC Substrates

The fabrication of microchannels and via holes on the SiC substrates was achieved by a femtosecond laser micromachining system, which is illustrated in figure 2.1(A). A high-energy fiber femtosecond laser (Uranus2000-1030-1000, Laser-Femto, Inc., USA) with a wavelength of 1030 nm, pulse width of 700 fs, and repetition rate of 121 kHz was transmitted into an objective lens (Mitutoyo, Japan) with a numerical aperture of 0.42 and focused onto the SiC target. The diameter of the focal spot was about 1.5 µm. A mechanical shutter was applied to switch the laser on or off. The power of the laser was adjusted by a polarizer. To achieve a clean surface after the laser ablation, the SiC sample was immersed in a deionized water (DI water) chamber that was

mounted on a computer-controlled translation stage (Newport XMS-160, XMS-100, and GTS-30 V for x-, y-, and z-axis, respectively) with the precision of 0.1 μm. The flow rate of the water was about 1 mm s−1. A CCD camera (Thorlabs Inc., USA) was employed for the real-time monitoring of the laser processing. The microchannels and via holes were fabricated by a layer-by-layer ablation process with the laser scanning strategy shown in figures 2.1(B) and (C), respectively. For the specific structures mentioned in this work, it took approximately 45 min to produce the via hole and 20–40 min to fabricate the microchannels depending on the various cross-sectional shapes.

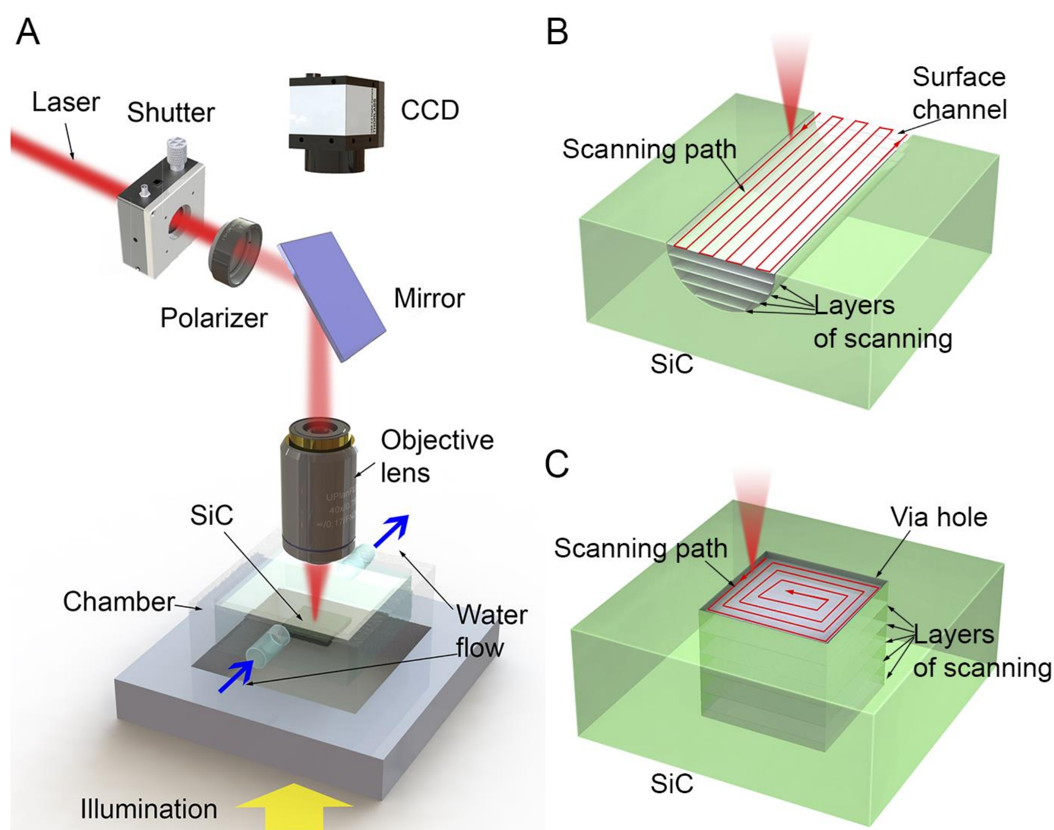

Figure 2.1. Schematic diagrams of the femtosecond laser micromachining. (A) Optical setup of the laser micromachining system. (B) Laser scanning strategy for the surface channel. (C) Laser scanning strategy for the via hole.

2.2.2 Preparation and Characterization of the SiC Samples

In our experiments, double polished 4H–SiC substrates (N-type doped, CREE, USA) with a thickness of ~350 micrometers were utilized. The wafer was cleaved into 1 × 1 cm2 square pieces and pre-washed with DI water before the laser ablation. The laser power was measured right before the laser beams hit the DI water surface. After the laser treatment, the samples were cleaned with acetone, methanol, and DI water in an ultrasonic bath for 15 min, respectively. The morphology of the ablated microchannels was characterized by an SEM (Zeiss LEO 1530, Germany) and a high-resolution optical microscope (Nikon Eclipse LV100ND, Japan), while the width and depth of the ablated grooves were measured by a high-resolution surface profilometer (Tencor AlphaStep 200).

2.2.3 Measurement of Contact Angle on the SiC Surfaces

A goniometer (OCA series, Future Digital Scientific Corp, USA) was used to measure the contact angles of the mineral oil and DI water on the SiC sample surface with and without the laser ablation. The sample was placed on a manually controlled 3-axis stage. The liquid droplet (1.5 μl) was dispensed from a volume controlled pipette onto the sample surface.

To test the wettability of the laser ablated SiC surface, an area of 5 x 5 mm^2 on the SiC was ablated by a line-scanning path with a pulse energy of 1.40 μJ and a scanning speed of 1 mm/s. The laser ablation area was much larger than the dimension of the droplet, so that the contact boundary of the droplet would not touch the edge of the laser-ablated area to ensure the accuracy of the measured contact angle.

2.2.4 Assembly and Characterization of the SiC Microfluidic Device

To demonstrate the laser micromachining of microfluidics on SiC substrates, a microfluidic device shown in figure 2.2(A) was fabricated and tested. Two straight microchannels with a

diameter of 100 μm and cross-section of a semicircle on both sides of a 1.6×1 cm^2 SiC substrate were connected by a via hole, forming a Z-shaped microfluidic channel, as illustrated in figure 2.2(B). The SiC substrate was flipped to machine the second microchannel, since the laser power was attenuated greatly after traveling through the wafer and thus no ablation could occur. In order to test the flow in the microfluidic system, two pieces of polydimethylsiloxane (PDMS) were pre-treated with oxygen plasma and then bonded on the top and bottom surfaces of the SiC sample, respectively, on a hotplate at 60° for 12 h to facilitate the bonding. The plasma treatment was used to bond the oxidized PDMS surfaces and then seal permanently to create leak-tight microchannels in our microfluidic microchannels. A syringe was used to inject the liquid into the microchannel via a drilled hole in the top PDMS layer. Since the pure fluid could not be observed under the optical microscope, a red solvent-based fluorescent dye (Solvent 250 Red Fluorescent Color Coding Dye, Kingscote Chemicals, USA) was mixed with the liquid to generate a vivid red color to denote the microfluidic path under the optical microscope.

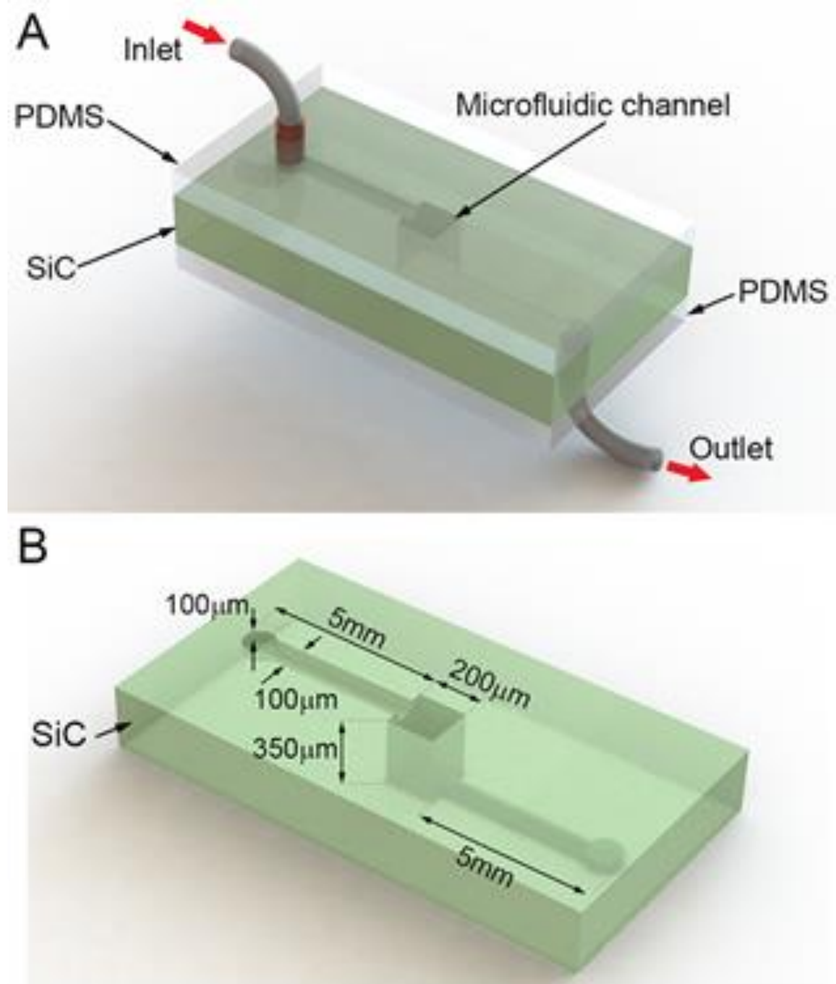

Figure 2.2. Structural design of the Z-shaped microfluidics on SiC. (A) Schematic diagram of the microfluidic device. (B) Dimensions of the microchannels and via hole on the SiC substrate.

2.3 Results and Discussion

2.3.1 Comparison of Machining Microstructures in Air and DI Water

Before tuning the laser parameters to achieve optical micromachining quality, another crucial factor that may affect the results, the ablation environment, should be evaluated especially for bulk micromachining process. One of the tests conducted was to make microchannels with the diameter of 100 μm with semicircular cross-sectional shape on the sample surface in the air and DI water, respectively. The laser parameters were chosen so as the ablation threshold was reached but the power was not too high to cause apparent collateral damage. The laser scanning speed was

set at 2 mm/s while the pulse energy was ~2.23 μJ. Figure 2.3(A) and figure 2.3(B) show the SEM images of the microchannels ablated in the air and DI water, respectively. As can be seen from figure 2.3, the microchannel processed in the DI water is much better in terms of uniformity and overall quality than that produced in the air. In fact, at some point during the micromachining process in the air, the laser-induced plume was not observed anymore and the laser beam became out of focus as seen via the CCD indicating no more ablation took place. This phenomenon combined with the high roughness of the microchannel wall in figure 2.3(A) suggests that large amount of debris due to the laser-SiC interaction was produced and finally deposited in the microchannel when processed in the air. In addition, it can be inferred that the re-solidification of the ablated material was so fast that it could not travel outside the microchannel before it cooled down, partly because of the ultrahigh melting point of silicon carbide (~2800°C). On the other hand, the ablated material was mostly carried away by the flowing DI water resulting in a much cleaner wall.

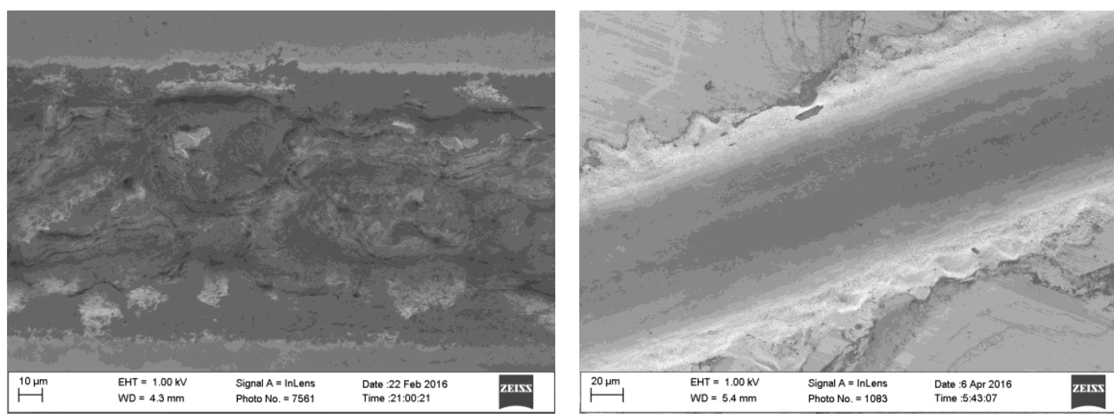

(A) (B)

Figure 2.3. Surface SEM images of microchannels with cross-sectional shape of semicircle and diameter of 100 μm with the parameters of scanning speed of 2 mm/s and pulse energy of ~2.23

μJ in (A) Air. (B) Deionized water.

This disparate performance in the two media can be further demonstrated when ablating small features. Figures 2.4(A) and 4(B) present intended through-wafer via structures processed at the same laser parameters listed for ablating the aforementioned microchannels in the air and DI water, respectively. As clearly shown in the figures, only first few layers of SiC were affected by the fs laser with no discernible depth of ablation while the water-assisted process created the micro-via stretching through the SiC substrate, which is due to the re-solidified substance accumulated around the small LAZs when lack of ambient liquid. When machining SiC using the similar laser parameters, the smaller features it requires, the more difficult it becomes to ablate the SiC in the air.

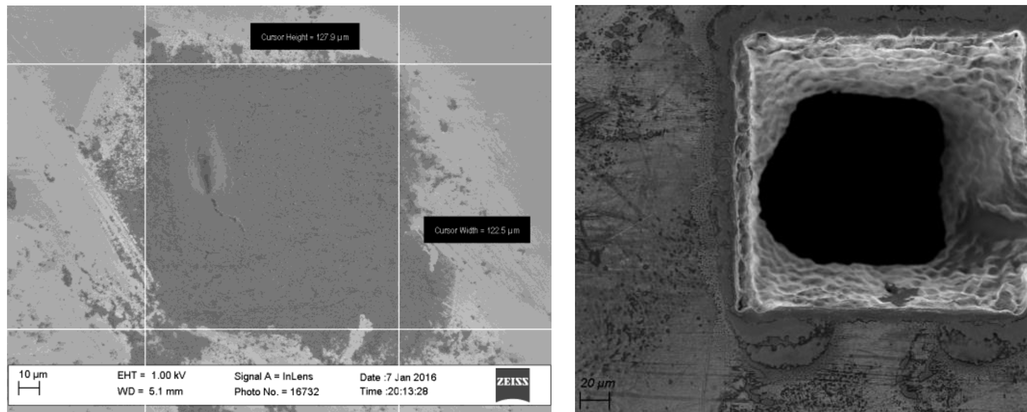

Figure 2.4. Surface SEM images of through-wafer via microstructures with diameter of 125 μm and parameters of scanning speed of 2 mm/s and pulse energy of ~2.23 μJ in (A) Air. (B) Deionized water.

2.3.2 Influence of Laser Parameters on Ablation Rate

Laser parameters play the crucial role in determining the micromachining quality in laser

micromachining process, therefore it is needed to pay meticulous attention to their calibration and testing. Despite not being as sensitive as some other laser parameters, the selection of objective lenses has impact on the machining process and quality in terms of processing time and focal spot size.

To investigate the effect of objective lenses of different magnifications quantitatively, a test of single-line one-time ablation on the SiC was performed. Figure 2.5(A) and 5(B) show the cross-sectional SEM images for trenches formed by fs laser in the environment of DI water with scanning speed of 1 mm/s and pulse energy 4.32 μJ using a 20X and 100X objective lenses, respectively. The ablation width of single scan for 20X lens was about 18 μm whereas it was 8.73μm for 100X objective lens since the dimension of focal point for 20X lens is greater than that for 100X lens. Based on this phenomenon, it can be concluded that the lens with higher magnification generally yields better resolution and accuracy of laser micromachining. However, magnification higher than necessary may induce problems such as longer processing time and higher sensitivity to the surface flatness as it requires much more precise match of the desired LAZ and the laser focal point, otherwise the laser beam will be out of focus. As a tradeoff, 50X was chosen in most of the experiments in this work.

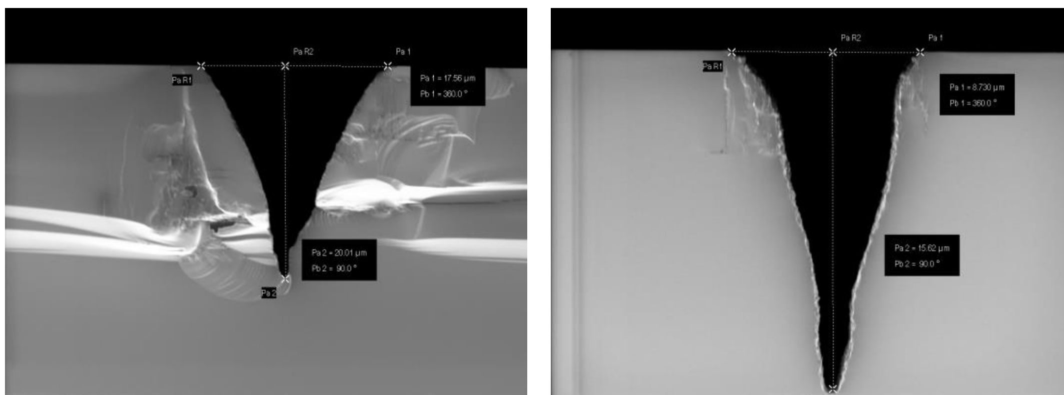

Figure 2.5. Cross-sectional SEM images for trenches formed by fs laser in DI water with scanning speed of 1 mm/s and pulse energy 4.32 μJ using objective lenses of (A) 20X. (B) 100X

Although it has been proved that 1 kHz fs laser pulses could minimize the thermal effects of the ablation process on various metal, dielectric, and semiconductor materials, very few works have provided a systematical study on femtosecond laser ablation on SiC, especially under water-assisted condition. Besides, a much higher repetition rate of pulses (121 kHz) in our experiment tends to result in thermal accumulation leading to a more remarkable melting-solidification phenomenon of the materials. Therefore, it is imperative to optimize the laser pulse energy and scanning speed, the two most important and sensitive parameters for the laser machining, to improve the ablation morphologies. A series of straight grooves were ablated by single scanning of the laser beam with varying pulse energy and scanning speed. Optical images combined as a single one for the scanning grooves with different pulse energy (0.83-4.32 μJ) and scanning speed (0.1-20 mm/s) are shown in Figure 2.6.

Figure 2.6. Optical images for the ablated grooves with different pulse energy and scanning speed. (from top to bottom: 0.83 μJ, 1.40 μJ, 2.23 μJ, 3.17 μJ, 3.80 μJ, 4.32 μJ; from left to right: 0.1 mm/s, 0.5 mm/s, 1 mm/s, 2 mm/s, 5 mm/s, 10 mm/s, 20 mm/s).

Figure 2.6 shows a general trend implying that for a given scanning speed, usually the continuous ablation is more possible as the laser pulse energy elevates whereas for a given pulse energy, ablation width decreases and eventually no obvious ablation takes place as the scanning speed increases. This is understandable since materials are easier to be ablated at higher power at a given speed but the number of absorbed laser pulses at a given region is reduced if the ablation becomes faster.

To put the explanation above into perspective, some data extracted from figure 2.6 was

plotted. Figure 2.7(A) shows the width and depth of the grooves ablated by the laser with different pulse energy ranging from 0.83–4.32 μJ at a translation speed of 1 mm/s. Both the width and depth of the grooves almost linearly increase as the pulse energy ramps up within the pulse energy range we tested. Meanwhile, the ablation width increases much faster than the ablation depth with respect to the laser fluence increase, since the femtosecond laser has a low thermal penetration depth, i.e. more localization of energy within the depth, whereas more debris generated from higher laser power assisted in more ablation in the surrounding regions. A similar trend was also observed with other translation speeds ranging from 0.1–20 mm/s. Figure 2.7(B) shows the width and depth of grooves ablated by the laser with scanning speeds at 0.1, 0.5, 1, 2, 5, 10, and 20 mm/s with a pulse energy of 2.23 μJ. This indicates that the ablated depth and width decrease with the increase in the scanning speed. As described above, during the line scanning process, fewer laser pulses would land on a unit area with a faster scanning speed, which results in a reduced ablation rate. In addition, the decreased rate in the ablation depth is significantly higher than that in the ablation width with increased scanning speed due to the lower thermal penetration depth, as this phenomenon was also found with decreased laser power.

Although high-power laser pulses provide a higher ablation rate, we found that lower laser pulse energy could cause fewer thermal effects as well as much better ablation quality. However, pulse energy lower than 0.83 μJ could not achieve a continuous kerf with measurable width and depth. Therefore, the critical pulse energy for our laser to produce a high-quality groove is considered to be 0.83 μJ, which is the value we used to fabricate microfluidic structures.

In addition, fast scanning can improve the fabrication efficiency but sacrifice the ablation quality, as demonstrated in figure 2.8. Figure 2.8(A) shows the SEM image of the feature after one ablation with pulse energy of 4.32 μJ at 20 mm/s, while figure 2.8(B) presents one of better quality

with the pulse energy of 1.40 μJ at 0.5 mm/s. No apparent ablation kerf was observed for higher power and scanning speed, whereas a clearly defined ablated path was formed after a single ablation at lower power and speed. Smooth ablation kerf is replaced with a thermally damaged feature if the scanning speed is not carefully calibrated.

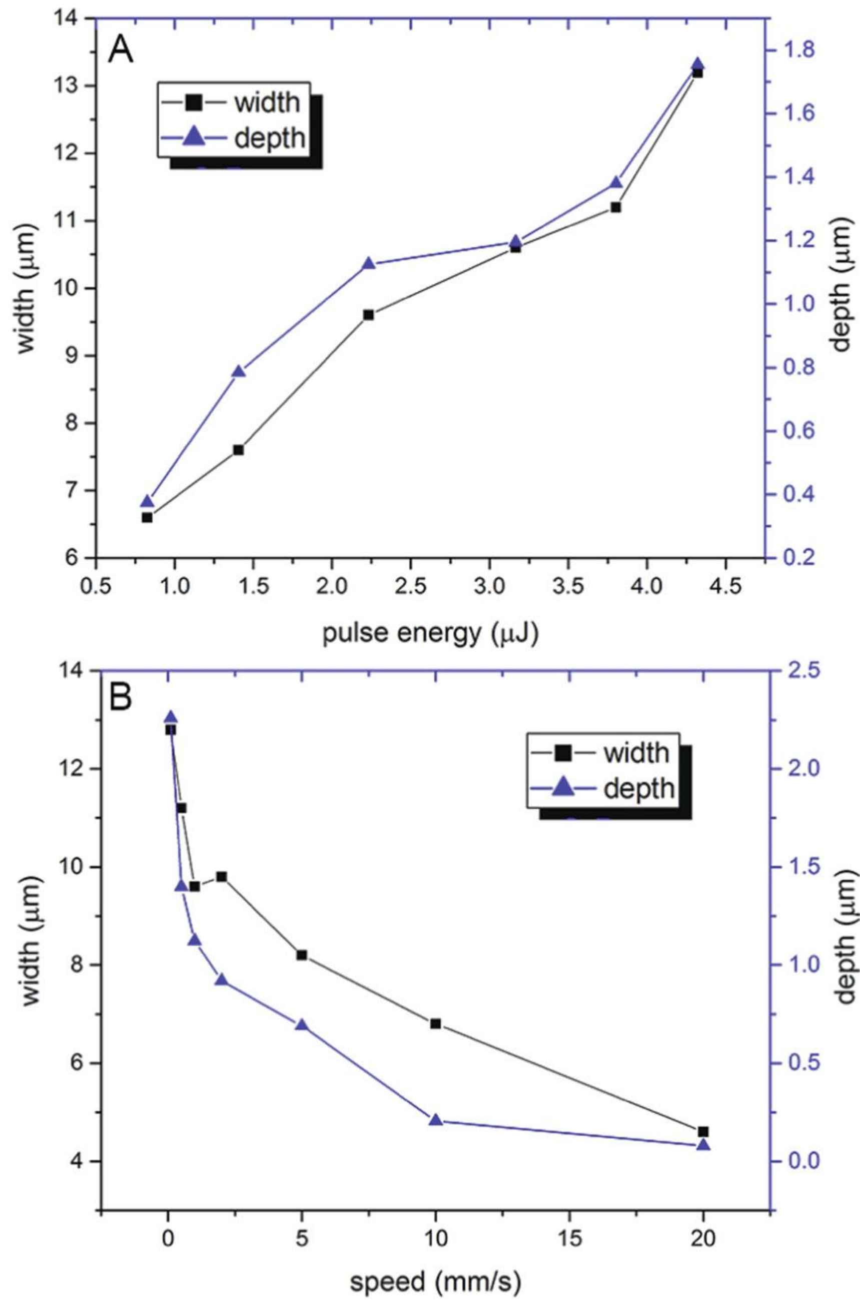

Figure 2.7. Dependence of the femtosecond laser ablation width and depth on the laser pulse energy (A) and scanning speed (B).

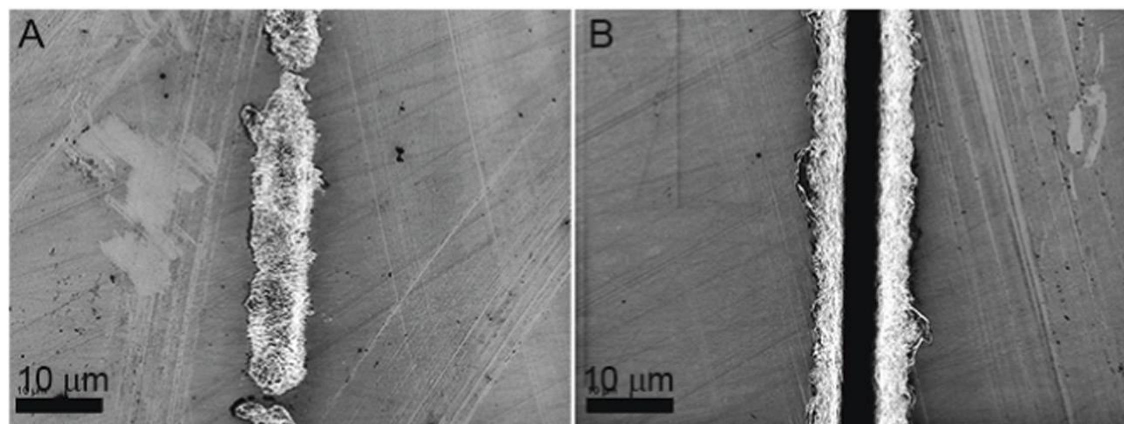

Figure 2.8. Ablated feature after a single ablation with different pulse energy and scanning speed. (A) Pulse energy: 4.32 μJ; speed: 20 mm/s. (B) Pulse energy: 1.4 μJ; speed: 0.5 mm/s.

2.3.3 Wettability of the Femtosecond Laser-Ablated Surface

The interfacial property of a microfluidic system interacting with the liquids chosen is critical, since it is directly linked to the smoothness, pressure, and velocity distribution of the liquid flow in the microchannels [32]. In the literature, the wetting property of SiC has been studied extensively for liquid metals [33], binary alloys [34], and even atomic nitrogen [35]. In our study, mineral oil was chosen as the liquid to flow in the microfluidic system for potential harsh environment applications since it has a relatively high boiling point, low thermal and electrical conductivity, and prevents the components of a fluidic system from corroding. The wettability of oil on a SiC surface has not been studied previously. Besides, compared with the lithography-based fabrication methods that produces smooth surfaces of the microchannels, the laser micromachining usually creates special micro- or even nano-structures during the laser-material interactions, which may significantly influence the interfacial properties of the microfluidic devices.

To explore the influence of the surface morphology induced by the laser ablation on the wettability of SiC, we measured the contact angle of mineral oil on the SiC substrate before and after the laser ablation. Figure 2.9(A) shows the smooth surface of the SiC substrate before laser treatment. The contact angle of the mineral oil is about 21°, indicating a wettable surface of SiC. Figure 2.9(B) illustrates the surface morphology of the SiC after the laser ablation. The laser-ablated surface shows sub-µm-scale periodic surface roughness compared with the intact surface, and the contact angle of the mineral oil on the laser-ablated SiC surface plummets to a mere 2.9°, which is expected, since the wettability of the surface with the given liquid is improved with increased roughness if the surface is wettable with the liquid [36]. The highly wettable characteristics of the oil in the LAZ reduces the pressure needed for it to be injected into and driven through the microfluidic channels. In contrast, the SiC sample surface is not highly hydrophilic for either the clean surface or the LAZ. While the contact angle of water on clean substrate is quite close to 90°, the roughened surface after laser treatment does not greatly increase the hydrophilicity as the contact angle is still close to 85°, indicating that the mineral oil is the more suitable fluid for SiC-based microfluidic systems.

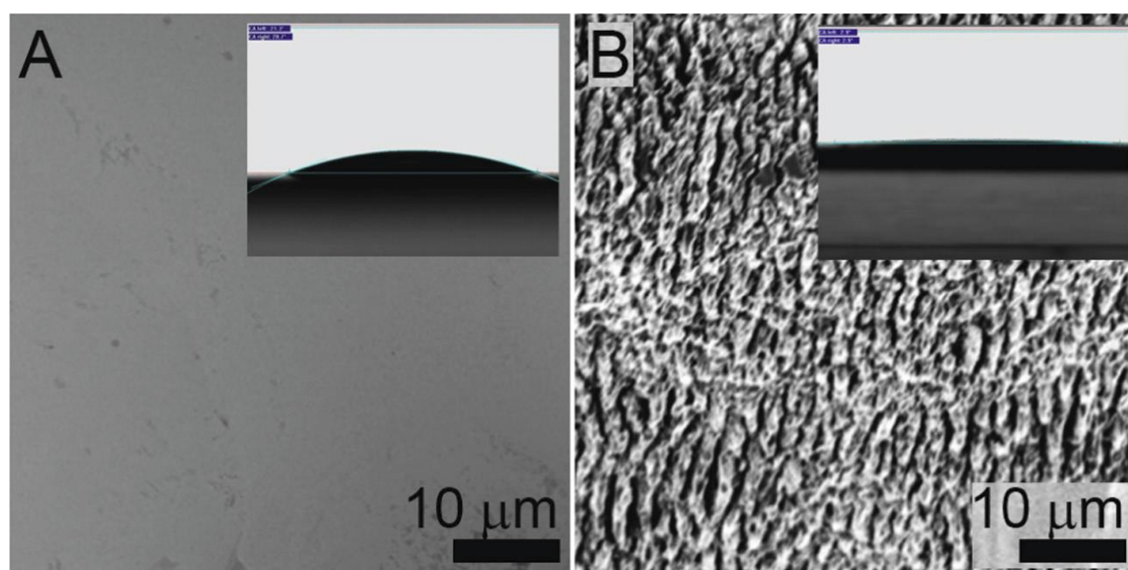

Figure 2.9. Surface morphology of SiC substrate (A) before and (B) after laser ablation. Inserts in (A) and (B) show the contact angle of mineral oil measured on the SiC surfaces.

2.3.4 Control of Cross-Sectional Shape of Microchannels

Compared with conventional photo-lithography patterning, which is only able to realize structures with uniform cross-sectional depth from one-time pattern transfer, the femtosecond laser micromachining not only has the advantage of no mask requirement and low cost but also possesses its capability of high-precision complex 3D structure manufacturing, including fabricating devices with various cross-sectional shapes. In general, the geometrical design of the cross-section of microchannels in a microfluidic MEMS system has substantial impact on the pressure [37] and flow velocity dynamics [38] of the liquid. Hence, it is indispensable to characterize the microchannels of various cross-sectional shapes during the design process of a microfluidic system.

The fabrication process for microchannels of various shapes was previously investigated. Maselli *et al* reported on a long microchannel with a circular shape on fused silica using femtosecond laser irradiation [39], Welin *et al* demonstrated water flows in trapezoidal silicon microchannels [40], Cheng *et al* varied the cross-sectional shape of microchannels in photostructurable glass [41]. Although microchannels of many regular or irregular shapes have been investigated, the target materials chosen for such studies mostly relied on conventional semiconductors such as silicon, common metals such as nickel and copper, and polymers such as PDMS. Here, we demonstrate microchannels of rectangular, semicircular, and triangular cross-sections in SiC by femtosecond laser micromachining and show the numerical simulations of corresponding cross-sectional velocity flow distributions.

In order to examine the morphology of the ablated surface in the designed structures, top-

view SEM images for the three aforementioned microchannels were obtained. Figures 2.10(A)–(C) show surface images for channels with cross-sectional rectangular, triangular, and semicircular shapes, respectively. All the microchannels are confined by the clear edges and relatively smooth transition inside their trenches. The raised stripes present in the three channels might be attributed to the slight turbulence of the flowing DI water that dispersed laser energy occasionally during the ablation process, which should be addressed in the future.

Figures 2.10(D)–(F) show the cross-sectional optical images of microchannels of rectangular, triangular, and semicircular shapes, respectively. The samples were processed on a program-controlled stage with a pulse energy of 2.23 μJ and a translation speed of 5 mm/s in DI water and with the target 0.1 mm deep. After the ablation process, the samples were rinsed with acetone in an ultrasonic bath for 5 min to remove any remaining debris. The microchannels were processed layer-by-layer with minimal thermal effect and cracking phenomenon.

In an effort to characterize the impact of cross-sectional geometry on the flow properties, Ansys Fluent 17.0 was utilized to simulate the steady-state cross-sectional velocity profile for the mineral oil. Since the Reynolds number is quite low in microscale channels, pressure driven laminar flow mode was selected. Figures 2.10(G)–(I) illustrate the cross-sectional velocity distribution for rectangular, triangular, and semicircular microchannels, respectively, with the initial velocity of 1 cm/s. The velocity of the oil near the walls of all three microchannels was set to zero with the assumption of no-slip boundary condition, as required by the basic law of fluid mechanics for pressure-driven laminar flow that produces a parabolic velocity distribution along the flowing direction within microchannels. However, due to the different shapes of the boundary walls, the transverse velocity profile can be squeezed to fit the cross-sectional configurations. Despite the similar trend that the closer the oil is to the center of the geometry, the faster it travels,

the area that represents the fastest flowing speed varies for the three microchannels under investigation. The flexibility of creating microchannels of various cross-sectional shapes by femtosecond laser micromachining widens the applications of microfluidics requiring unconventional or non-uniform flowing channels.

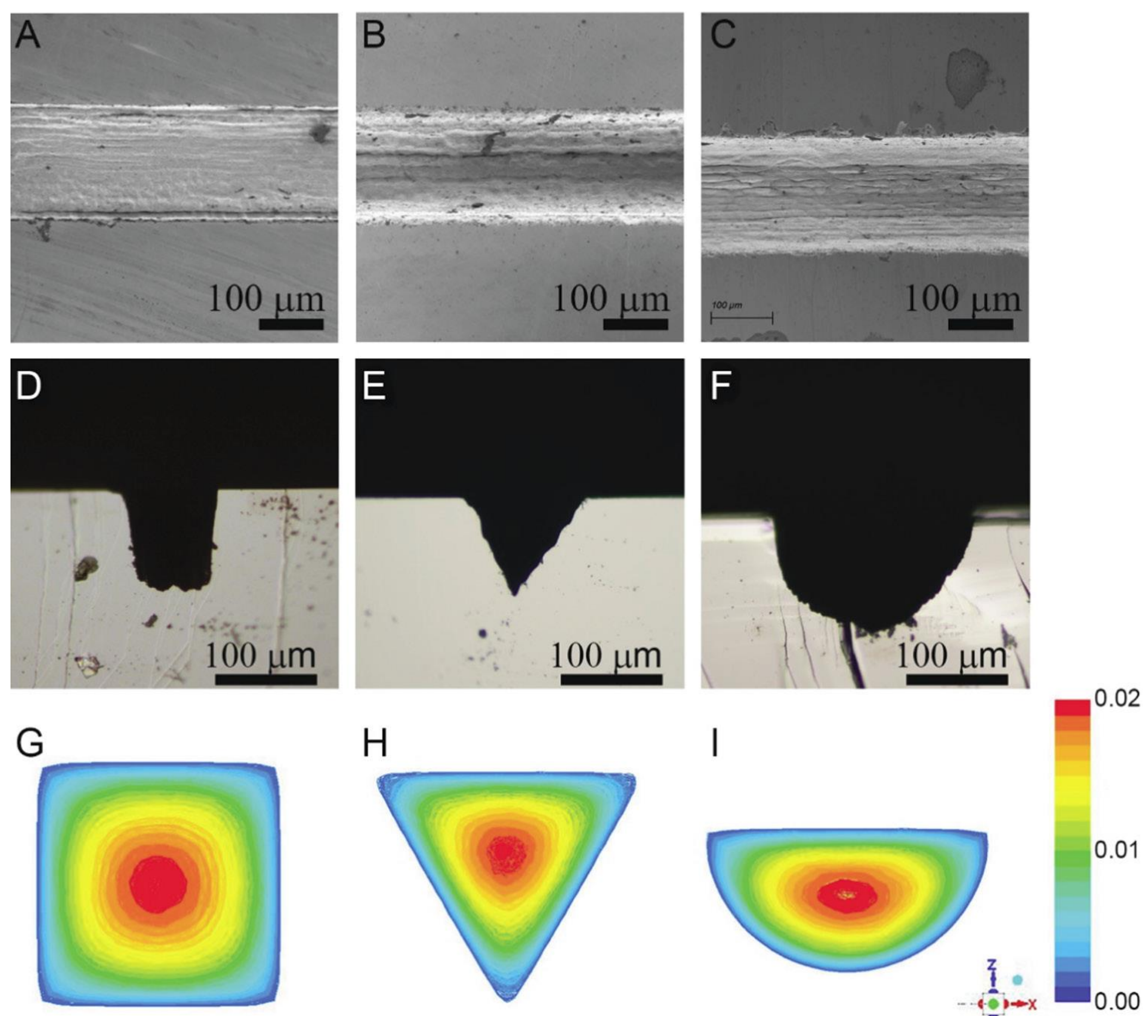

Figure 2.10. (A)–(C) Surface images of the microchannels with rectangular, triangular, and semicircular shapes, respectively. (D)–(F) Cross-sectional images of the microchannels with rectangular, triangular, and semicircular shapes, respectively. (G)–(I) Steady-state cross-sectional velocity profiles of microchannels with rectangular, triangular, and semicircular shapes, respectively.

2.3.5 Fabrication of Microchannels and Via Holes on SiC

It is necessary to utilize through-wafer structures when complex 3D microfluidics, such as wafer-to-wafer microfluidics, need to be built. In order to realize a through-wafer microfluidic system, femtosecond pulsed laser was used and the relevant parameters, i.e. translation speed and laser pulse energy, were tuned to obtain the best quality of the surface and through-wafer microchannels. The water film thickness was set slightly over 1 mm, which was found to be the optimal parameter for infrared pulse laser drilling of SiC in the water [31].

Figure 2.11 illustrates the morphology of the microchannels and the via manufactured by the femtosecond laser micromachining. Figure 2.11(A) presents the top view of a Y-channel with three legs of identical dimensions with sharp turns at the intersection and minimal thermal damage, indicating the high quality of the ablation by the femtosecond laser. The SEM image of the Y-channel in Figure 2.11(B) shows the morphology of the laser-ablated microchannel. The overall roughness is in the range of 800 nm – 1 μm and the micro- and nano-roughness on the sidewall and bottom of the microchannel could improve the wettability of the microfluidic channel, as demonstrated in the section 2.3.3. The images of the cross-section, top, and bottom view of the via hole are demonstrated in figures 2.11(C)–(E), respectively. The cross-sectional view indicates a vertical sidewall not readily possible with other manufacturing techniques within a reasonable processing time. The top and bottom views of the via show smooth and clear edges, indicating the minimized thermal damage of the water-assisted femtosecond laser-ablation process. The slightly wider opening of the surface is due to the higher susceptibility of the laser power near the surface region. The top and bottom of the via exhibit the same feature as the cross-section as well as the rough wall, as found in the microchannels on the surface.

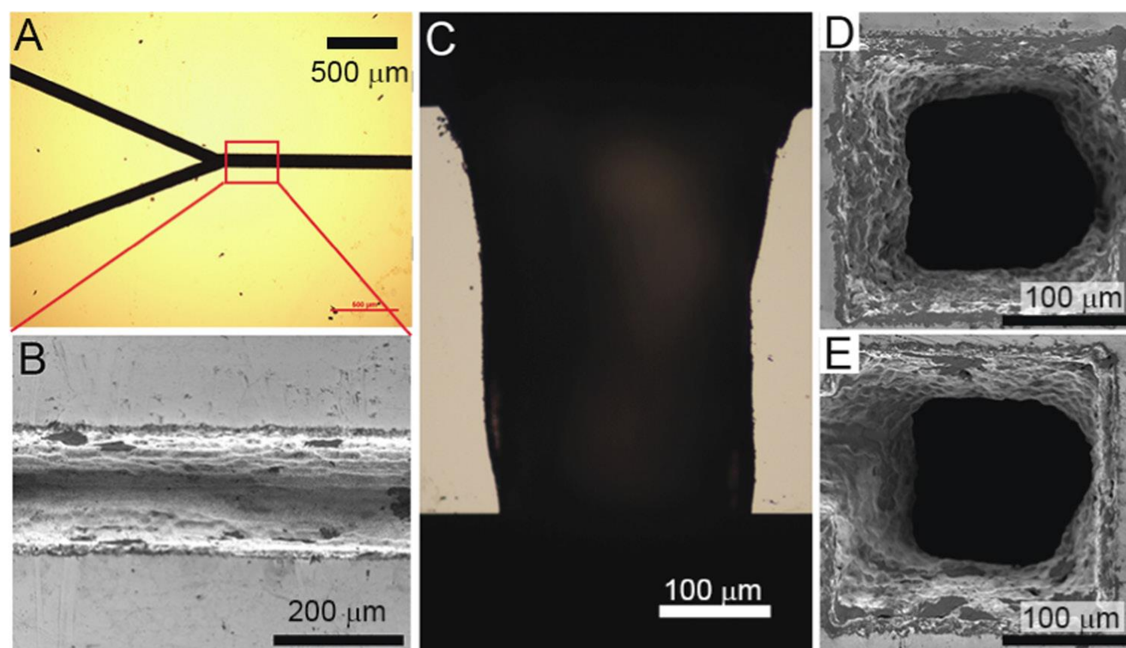

Figure 2.11. Fabricated surface microchannels and via hole on the SiC substrates. (A) and (B) Optical microscopic and SEM images of a Y-shaped microchannel, respectively. (C) Cross-sectional image of the via hole. (D) and (E) Top- and bottom-view SEM images of the via hole, respectively.

2.3.6 Z-Shaped Through-Wafer Microfluidic Device

Figures 2.12(A) and (B) shows a photo of a Z-shaped through-wafer microfluidic device and an image of the microfluidic channel, respectively. The straight microchannels on the top and the bottom of the SiC are 5 mm long, 0.1 mm wide, and 0.05 mm deep, while the width and depth of the via are 0.2 mm and about 0.35 mm, respectively.

Figures 2.12(C) and (D) demonstrate the oil flow in the bottom and top microchannels, respectively, from the optical microscope. The mineral oil was first mixed with the prepared fluorescent dye, then injected through the hole punched into the PDMS layer and finally the microchannels. Note that the bottom microchannel was displaced from the center of the via slightly to differentiate from the top for convenience of measurement. According to the microscopic image

showing the red color filling all areas of the top and bottom microchannels, a smooth liquid flow was achieved throughout the microfluidic channels.

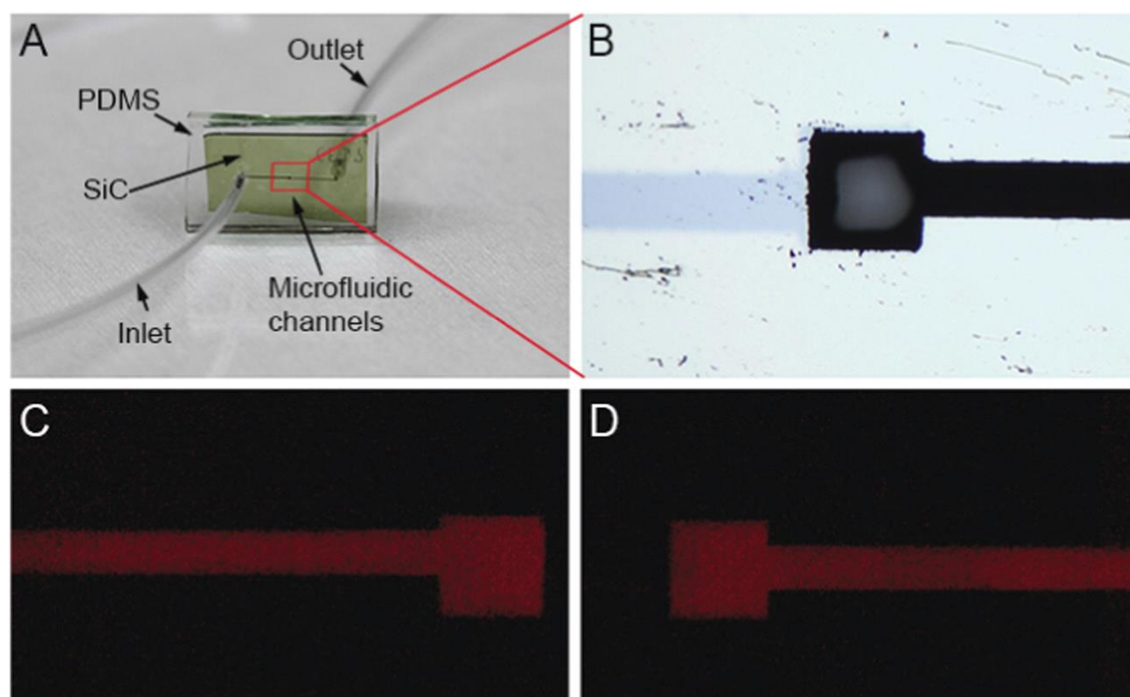

Figure 2.12. Z-shaped microchannel device demonstrated with mineral oil flowing with red fluorescent dye. (A) Photo of the Z-shaped microchannel device. (B) Image of the microchannels and via hole on the SiC substrate. (C) and (D) Images of the mineral oil flow with red fluorescent dye for bottom and top channels, respectively.

It is interesting to note, however, that the laser power slightly above the ablation threshold did not successfully yield the best quality microchannel in our experiments. From the previous studies, ablation from lower pulse energies, so long as it is above the threshold, creates cleaner features with less heat-affected zone formation and debris around the patterning areas. This was true in our study only when the ablation took place near the surface. When the ablation continued into the bulk SiC, the defect-activation process occurred, which drastically reduced the ablation threshold fluence [42]. Therefore, the laser power was tuned to a lower value after the ablation continued into the bulk to approximately retain the ablation width and depth for each single scan,

which in turn retained the target shape and dimension of the microchannels.

2.4 Conclusion

In conclusion, a prototype through-wafer microfluidic structure in a bulk 350 µm thick 4H–SiC wafer micromachined by a 1030 nm, 700 fs ultrafast femtosecond pulsed laser ablation system was demonstrated for the first time. A smooth oil flow in the microchannels was achieved, while it was found that the oil is highly attractive to the LAZ area of the SiC substrate. The high-quality microchannels with several different cross-sectional geometries were also realized by the femtosecond laser system and the flowing properties were studied as well. The dimension of the ablated kerf with respect to the speed of the relative motion between the laser focal spot and the sample, the laser pulse energy and the different objective lenses was also characterized. This study also indicates that the ultrafast femtosecond pulsed laser is a promising technique for high-precision 3D micromachining with minimal thermal damage for ultrahard materials. The manufactured through-wafer microfluidic system can be used in a harsh environment such as high temperature, corrosive media, high radiation, etc. It also paves the way for the SiC wafer bonding in the packaging of microfluidic MEMS devices to be used in harsh environments.

In the future, we plan to design more complex structures to realize more functionalities based on this system such as microfluidic structures with not only various cross-sectional shapes but curved channels and varied channel dimension along the direction of the fluid flow in the bulk SiC substrate that the conventional photolithography technique cannot accomplish. We also intend to investigate further the micro- and nano-particles generated from the ablation of SiC in the liquid-assisted environment. The critical speed for a given laser pulse energy has not been studied extensively, and has yet to be explored in more depth.

2.5 References

[1] Terry S C, Jerman J H and Angell J B 1979 A gas chromatographic air analyzer fabricated on a silicon wafer *IEEE Trans. Electron Devices* **26** 1880–6

[2] Nguyen N T and Wu Z G 2005 Micromixers—a review *J. Micromech. Microeng.* **15** R1–6

[3] Gunther A, Jhunjhunwala M, Thalmann M, Schmidt M A and Jensen K F 2005 Micromixing of miscible liquids in segmented gas-liquid flow *Langmuir* **21** 1547–55

[4] Garstecki P, Fischbach M A and Whitesides G M 2005 Design for mixing using bubbles in branched microfluidic channels *Appl. Phys. Lett.* **86** 244108

[5] Weibel D B, Kruithof M, Potenta S, Sia S K, Lee A and Whitesides G M 2005 Torque-actuated valves for microfluidics *Anal. Chem.* **77** 4726–33

[6] Laser D J and Santiago J G 2004 A review of micropumps *J. Micromech. Microeng.* **14** R35–64

[7] Unger M A, Chou H, Thorsen T, Scherer A and Quake S R 2000 Monolithic Microfabricated valves and pumps by multilayer soft lithography *Science* **288** 113

[8] Attia U M, Marson S and Alcock J R 2009 Micro-injection moulding of polymer microfluidic devices *Microfluid. Nanofluid.* **7** 1

[9] Garra J, Long T, Currie J, Schneider T, White R and Paranjape M 2002 Dry etching of polydimethylsiloxane for microfluidic systems *J. Vac. Sci. Technol.* A **20** 975–82

[10] Grosse A, Grewe M and Fouckhardt H 2001 Deep wet etching of fused silica glass for hollow capillary optical leaky waveguides in microfluidic devices *J. Micromech. Microeng.* **11** 257–62

[11] Van Lintel H, Vandepol F and Bouwstra S 1988 A piezoelectric micropump based on micromachining of silicon *Sensors Actuators* **15** 153–67

[12] Harrison D J, Manz A, Fan Z H, Ludi H and Widmer H M 1992 Capillary electrophoresis and sample injection systems integrated on a planar glass chip *Anal. Chem.* **64** 1926–32

[13] Duffy D C D, McDonald J C J, Schueller O J O and Whitesides G M G 1998 Rapid prototyping of microfluidic systems in poly(dimethylsiloxane) *Anal. Chem.* **70** 4974–84

[14] Young D J, Du J, Zorman C A and Ko W H 2004 Hightemperature single-crystal 3C–SiC capacitive pressure sensor *IEEE Sens. J.* **4** 464–70

[15] Srour J R, Marshall C J and Marshall P W 2003 Review of displacement damage effects in silicon devices *IEEE Trans. Nucl. Sci.* **50** 653–70

[16] Fassbender F, Schmitt G, Schöning M J, Lüth H, Buss G and Schultze J-W 2000 Optimization of passivation layers for corrosion protection of silicon-based microelectrode arrays *Sensors Actuators* B **68** 128–33

[17] Casady J B and Johnson R W 1996 Status of silicon carbide (SiC) as a wide-bandgap semiconductor for hightemperature applications: a review *Solid-State Electron.* **39** 1409–22

[18] Mehregany M, Zorman C A, Roy S, Fleischman A J, Wu C-H and Rajan N 2000 Silicon carbide for microelectromechanical systems *Int. Mater. Rev.* **45** 85–108

[19] Nabki F 2009 Silicon carbide micro-electromechanical resonators for highly integrated frequency synthesizers *PhD Thesis* McGill University (http://digitool.library.mcgill.ca/R/NR8CV9GJDCC5ECCQUJ6ES6RLAQ8TJ5Y1VKDKC1QVS1RUSXG47P-03355?func=results-brief)

[20] Jin S, Rajgopal S and Mehregany M 2011 Silicon carbide pressure sensor for high temperature and high pressure applications: influence of substrate material on performance *16th Int. Solid-State Sensors, Actuators and Microsystems Conf.* pp 2026–9

[21] Nishino S, Powell1 J A and Will H A 1983 Production of large-area single-crystal wafers of cubic SiC for semiconductor devices *Appl. Phys. Lett.* **42** 460

[22] Zhuang D and Edgar J H 2005 Wet etching of GaN, AlN, and SiC: a review *Mater. Sci. Eng.* R **48** 1–46

[23] Senesky D G and Pisano A P 2010 Aluminum nitride as a masking material for the plasma etching of silicon carbide structures *IEEE 23rd Int. Conf. on Micro Electro Mechanical Systems (MEMS) (Wanchai, Hong Kong)* pp 352–5

[24] Zhang J, Sugioka K, Wada S, Tashiro H and Toyoda K 1997 Direct photoetching of single crystal SiC by VUV-266 nm multiwavelength laser ablation *Appl. Phys.* A **64** 367–71

[25] Zhang J, Sugioka K, Wada S, Tashiro H, Toyoda K and Midorikawa K 1998 Precise microfabrication of wide band gap semiconductors (SiC and GaN) by VUV–UV multiwavelength laser ablation *Appl. Surf. Sci.* **127–9** 793–9

[26] Chichkov B N, Momma C, Nolte S, von Alvensleben F and Tünnermann A 1996 Femtosecond, picosecond and nanosecond laser ablation of solids *Appl. Phys. A Mater. Sci. Process.* **63** 109–15

[27] Dong Y 2004 Femtosecond pulsed laser ablation and patterning of 3C–SIC films on SI substrates for MEMS fabrication *PhD Thesis* Iowa State University (http://lib.dr.iastate.edu/cgi/viewcontent.cgi?article=2153&context=rtd)

[28] Luan Q, Jia Y, Wang Y, Akhmadaliev S, Zhou S, Vázquez de Aldana J R, Tan Y and Chen F 2014 Optical ridge waveguides in 4H–SiC single crystal produced by combination of carbon ion irradiation and femtosecond laser ablation *Opt. Mater. Express* **4** 1166–71

[29] Khuat V, Ma Y, Si J, Chen T, Chen F and Hou X 2014 Fabrication of through holes in silicon carbide using femtosecond laser irradiation and acid etching *Appl. Surf. Sci.* **289** 529–32

[30] Li C, Shi X, Si J, Chen T, Chen F, Liang S, Wu Z and Hou X 2009 Alcohol-assisted photoetching of silicon carbide with a femtosecond laser *Opt. Commun.* **282** 78–80

[31] Iwatani N, Doan H D and Fushinobu K 2014 Optimization of near-infrared laser drilling of silicon carbide under water *Int. J. Heat Mass Transfer* **71** 515–20

[32] Stone H A, Stroock A D and Ajdari A 2004 Engineering flows in small devices: microfluidics toward a lab-on-a-chip *Annu. Rev. Fluid Mech.* **36** 381–411

[33] Liu G W, Muolo M L, Valenza F and Passerone A 2010 Survey on wetting of SiC by molten metals *Ceram. Int.* **36** 1177–88

[34] Naidich Y V, Zhuravlev V and Krasovskaya N 1998 The wettability of silicon carbide by Au–Si alloys *Mater. Sci. Eng.* **A245** 293–9

[35] Galli G, Catellani A and Gygi F 1999 Wetting silicon carbide with nitrogen: a theoretical study *Phys. Rev. Lett.* **83** 2006–9

[36] Kubiak K J, Wilson M C T, Mathia T G and Carval P 2011 Wettability versus roughness of engineering surfaces *Wear* **271** 523–8

[37] Akbari M, Sinton D and Bahrami M 2009 Pressure drop in rectangular microchannels as compared with theory based on arbitrary cross section *J. Fluids Eng.* **131** 041202

[38] Tsai C-H, Tai C-H, Fu L-M and Wu F-B 2004 Experimental and numerical analysis of the geometry effects of low-dispersion turns in microfluidic systems *J. Micromech. Microeng.* **15** 377–85

[39] Maselli V, Osellame R, Cerullo G, Ramponi R, Laporta P, Magagnin L and Cavallotti P L 2006 Fabrication of long microchannels with circular cross section using astigmatically shaped femtosecond laser pulses and chemical etching *Appl. Phys. Lett.* **88** 191107

[40] Weilin Q, Mala G M and Dongqing L 2000 Pressure-driven water flows in trapezoidal silicon microchannels *Int. J. Heat Mass Transfer* **43** 353–64

[41] Cheng Y, Sugioka K, Midorikawa K, Masuda M, Toyoda K, Kawachi M and Shihoyama K 2003 Control of the cross-sectional shape of a hollow microchannel embedded in photostructurable glass by use of a femtosecond laser *Opt. Lett.* **28** 55–7

[42] Dong Y and Molian P 2003 Femtosecond pulsed laser ablation of 3C–SiC thin film on silicon *Appl. Phys.* A **77** 839–46

CHAPTER 3

Lateral Dye-Sensitized Microscale Solar Cells via Femtosecond Laser Patterning

Part of the contents in this chapter has been published as:

X. Zhang, Y. Huang, H. Bian, H. Liu, X. Huang, and H. Jiang, "Lateral dye-sensitized microscale solar cells via femtosecond laser patterning," ***Advanced Materials Technologies*****, Vol. 1, No. 6, article no. 1600121, 2016.**

In this chapter, femtosecond (fs) laser is employed to fabricate compact lateral Dye-sensitized solar cells (DSSCs) with fill factor (FF) double than that for the lateral solar cells previously reported. The photon-to-electron efficiency reaches 5.18% which is also significantly higher than the other lateral solar cells. The fs pulsed laser is used to cut through the TiO_2 film and the Fluorine doped Tin Oxide (FTO) Glass layer to create an interdigital pattern resulting in the base for two electrodes, photoelectrode (PE) and counter electrode (CE). Such a structure inherently overcomes the difficulty of truly achieving lateral charge carrier transport associated with the lateral DSSCs previously reported. The structural design, fabrication process, and the device performance are presented.

3.1 Introduction

Low cost, high efficiency, long-term stability, and excellent scalability are features that researchers always pursue for solar cells. Dye-sensitized solar cells (DSSCs) are considered to have a great potential to achieve all these goals [1,2]. Conventional DSSCs have a sandwiched structure in which charge transport occurs perpendicular to the device surface, as shown in figure 3.1(a). Recently, solar cells with lateral structures [3–8] have caught much attention owing to the following advantages in comparison with the conventional vertical structure: (a) The requirement of the transparency of the electrode can be eliminated; both electrodes can be placed at the back side and use high-conductivity materials, while the light can be incident from the front. As a result, transmission loss can be reduced and the charge collection increased simultaneously. (b) Compact device structure can be realized that is more conducive to scaling up, integration, and functionalization. (c) Flexible devices are feasible. Lateral DSSC is, therefore, a concept of advanced structure of DSSCs with lateral transport of charges, as shown in figure 3.1(b). A few structures have been proposed in this direction. Back-contact structure, which leads both photoelectrode (PE) and counter electrode (CE) to the back side of the device, was developed from monolithic structure [9] to interdigital structure [10,11] in recent years, as shown in Figure 3.1(c) and (d), respectively. In a back-contact DSSC in figure 3.1(d), CE of Pt/fluorine-doped tin oxide (FTO) was interdigitally patterned and separated from PE made of TiO_2, which was about 10 μm thick and not patterned [10]. Therefore, most of the photo-induced charges still transport vertically in such back-contact structure, while a small number of carriers transport laterally in a limited region near PE, which has a nanoscale thickness. Li et al. reported a DSSC structure that realized lateral PE-CE separation (figure 3.1(e)), which is by far the closest structure to the lateral DSSCs [3]. However, in their structure, the Pt layer has intrinsically nanoscale thickness, which is much

less than the thickness of the neighboring PE. Such structure along with the limited PE material of ZnO nanowire resulted in a low performance of the solar cell. In this study, we accomplished lateral DSSCs with patterned PE and CE as shown in figure 3.1(b).

Currently, the research on lateral structures for the emerging new-generation solar cells other than DSSCs, including organic photovoltaics (OPVs) and perovskite solar cells (PSCs), is also being conducted. Nevertheless, the best photon-to-electron conversion efficiency (η) of these lateral solar cells is still very low: 0.5% for OPVs [5] and 1.88% for PSCs [7]. Lateral DSSC is not an exception, with η less than 1% [3]. One of the common issues of these low-efficiency lateral solar cells is their low fill factor (FF) of less than 0.3 [3–8]. It indicates that the fundamental problem of great internal loss in these lateral structures is still hard to overcome. In this work, we utilized the powerful femtosecond (fs) laser to directly pattern nano-TiO_2/FTO photoelectrode into microscale units and successfully obtained lateral DSSCs with the best η of 5.18%, much better than the previously reported lateral solar cells. FF achieved from this lateral DSSC was nearly 0.6.

Fs laser ablation has proven to be a convenient and effective method to create micro- or nano-structures in bulk materials [12–15] and nano materials [16–18], and is especially advantageous to create high aspect ratio structure [15]. In this study, we utilized fs laser to cut through the nano-porous TiO_2 film on the FTO glass substrate and scan within the TiO_2 region to construct an interdigital pattern, where the used-to-be PE was divided into two electrodes, both consisting of microscale fingers. One of the separated electrodes was deposited with Pt by electrodeposition to form the CE of the lateral DSSC, while the other electrode was loaded with dye molecules as the PE. The ion transport between neighboring PE and CE fingers is thus in a completely lateral mode, as shown in Figure 3.1(b). One such solar cell is formed by a number of subcells with microscale fingers, the merit of which lies in that the subcells could be rearranged

and connected for functionalization as individual microscale modules [19,20]. The spacer-free structure could avoid possible contact in practice between the electrodes. The lateral PE-CE structure of nanostructured TiO_2 could also be directly implemented in quantum dot-sensitized solar cells (QDSSCs) [21] that possess a very similar device structure to that of DSSCs. This compact lateral design could substantially reduce the structural complication of devices such as tandem solar cells [22,23] and hybrid solar energy harvesting/storage devices [24,25].

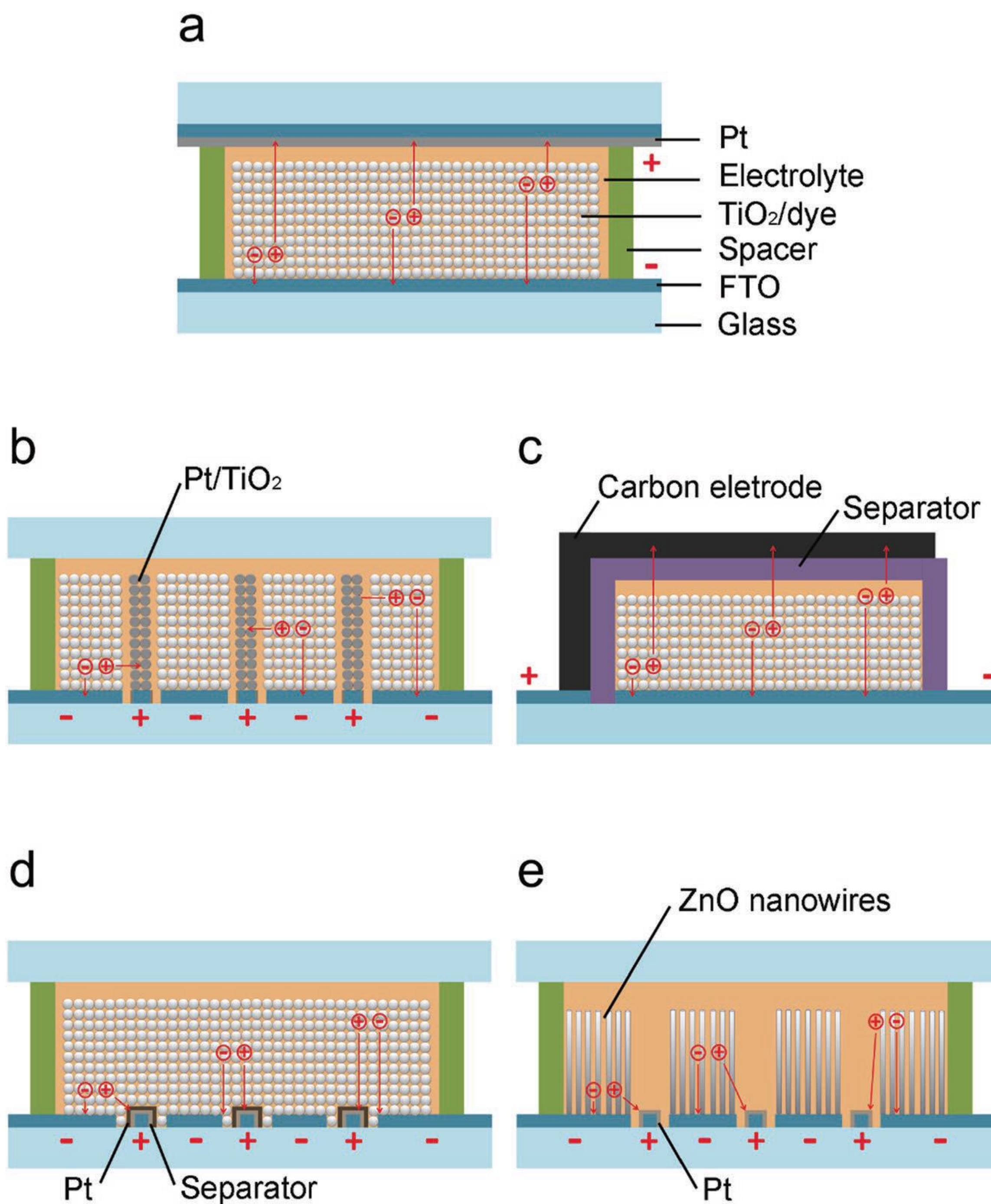

Figure 3.1. a) Conventional sandwich-structured DSSC, b) lateral DSSC with patterned PE (−) and CE (+), c) monolithic back-contact DSSC, d) back-contact DSSC with patterned CE, e) lateral DSSC with hierarchical PE and CE. Photogenerated positive and negative charges are shown in each structure.

3.2 Fabrication and Sample Morphology

The fabrication process of the lateral DSSCs is shown in figure 3.2(a–e). The 10 μm thick nanostructured TiO_2 film was deposited onto an FTO glass substrate first, followed by sintering at 500 °C, as shown in figure 3.2(a). Using a laser ablation system, linearly polarized 700 fs laser pulses were transmitted through an objective lens and subsequently focused onto the sample surface with a fixed spot size. The optimized pulse energy is 4.2 μJ, which could adequately cut through the TiO_2/FTO layer all the way to the glass substrate. An interdigital pattern was defined with the width of a PE finger (100 μm) larger than that of a CE finger (35 μm). By scanning the laser beam along the programmed paths as shown in figure 3.2(b), PE and CE were separated and isolated. The scanning electron microscopy (SEM) image of the part of patterned TiO_2/FTO glass is shown in Figure 3.2f, while the microscopic image of the whole film is shown in figure 3.3. The cross-sectional SEM images in figures 3.4(a) and (b) show that the fs laser formed a V-shaped profile all through the TiO_2 layer. The width at the top of the TiO_2 film was 8.3 μm, while the width at the bottom was 2.9 μm. The average spacing between neighboring PE and CE fingers was about 5.6 μm, lower than the spacing (typically ≈15 μm) between the vertical PE and CE in conventional DSSCs. This smaller spacing could improve the ion transport in the electrolyte of DSSCs, and contribute to the improvement of the overall performance [26]. The morphology detail near the ablated region in figures 3.4(b) and (c) show that most of the ablated TiO_2 particles with a laser pulse energy of 4.2 μJ were removed, and no distinct damage or alteration to the nano-porous TiO_2 could be observed. An X-ray diffraction (XRD) characterization of the TiO_2 nanoparticles before and after the ablation at 4.2 μJ pulse energy shows that ablation under such level of pulse energy did not change the anatase lattice as shown in figure 3.5.

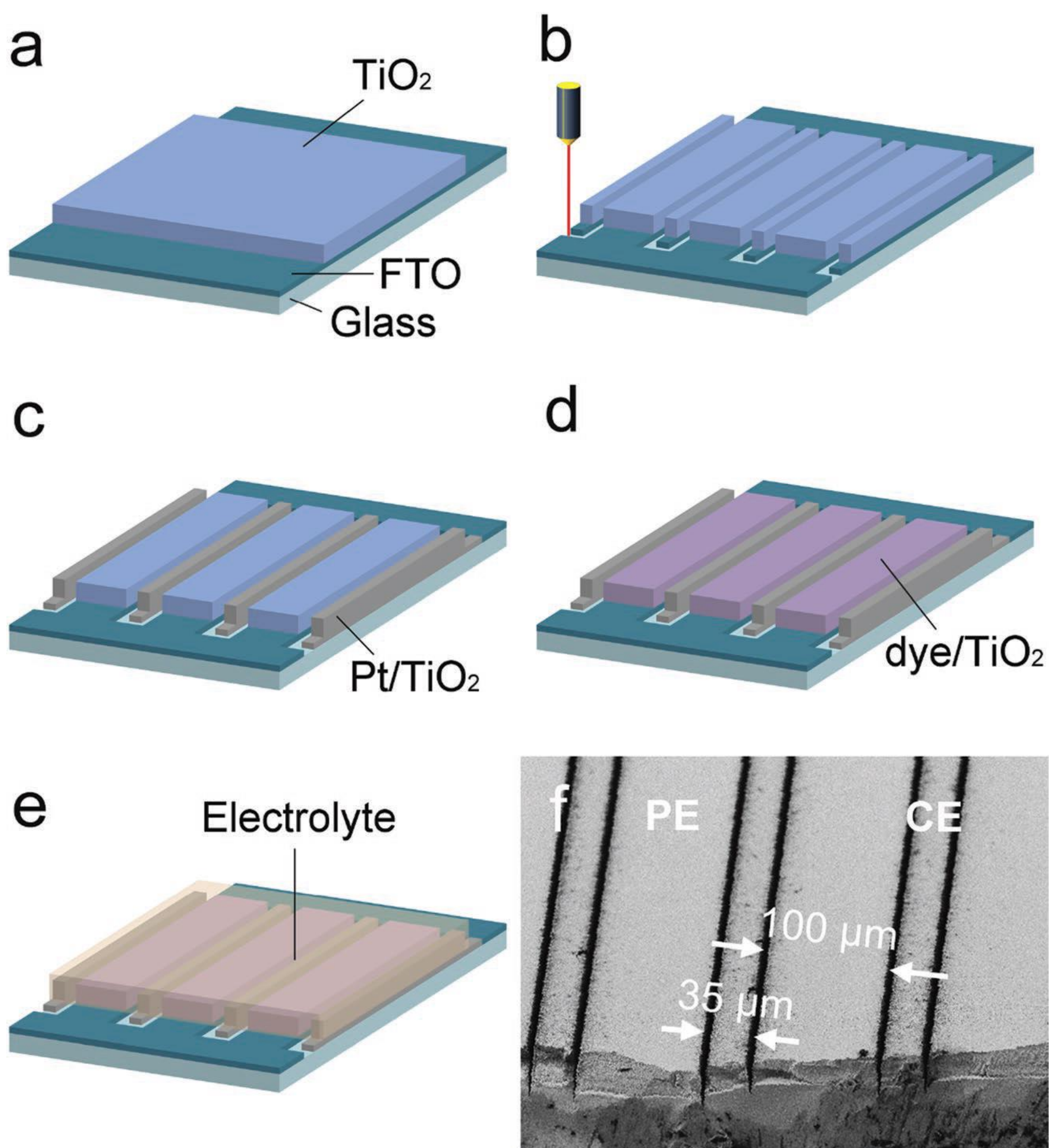

Figure 3.2. Schematics of the fabrication process of the lateral DSSC: a) nanostructured TiO_2 film deposited on FTO glass, b) TiO_2/FTO patterned by femtosecond laser ablation, c) electrodeposition of Pt on CE fingers, d) dye-loading on PE fingers, e) electrolyte filling and device sealing. f) SEM image of the tilted top view of the laser-patterned TiO_2 film, where the widths of patterned fingers are labeled.

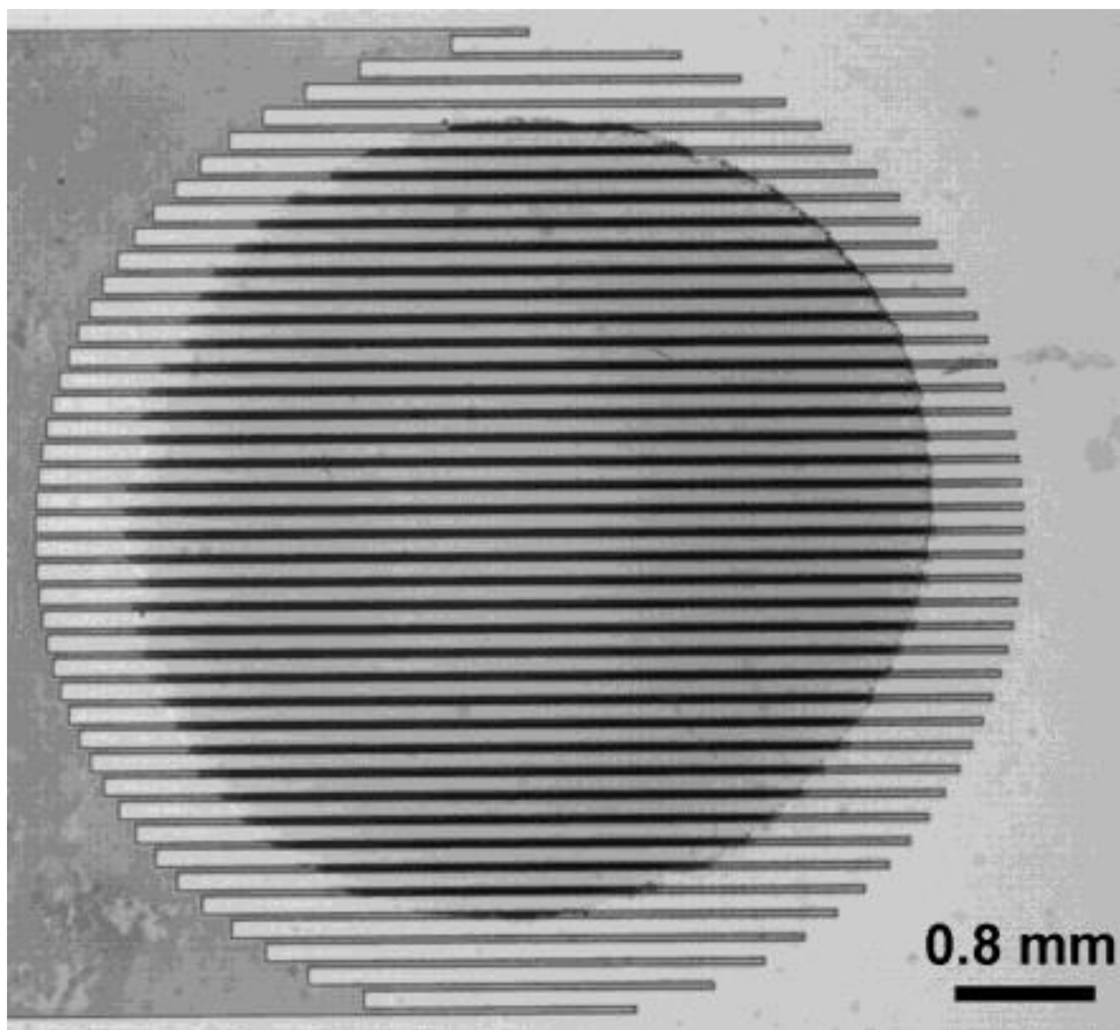

Figure 3.3. Microscopic image of laser-patterned TiO_2 film on FTO glass with CE deposited with Pt for lateral DSSC

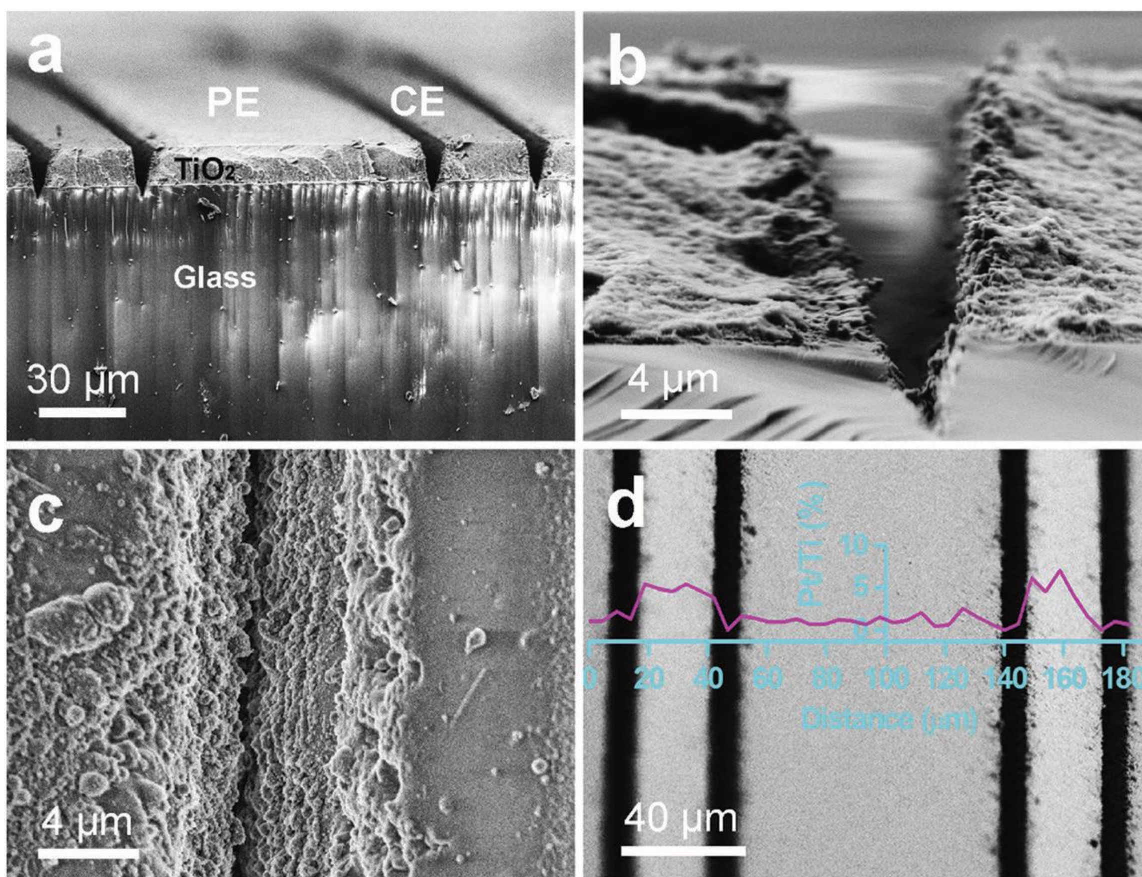

Figure 3.4. a) Cross-sectional SEM image of laser-patterned TiO_2 film, where CE fingers are deposited with Pt. Cross-sectional and top view images of one ablation channel are shown in b,c), respectively. d) Top view SEM image of patterned TiO_2 film with Pt, where the line-scanning curve of EDS is shown, with the atomic ratio of Pt/Ti as the y-axis. After the laser ablation process, the Pt and organic dye were loaded to CE and PE electrodes, respectively.

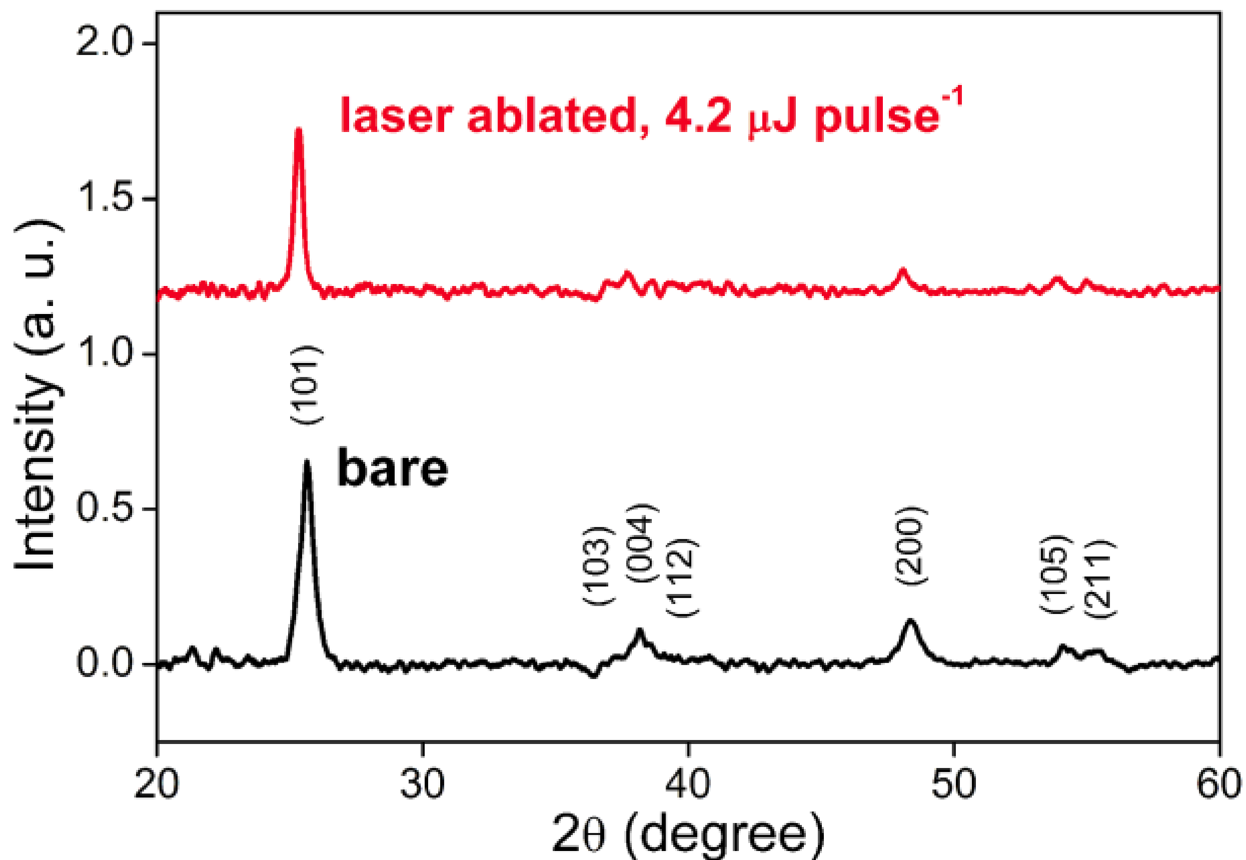

Figure 3.5. XRD spectra of nanostructured TiO_2 film before and after laser ablation with pulse energy of 4.2 μJ.

Next, the patterned region of the sample was dipped into a $PtClO_4$ aqueous solution to deposit Pt onto the narrow CE fingers, as shown in Figure 3.2(c). Pt was deposited onto the CE of the film under three 2V-constant-bias pulses (pulse width: 10 s, rest time: 30 s) via an electrodeposition process. The films were subsequently sintered at 500 °C for one hour. To characterize the deposited Pt on CE fingers, energy dispersive x-ray spectrometry (EDS) analysis was performed. The line-scanning on the top surface of the TiO_2 film was conducted and the results are shown in figure 3.4(d). Most of the Pt was distributed on the CE area between the two ablated channels, with a portion of about 6% in comparison with Ti. Pt also appeared at the edge of the PE, but with limited width of about 3 μm. Hence Pt could be well controlled to be loaded only

onto the narrow TiO_2 fingers as CE of the lateral DSSC. This Pt deposition process is sensitive to the laser-patterning with microscale spacing between neighboring PE and CE fingers. When the laser energy is lower, this spacing is reduced. However, too small a spacing could result in short-circuit by the $PtClO_4$ solution during the electrodeposition and some of the Pt could be deposited onto the PE fingers which would have a negative impact on the device performance, as shown in figure 3.6 in which two samples processed with different pulse energy were compared. Figures 3.6(a) and (b) are the cross-sectional SEM images for samples ablated by pulse energy of 4.2 μJ and 3.4 μJ, respectively showing that 3.4 μJ yields much narrower spacing between the PE and CE electrodes. Figures 3.6(c) and (d) are the microscopic images after Pt deposition for the the two samples with 4.2 μJ and 3.4 μJ, respectively. As can be clearly seen, the sample processed by pulse energy of 3.4 μJ shown in figure 3.6(d) has apparent undesirable deposition of Pt on PE fingers that degrades the solar cell performance as indicated in figure 3.6(e). The efficiency is reduced by almost 2% with 3.4 μJ meaning the appropriate selection of the ablation pulse energy is critical in achieving best results. On the other hand, it was found that higher laser pulse energy such as 4.6 μJ under the same conditions cracked the TiO_2 film, hence the optimal pulse energy chosen to fabricate our lateral DSSCs was determined to be 4.2 μJ.

Then, the PE was loaded with a type of organic dye RK1 with superior performance when exposed to light with wavelengths below 600 nm, and finally the film was filled with electrolyte and sealed after the Pt deposition, as shown in figure 3.2(d)-(e).

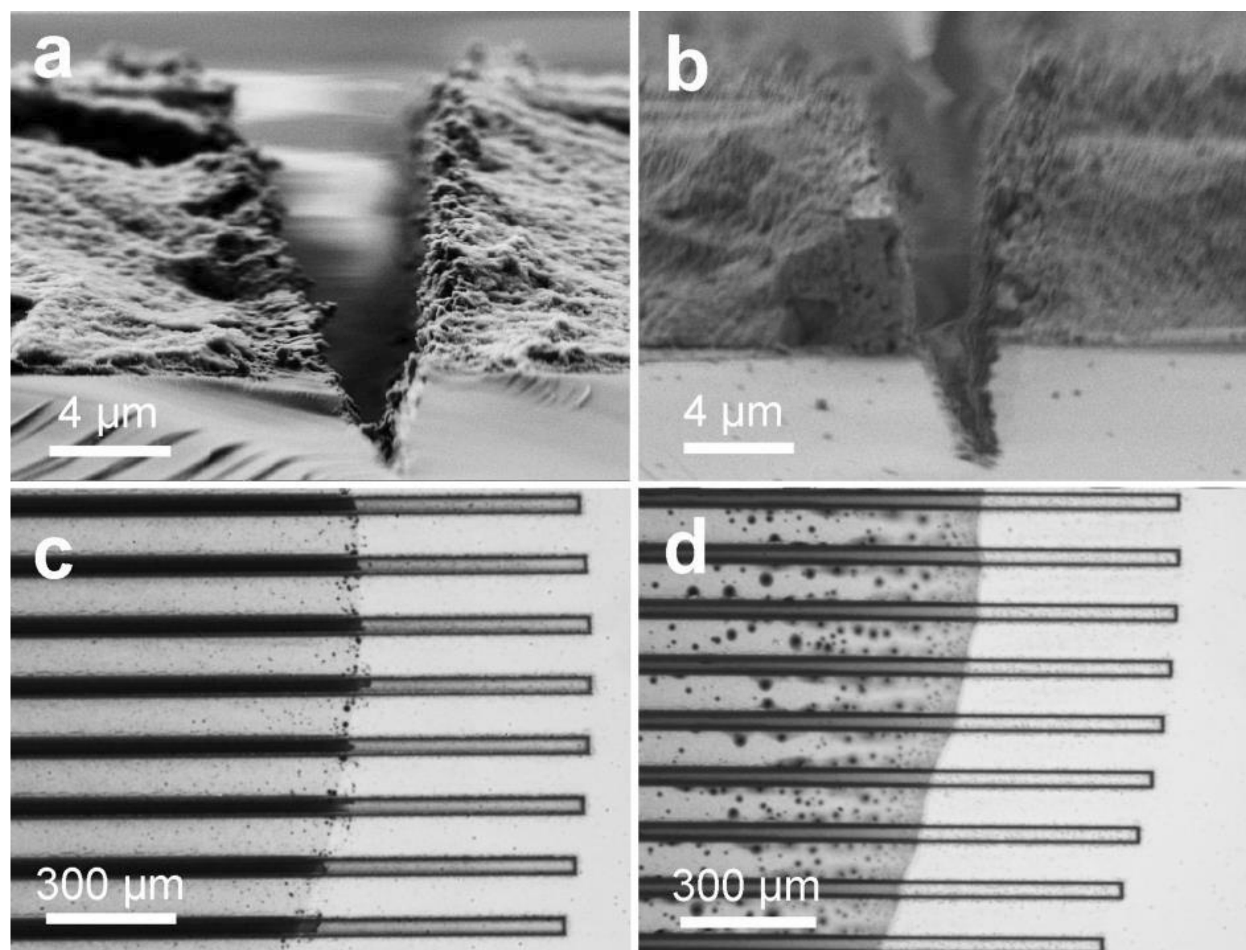

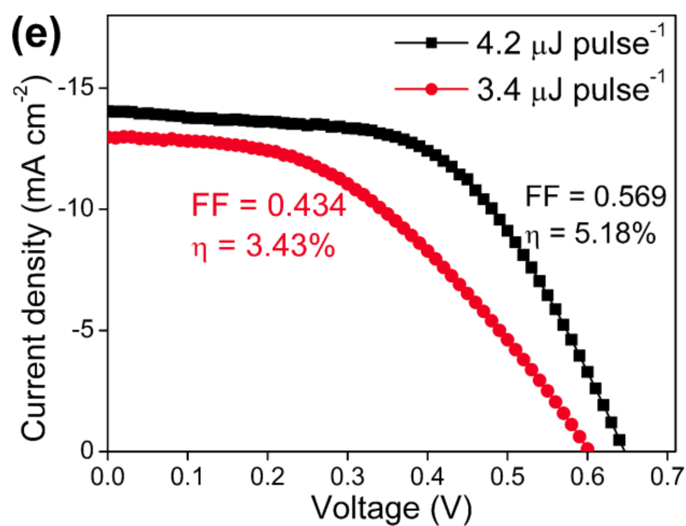

Figure 3.6. Effect of different laser pulse energy (4.2 μJ pulse vs. 3.4 μJ pulse) on the width of the ablated channels (a) & (b), Pt deposition (c) & (d) for 4.2 μJ and 3.4 μJ, respectively and (e) resultant performance of the two lateral DSSCs.

3.3 Results and Discussion

The device performance in terms of fill factor (FF) in the current density-voltage (J-V) curves and incident photon-to-current efficiency (IPCE) was measured and compared for our lateral DSSC and a reference DSSC with conventional structure under AM 1.5G illumination. For the tests of the lateral DSSC device, the light was incident from the back side of the device. The photocurrent density, short-circuit photocurrent density (J_{sc}), and η of each lateral cell in this work were calculated based on the area of the PE region only, where the incident light is absorbed and converted to carriers. Hence the defined internal J_{sc} and η for lateral DSSCs reflect the real photon-to-electron conversion performance of the PE material with the crucial results summarized in Table 3.1 below.

Solar Cell	V_{oc} (V)	J_{sc} (mA/cm^2)	FF (%)	η (%)
Reference	0.70	15.0	68.7	7.20
Our Device	0.65	14.0	56.9	5.18

Table 3.1. Open-circuit voltage, short-circuit current density, fill factor and efficiency of reference and our DSSCs where J_{sc} and η of lateral cells were calculated based on the area of PE, which is 74% of the device area exposed to the AM 1.5G illumination

If the CE fingers exposed to the incident light are also included in the calculation with no photocurrent generated, the values of external J_{sc} and η of the said devices should be reduced by 26% due to the area ratio of 35:100 for CE and PE fingers. To increase the absorption efficiency of incident photons and thus increase the overall efficiency, the area portion of CE in the design should be as low as possible while ensuring its function as the fs laser ablation has a limit on how narrow a ridge structure can be defined. Such lateral structure is especially suitable for the PV system with concentrators [19], where the photon loss caused by CE could be completely avoided.

Table 3.2 shows the comparison of short-circuit current density and efficiency for the lateral DSSCs considering only the PE area and whole area exposed to incident light (w-J_{sc} and w- η).

Solar Cell	J_{sc} (mA/cm^2)	w-J_{sc} (mA/cm^2)	η (%)	w-η (%)
Lateral DSSC	14.0	10.4	5.18	3.84

Table 3.2. Conversion table of J_{sc} and η using PE area or whole exposed area (w-J_{sc} and w-η) for lateral DSSCs.

Figure 3.7 shows the J-V characteristics and the IPCE with respect to the spectra of 400nm – 750nm. J_{sc} of the desgined lateral solar cell is close to that of the reference DSSC with the same dye and PE material/thickenss, indicating that the laser ablation process preserved the performance of PE material. The slightly lower FF infers that the charge recombination and internal loss in the cell are slightly higher than the conventional DSSC that might stem from the edges of the CE fingers affected by the laser pulses and still some, albeit not much, Pt was deposited on the PE fingers as shown in figure 3.4(d). However, the performance of this lateral DSSC is significantly improved compared with the lateral DSSC previously reported in Reference [3] and much better than that of other types of lateral solar cells [4-8] with low FF values. The shape of IPCE response curve with respect to the spectra remains the same. The IPCE decay of the lateral DSSC seems larger than the J_{sc} reduction in figure 3.7(a). This is because the IPCE spectrum of the lateral DSSC was obtained based on the whole area of the incident light spot, which contains the areas of both PE and CE. Therefore, the real IPCE values afforded by the PE of the lateral DSSC should be 1.35 times of the result in figure 3.7(b), and should be much closer to the IPCE of the reference DSSC.

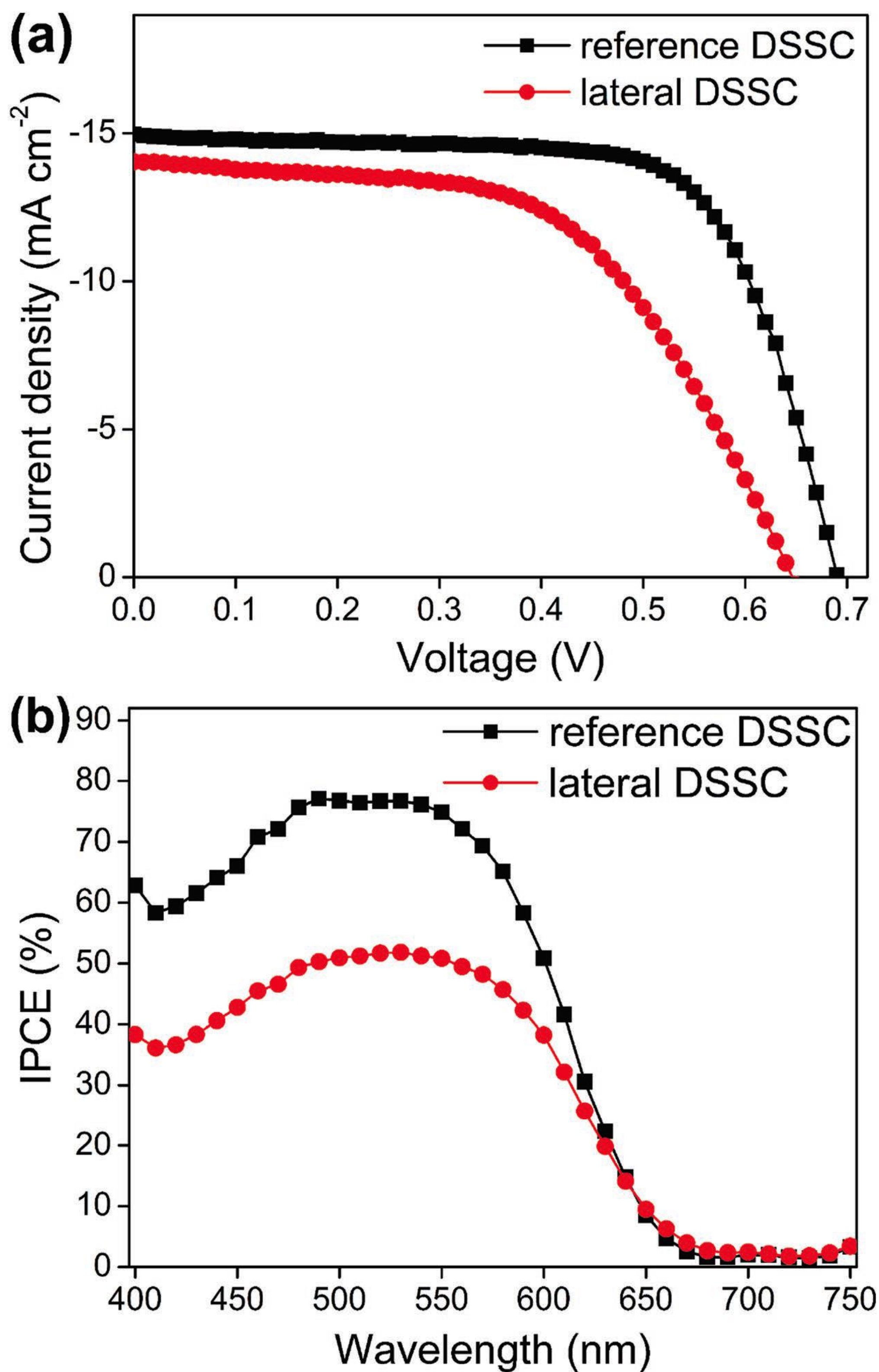

Figure 3.7. a) J–V curves and b) IPCE spectra of a conventional DSSC and a lateral DSSC with back incident light.

3.4 Conclusion

In conclusion, we created a lateral PE-CE structure of nanostructured TiO_2/FTO films with microscale interdigital fingers for DSSCs through the process of a one-step femtosecond laser patterning. The performance of this lateral DSSC, especially FF, is significantly improved in comparison with other types of laterally structured third-generation solar cells. The design of this lateral structure with microscale interdigital fingers could be directly implemented in QDSSCs, and the laser patterning could be applied to other types of solar cells, such as interdigital PE for OPVs and PSCs. For future work, we will focus on the individual electrode finger and study its surface variation by laser processing to further improve the performance of such lateral DSSCs.

3.5 References

[1] M. Grätzel, R. A. J. Janssen, D. B. Mitzi, E. H. Sargent, Nature 2012, 488, 304.

[2] S. Mathew, A. Yella, P. Gao, R. Humphry-Baker, B. F. Curchod, N. Ashari-Astani, I. Tavernelli, U. Rothlisberger, M. K. Nazeeruddin, M. Grätzel, Nat. Chem. 2014, 6, 242.

[3] H. Li, Q. Zhao, W. Wang, H. Dong, D. S. Xu, G. J. Zou, H. L. Duan, D. P. Yu, Nano Lett. 2013, 13, 1271.

[4] M. Kim, S. B. Jo, J. H. Park, K. Cho, Nano Energy 2015, 18, 97.

[5] M. Kim, J. H. Park, J. H. Kim, J. H. Sung, S. B. Jo, M.-H. Jo, K. Cho, Adv. Energy Mater. 2015, 5, 1401317.

[6] Z. Xiao, Y. Yuan, Y. Shao, Q. Wang, Q. Dong, C. Bi, P. Sharma, A. Gruverman, J. Huang, Nat. Mater. 2015, 14, 193.

[7] Q. Dong, J. Song, Y. Fang, Y. Shao, S. Ducharme, J. Huang, Adv. Mater. 2016, 28, 2816.

[8] A. Ahnood, H. Zhou, Y. Suzuki, R. Sliz, T. Fabritius, A. Nathan, G. A. J. Amaratunga, Nanoscale Res. Lett. 2015, 10, 486.

[9] H. Han, U. Bach, Y. Cheng, R. A. Caruso, C. MacRae, Appl. Phys. Lett. 2009, 94, 103102.

[10] D. Fu, X. L. Zhang, R. L. Barber, U. Bach, Adv. Mater. 2010, 22, 4270.

[11] H. Yang, D. Fu, M. Jiang, J. Duan, F. Zhang, X. Zeng, U. Bach, Thin Solid Films 2013, 531, 519.

[12] M. Shen, J. E. Carey, C. H. Crouch, M. Kandyla, H. A. Stone, E. Mazur, Nano Lett. 2008, 8, 2087.

[13] M. Farsari, B. N. Chichkov, Nat. Photonics 2009, 3, 450.

[14] U. Zywietz, A. B. Evlyukhin, C. Reinhardt, B. N. Chichkov, Nat. Commun. 2014, 5, 3402.

[15] H. liu, Y. Huang, H. Jiang, PNAS 2016, 113, 3982.

[16] X. Zhang, H. Liu, X. Huang, H. Jiang, J. Mater. Chem. C 2015, 3, 3336.

[17] X. Huang, H. Liu, X. Zhang, H. Jiang, ACS Appl. Mater. Interfaces 2015, 7, 27845.

[18] G. Mincuzzi, A. L. Palma, A. Di Carlo, T. M. Brown, ChemElectro-Chem 2016, 3, 9.

[19] X. Sheng, C. A. Bower, S. Bonafede, J. W. Wilson, B. Fisher, M. Meitl, H. Yuen, S. Wang, L. Shen, A. R. Banks, C. J. Corcoran, R. G. Nuzzo, S. Burroughs, J. A. Rogers, Nat. Mater. 2014, 13, 593.

[20] P. Kubis, N. Li, T. Stubhan, F. Machui, G. J. Matt, M. M. Voigt, C. J. Brabec, Prog. Photovolt: Res. Appl. 2015, 23, 238.

[21] I. J. Kramer, E. H. Sargent, Chem. Rev. 2014, 114, 863.

[22] W.-S. Jeong, J.-W. Lee, S. Jung, J. H. Yun, N.-G. Park, Sol. Energy Mater. Sol. Cells 2011, 95, 3419.

[23] S. K. Balasingam, M. Lee, M. G. Kang, Y. Jun, Chem. Commun. 2013, 49, 1471.

[24] X. Zhang, X. Huang, C. Li, H. Jiang, Adv. Mater. 2013, 25, 4093.

[25] D. Schmidt, M. Hager, U. Schubert, Adv. Energy Mater. 2016, 6, 1500369.

[26] S. Ito, S. M. Zakeeruddin, P. Comte, P. Liska, D. Kuang, M. Grätzel, Nat. Photonics 2008, 2, 693.

CHAPTER 4

Artificial Eye for Scotopic Vision based on Bioinspired All-Optical Photosensitivity Enhancer with Super-Resolution Image Reconstruction Technique

Part of the contents in this chapter has been published as:

H. Liu, Y. Huang, and H. Jiang, "Artificial eye for scotopic vision with bioinspired all-optical photosensitivity enhancer," ***Proceedings of the National Academy of Sciences of the United States of America (PNAS)*****, Vol. 113, No. 15, pp. 3982-3985, 2016.**

This chapter reports an all-optical strategy to significantly improve low-light imaging capability with the help of a biologically inspired photosensitivity enhancer (BPE) consisting of thousands of microphotocollectors (μ-PCs). The underlying principle is based on the optical concept of superposition eyes and elephantnose fish eye which is described in detail. The structural design as well as the unique features of the BPE are also explained. In addition to the demonstration of the hardware capability of acquiring images under low-light environment, the software approach that adopts iterative-back-projection (IBP) maximum likelihood super-resolution algorithm to obtain high-resolution images is described. The presented all-optical approach can be used on top of other electronic technologies further improving image sensors with photosensitivity reaching their physical limitations.

4.1 Introduction

Improving the photosensitivity level for low-light imaging is important for visual information acquisition and is critical to many applications in medicine, military, security, and astronomy [1–5]. Current methods for this purpose predominantly rely on electronics, including the use of external image intensifiers or on-chip multiplication gain technology, or highly photosensitive imaging sensors with emerging photoactive materials [6–9]. These electronic devices, although able to increase the overall photosensitivity of imagers by several orders of magnitude, have inevitable physical and material limitations [10]. Another direction to improve the photosensitivity of imaging systems could be seeking a breakthrough in the optics for the imaging, which is largely unexplored.

In pursuit of a groundbreaking optical approach to photosensitivity enhancement, we look to nature for inspiration. Some biological eyes have adopted exquisite, purely optical scheme for scotopic vision [11–13]. For example, superposition eyes possess much better scotopic vision than equivalent apposition eyes because light received by a single rhabdom is collected from multiple lenses or reflectors [14]. Figures 4.1(A-C) illustrate the structures and light-receiving mechanisms for an apposition eye, superposition eyes without and with misaligned optics. The apposition compound eyes, usually found in arthropod groups, consist of many individual ommatidia, each of which has a lens and a rhabdom. The light is gathered by the single lens to the rhabdom, contributing only a single point of image. In superposition eyes, nevertheless, the light received by the rhabdom is superimposed from multiple lenses (refractive superposition eyes) or mirrors (reflective superposition eyes) that are precisely aligned on a curved surface. As can be seen, superposition eyes are relatively more superior in delivering a picture in low-light environment due to the convergence of the gathered light.

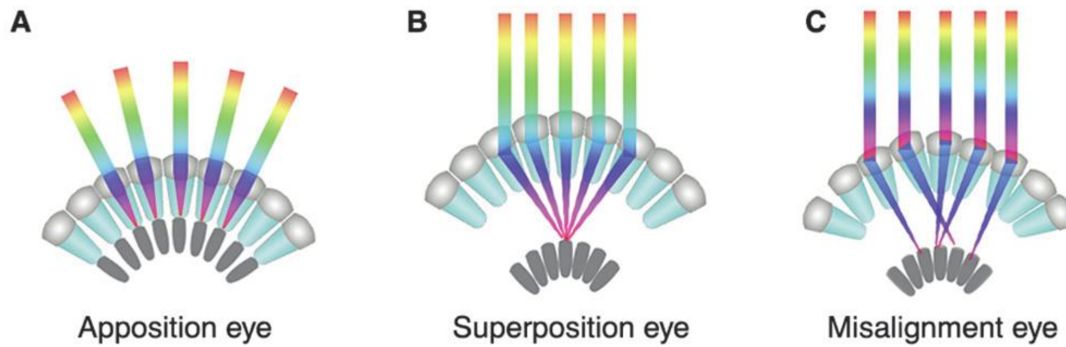

Figure 4.1. Schematic illustrations of (A) An apposition compound eye, (B) A superposition compound eye. (C) A superposition eye with misaligned optics.

However, mimicking superposition eyes in artificial devices poses tremendous technical challenges in both manufacturing and maintaining the optical performance since any misalignment of the optics might cause a failure in light collection and imaging as depicted in figure 4.1(C). In the retina of the elephantnose fish (Gnathonemus petersii), collecting light (wavelength $\lambda \sim 615$ nm) to reach the photoreceptors is achieved by crystalline micro-cups with reflecting photonic crystal sidewalls as shown in figure 4.2(A) [15]. This focusing mechanism of guiding light rays through an enclosed structure is much less prone to imperfection in optical elements, and thus provides a viable solution to realizing superposition in man-made imagers. Figures 4.2(B-C) show an artificial eye for scotopic vision employing the all-optical photosensitivity enhancer as shown in figure 4.2(D) with numerous μ-PCs.

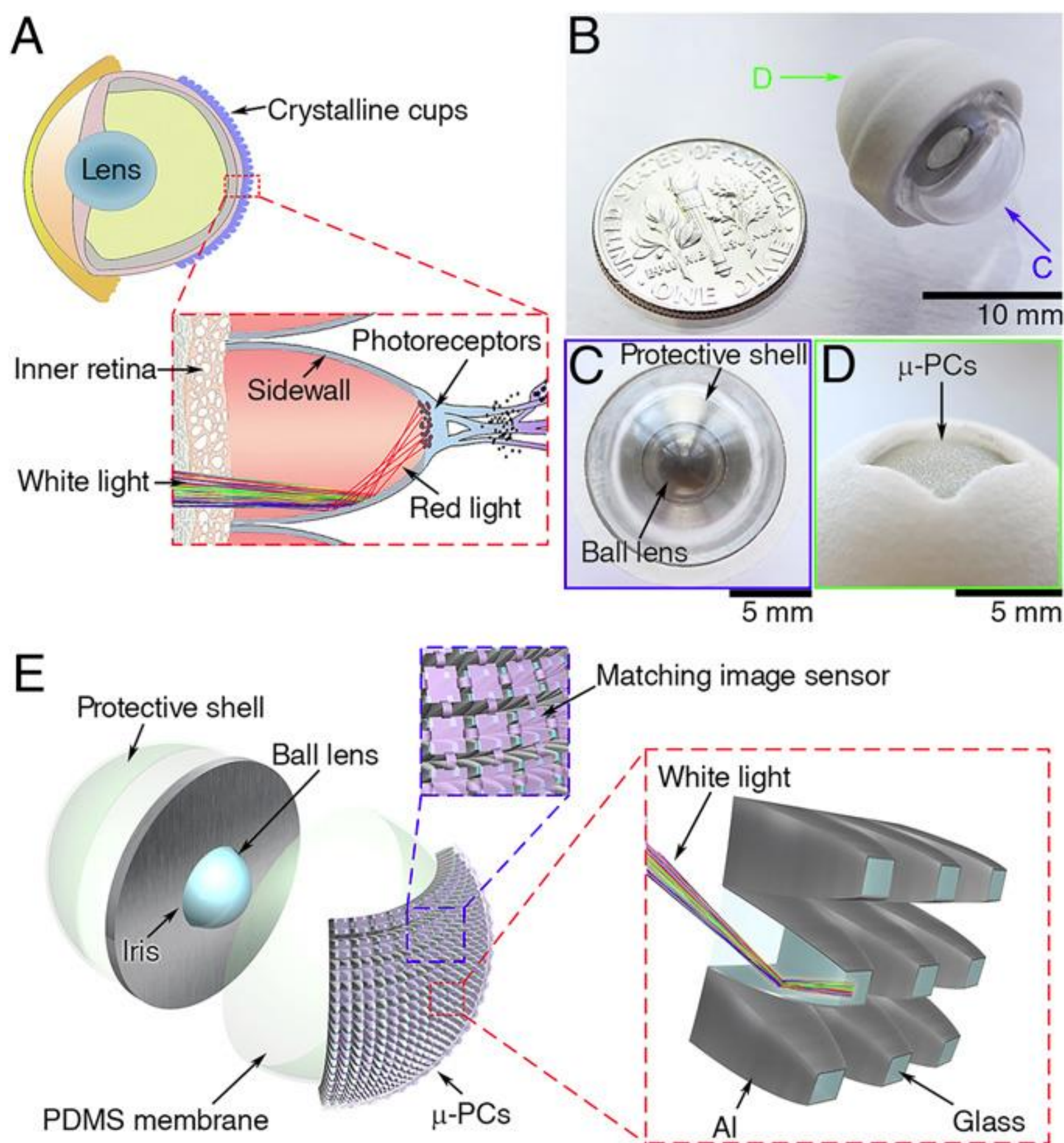

Figure 4.2. Schematic illustrations and images of a natural eye of elephantnose fish and an artificial eye. (A) Illustrations of the anatomical structure of the elephantnose fish eye and a crystalline cup in the retina (Inset). (B–D) Images of the artificial eye, its front view, and the BPE on the rear side, respectively. (E) Exploded illustration of the artificial eye. (Inset, Right) The structure of μ-PCs is shown.

In this work, an artificial eye inspired by the light-collecting mechanism mentioned above is demonstrated which is basically a bioinspired photosensitivity enhancer (BPE) accomplished by thousands of three-dimensional, omnidirectionally aligned microphotocollectors (μ-PCs) with parabolic reflective sidewalls. The miniaturized, low-cost, and zero-power-consumption device presented here can be implemented independently in imaging systems, or combined with other image enhancement technologies, which opens a previously unidentified direction toward obtaining high photosensitivity in imaging systems.

Basic structure, features and fabrication of the BPE and μ-PCs are briefly introduced and a software-based method, i.e. iterative-back-projection super-resolution reconstruction to resolve the problem of low resolution in the designed system is described. The performance of the device in image-capturing was tested manifesting the achievement of clear and high-resolution images and no discernible images could be obtained without the BPE. The image quality assessment method of structural similarity (SSIM) index is employed to quantitatively evaluate the performance of the algorithm with different initial guesses of high-resolution images.

4.2 Structures of the artificial eye, BPE and μ-PCs

Figure 4.2(E) draws the 3D layout of the artificial eye listing the components and the structure of the bioinspired μ-PCs. The artificial eye consists of a ball lens mounted in a central iris, an array of 48 × 48 μ-PCs supported by a hemispherical polydimethylsiloxane (PDMS) membrane, and a protective shell, which are packaged in a 3D-printed protective casing of matching radii as shown in figure 4.2(B).

Figure 4.3 depicts the structure and the relevant dimensions of the designed artificial eye and the μ-PC in more detail. The ball lens generates a hemispherical image plane on the PDMS membrane, analogous to a natural eye. The close-packed μ-PCs are omnidirectionally arranged on

the PDMS membrane, with orientations directed toward the geometric center of the ball lens, anatomically equivalent to the crystalline microcups in the eyes of the elephantnose fish. Each μ-PC is a glass microstructure with two opposite facets enclosed by four parabolic sidewalls coated with reflecting aluminum as shown in the inset of figure 4.2(E). The incoming light from the large facet (input port) is collected to the small facet (output port) by the parabolic sidewalls, consequently increasing the light intensity. In this manner, μ-PCs function as superposition of incoming light to pixels on the imager. The resultant image can then be acquired by a matching image sensor [16–18].

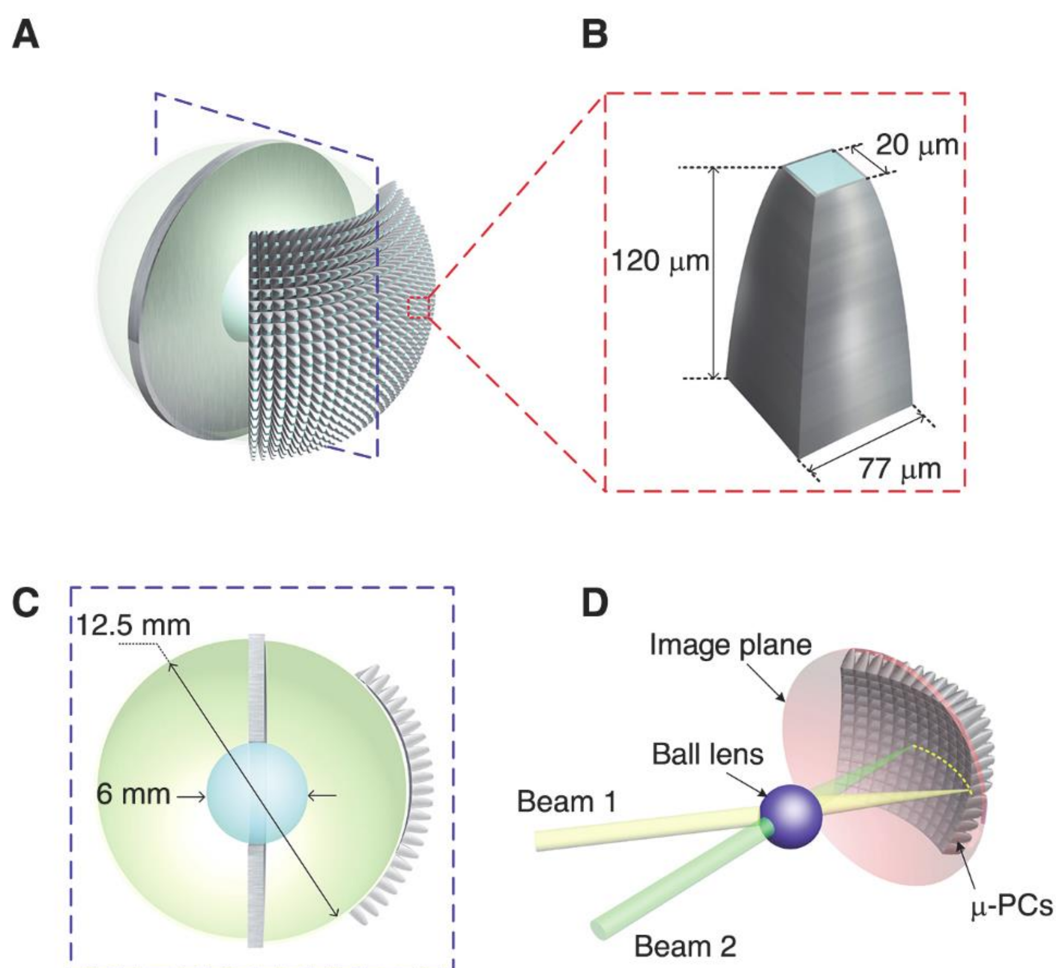

Figure 4.3. Schematic of the design of the artificial eye. (A and B) 3D layout of the artificial eye

and a μ-PC, respectively. (C) Cross-section view of the artificial eye. (D) Illustration of the image acquisition system. The ball lens generates an image plane on a hemispherical surface which is coincident with input ports of the μ-PCs. The image from the output ports is captured by a matching imager.

The structure of BPE with the array of μ-PCs is formed by femtosecond laser micromachining with layer-by-layer strategy and then is transferred onto a hemispherical PDMS membrane. The details of the fabrication process are elaborated in Reference [19].

Figure 4.4 shows the SEM image of a part of fabricated BPE indicating high-quality micromachining due to the uniform topography of the device and smooth curved sidewalls of the individual μ-PCs thanks to the precise 3D processing capability of our fabrication process.

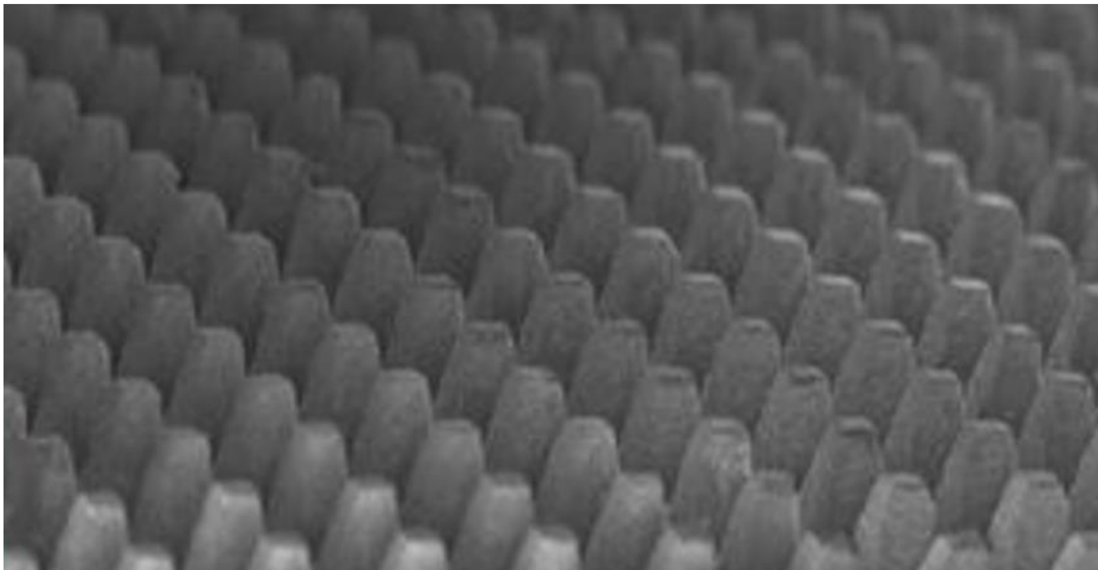

Figure 4.4. Surface SEM image of a part of fabricated BPE indicating high-quality micromachining by fs laser ablation

4.3 Device Performance

4.3.1 Visible Spectral Response

Although the emphasis of the device performance is given to the imaging capability under low-light condition, the multiplication of the light intensity (M) with respect to different wavelengths especially the visible spectrum should be evaluated first as the obtained image color might deviate from the original substantially if the responsivity at different visible wavelengths varies too much. In every 14 × 14-pixel area (corresponding to a μ-PC which covers a 77 μm × 77 μm area), maximum gray-scale values, $G_{without}$ (without μ-PC) and G_{with} (with μ-PC), were selected to calculate the multiplication of the light intensity M:

$$M = \frac{G_{with} - G_{without}}{G_{without}} \tag{4.1}$$

Figure 4.5 plots the relationship between the multiplication of the light intensity for the wavelength range of 380 to 900nm that covers the entire visible light spectrum. Blue dots in the figure denote the numerous measurements and the plot was obtained by cubic polynomial curve-fitting. As shown in the plot, the M value across the visible light spectrum has a value of approximately 3 and has a reasonable uniformity.

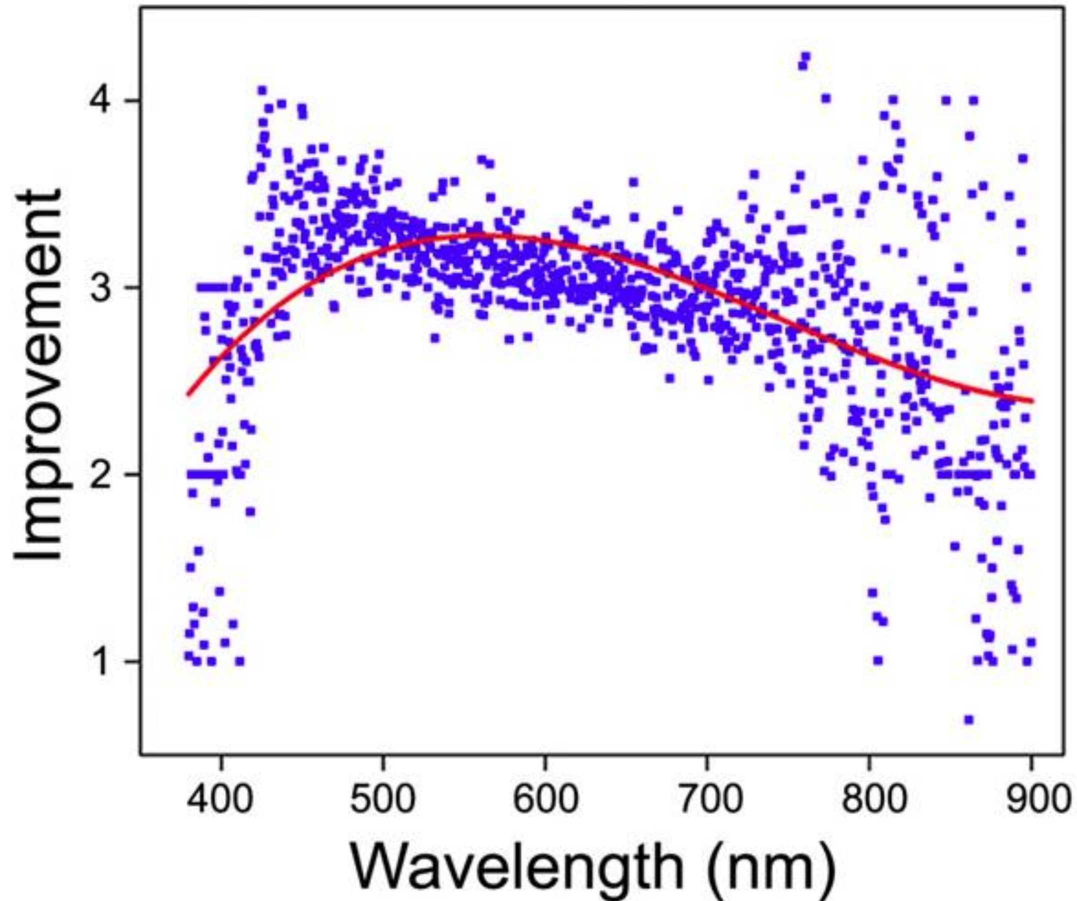

Figure 4.5. Multiplication of light intensity M (blue dots) at wavelengths ranging from 380 to 900 nm. The red line is obtained by a cubic polynomial fit.

4.3.2 Imaging Results

In order to test the imaging performance of the designed BPE, a famous figure at University of Wisconsin-Madison called Bucky badger is used as a target with the original and undistorted image shown in Figure 4.6. The original image was obtained by a camera under reasonably good illumination and then compressed to the resolution of 384 X 384 in JPEG format.

Figure 4.6. The image of the original distortion-free image of Bucky badger

Initially our BPE, array of 48x48 μ-PCs, is applied to upper-left, upper-right, bottom-left and bottom-right sections of Bucky separately under low-light condition in which the areas of the 4 sections are equal. Since each μ-PC corresponds to one pixel in resultant images, each obtained image has the resolution of 48x48. A CCD sensor is placed after the BPE that saves the image. The 4 raw images obtained directly from the CCD with BPE applied are shown in figure 4.7. It is observed that each bright dot in the images is obtained by a μ-PC while the black gap between bright dots originates from the "blind" regions between the boundary of outputs of all μ-PCs. The experiment was performed under the same ambient condition without the BPE applied, however, no light was detected by the CCD resulting in a completely dark image that indicates the much improved photosensitivity of the designed BPE structure.

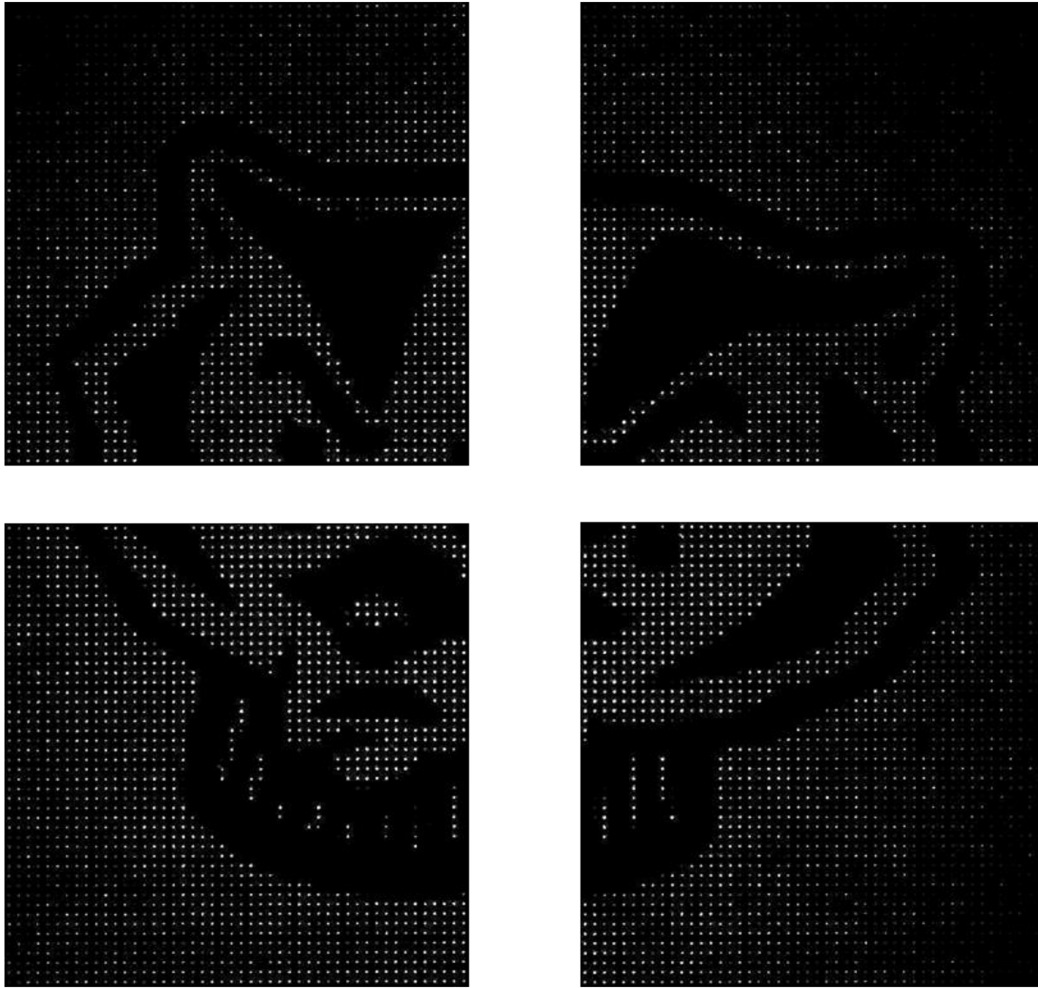

Figure 4.7. Four raw images obtained by CCD sensor with the BPE applied to the upper-left, upper-right, bottom-left and bottom-right parts of Bucky, respectively.

After the 4 raw images are obtained, they are stitched together to form a complete image for Bucky badger as shown as the left image in figure 4.8. The stitched image shows a seamless joining process for the 4 raw images. Since the bright dots along with part of their adjacent black regions represent individual pixels generated from the μ-PCs, it is necessary to convert them into single pixels so that all pixels in the final constructed image contain meaningful visual information. The dimension of the inputs of the μ-PC is approximately equivalent to the width of 14 pixels in the CCD sensor utilized in our experiment, therefore each 14x14 pixels block in the left image of figure 4.8 is converted into single pixel chosen from the pixel with the highest grayscale value

within the pixels block, and the resultant image with the resolution of 96x96 is provided as the middle image in figure 4.8. As can be seen, the physical size of the middle image is much smaller than the left one due to the pixel block compression process. To emphasize the quality of the processed image compared with the left image, the middle image is zoomed in to match the size of the left one shown as the right image in figure 4.8. It therefore can be concluded from the figure and also from the resolution of the processed image (96x96) that its quality is not satisfactory in the modern imaging applications demanding for high-definition digital contents. One solution is to fabricate BPE with smaller μ-PC, however, the fs laser has a low limit on the dimension of the features it can achieve especially for layer-by-layer ablation process. In addition, the higher number of μ-PCs requires much longer processing time with the fs laser micromachining. This difficulty of hardware improvement can be overcome by the software approach introduced in the next subsection.

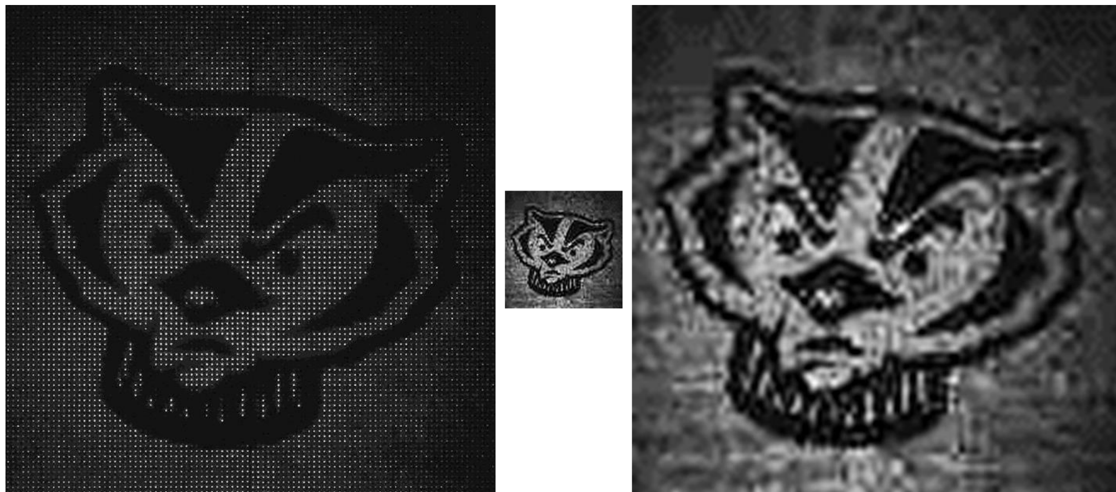

Figure 4.8. (left) Combined image from the 4 raw images;

(middle) Processed image by taking the maximum gray value in every block of 14x14 pixels of the left image as a single pixel, and then stitching them together;

(right) simply zoomed-in middle image.

4.3.3 Iterative-Back-Projection (IBP) Super-Resolution for High-Resolution Image Reconstruction

The enhancement of the photosensitivity of the μ-PCs and thus the BPE comes with the cost of an inherent problem associated with the structure of the photo-collector, that is, low resolution of the resultant images. The originally gathered light enters the μ-PC through the input port and exits through the output port. While the smaller design of the output port increases the average light intensity, it inevitably confines the received light to a smaller region hence it causes lower resolution which is hard to overcome due to the hardware limitation with this specific design and increasing processing time for greater number of smaller μ-PCs.

Instead of an expensive overhaul on the hardware modification, we resort to the software approach by adopting the iterative-back-projection (IBP) maximum likelihood super-resolution (SR) technique for a high-resolution image reconstruction from a set of low-resolution images. It is a process of combining multiple low-resolution (LR) images obtained by an imaging system and, after some computation, generating a high-resolution (HR) image. The basic prerequisites are: 1). availability of LR images captured from the same scene; 2). sub-pixel shifts between the LR images. The information difference between the LR images shifted by sub-pixel distance is the key for reconstructing an HR image beyond the resolution of the physical imaging system. Figure 4.9 illustrates the observation model for the back-projection process with a transformation kernel involving three essential steps, namely warping, blurring and down sampling, to transform an initial guess of HR image to the obtained LR images [20]. In our application, warping process only incorporates the global translation matrix, blurring is assumed to be the Gaussian distribution related to all immediately adjacent pixels and it is uniform across all pixels of the HR image, and the down sampling extent is determined by the resolution ratio of HR and LR images. In addition,

noise is considered to be zero for the simplicity. This observation model can be described as the Equation (4.2) in which the kernel is represented by a transformation matrix.

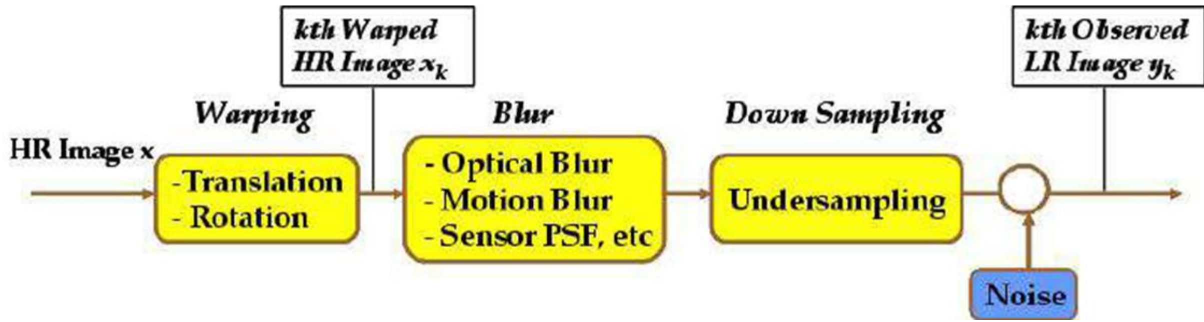

Figure 4.9. Observation model of the super-resolution image reconstruction [20]

$$\boldsymbol{Y}_k = D_k H_k F_k \boldsymbol{X} \tag{4.2}$$

where k = 1, 2, …, K, K is the number of LR images; F_k is the warping matrix for k_{th} frame; H_k models the blurring effects for k_{th} frame; D_k is the down-sampling operator for k_{th} frame; $\boldsymbol{Y}_k$ is the k_{th} frame of LR images; $\boldsymbol{X}$ is the HR image to be constructed.

In our application, the down sampling matrix and the blurring matrix are the same for all LR images while warping matrix varies for different LR images depending on their horizontal and vertical translation values.

The underlying IBP algorithm is operated as follows [21]: 1. firstly an HR image is guessed to be used in Equation (4.2); 2. after the set of LR images are computed by Equation (4.2), they are compared with the real LR images to obtain the mean squared error; 3. update the HR image with a value proportional to the difference between real LR images and computed LR images; 4. terminate the process if the number of iterations exceeds a preset maximum value allowed; 5. terminate the process if the mean squared error is less than a specified error that can be tolerated

for the final result; 6. if neither step 4 nor step 5 is met, compute LR images based on the updated HR image and then repeat steps 2-6. This iterative process is illustrated as a flow chart in figure 4.10.

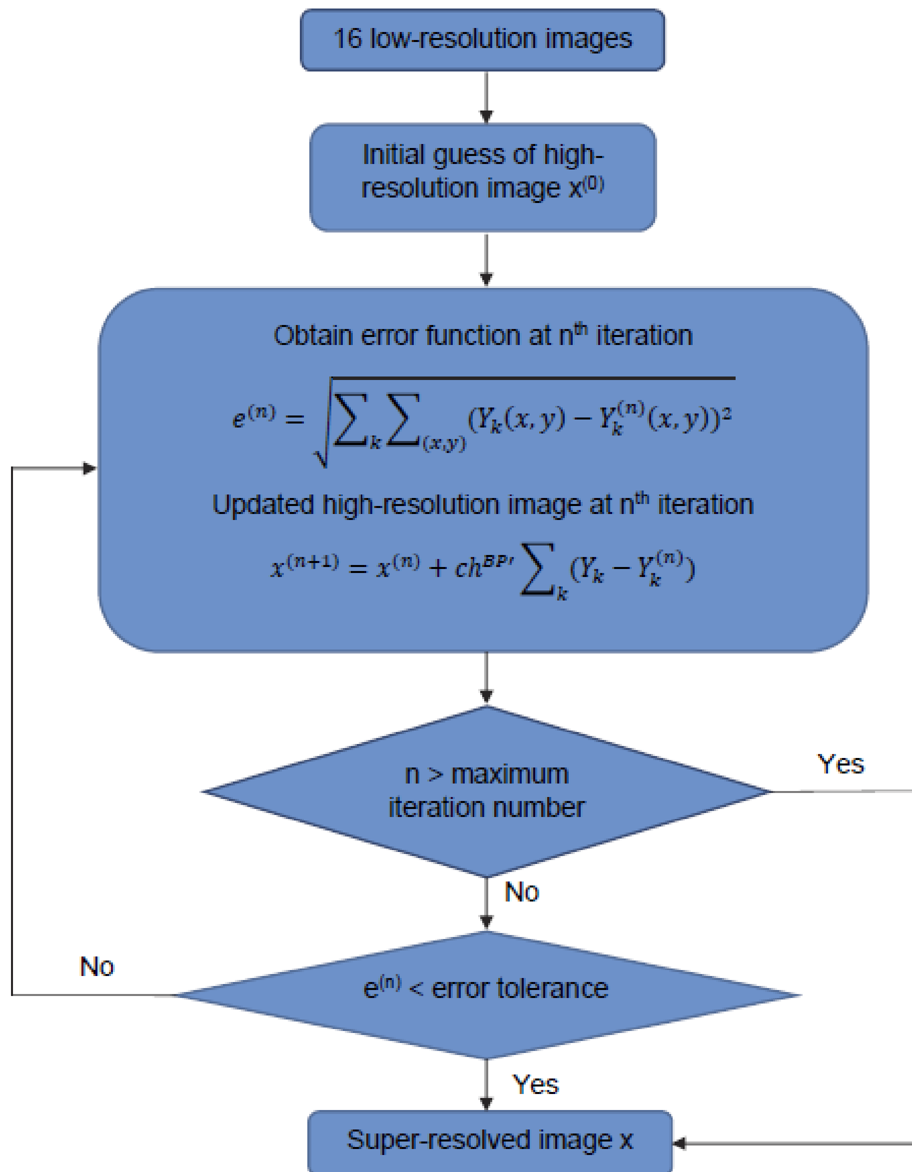

Figure 4.10. Flow chart of the iterative super-resolution reconstruction algorithm used.

In our experiments, 16 LR images were obtained when shifting the BPE-coupled CCD both horizontally and vertically with the increment of 18 μm. Because the displacement between these low-resolution images is smaller than the pixel size of BPE (77 μm), the 16 images contain different sub-pixel information. Figure 4.11 schematically illustrates the main steps to acquire high-resolution images with the BPE. The power intensity of the laser source was 0.05 μW/cm2, and transparent mask of Bucky badger head logo is used as the object. A single double-convex lens is used to generate real images on the BPE-coupled CCD which is mounted on a computer-controlled x-y translational stage.

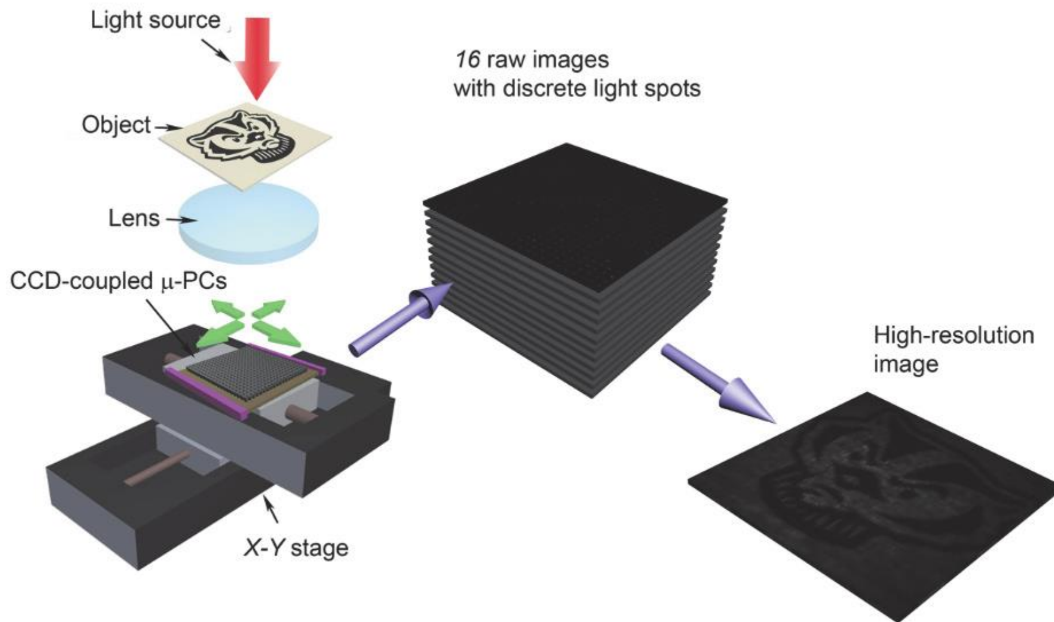

Figure 4.11. Schematic illustration of the image acquisition process.

Since the increment of displacement is 18 μm and the pixel size of BPE is 77 μm, the increment is approximated to be 2/7 pixel used in the global translation matrix in the IBP super-resolution algorithm. All the 16 LR images obtained and their corresponding horizontal and vertical displacements are shown in figures 4.12(a) and (b), respectively.

(a)

$(0,\ 0)$	$(\frac{2}{7}, 0)$	$(\frac{4}{7}, 0)$	$(\frac{6}{7}, 0)$
$(0, \frac{2}{7})$	$(\frac{2}{7}, \frac{2}{7})$	$(\frac{4}{7}, \frac{2}{7})$	$(\frac{6}{7}, \frac{2}{7})$
$(0, \frac{4}{7})$	$(\frac{2}{7}, \frac{4}{7})$	$(\frac{4}{7}, \frac{4}{7})$	$(\frac{6}{7}, \frac{4}{7})$
$(0, \frac{6}{7})$	$(\frac{2}{7}, \frac{6}{7})$	$(\frac{4}{7}, \frac{6}{7})$	$(\frac{6}{7}, \frac{6}{7})$

(b)

Figure 4.12. (a) 16 LR images, resolution: 96 x 96; (b) Sub-pixel displacement (x, y) for each LR image (unit: pixel)

An initial guess for the high-resolution image $x^{(0)}$ must be provided that matches the desirable resolution. In our implementation, the effect of different initial guesses for HR image (resolution: 384 x 384) on the quality of the final result is studied. In total, the following three guesses of HR image are used: A. completely dark HR image; B. expanded first LR image matching the HR image in which each pixel in the first LR image is expanded to a 4x4 pixels block with the same values as the original pixel; C. the average of all 16 LR images that are expanded the same way as that described in B. Since 16 (4-by-4) low-resolution images with identical increment of horizontal or vertical sub-pixel displacement are to be super-resolved, the initially guessed high-resolution image and the updated high-resolution images on-the-fly are under-sampled (i.e. decimated) every four pixels horizontally or vertically. The warping matrix M_k which is in fact a purely global translational matrix in our application, is obtained via a linear kernel relating the next pixel horizontally or vertically depending on the displacement orientation. The kernel primarily consisted of a sparse Toeplitz matrix that can apply the same kernel function to related pixels for all pixels in the images. A regularization term of Laplacian operator as the prior knowledge is used to maintain a low value of steep changes among adjacent pixels to ensure smoothness of the processed HR image.

Figures 4.13(a)-(c) show the HR images with the resolution of 384 x 384 with the initial guesses of blank HR image, expanded first LR image, average of the 16 expanded LR images. As can be clearly seen, the processed HR images in figures 4.13(b)-(c) possess much higher quality than figure 4.13(a) with the initial guess of blank HR image although the mean squared errors between the real LR images and the computed LR images based on all processed HR images fall below the specified tolerable value. In fact, the choice of the back-projection kernel including the regularization term as well as the initial guesses can affect the quality of the final HR image

reconstructed. There are several possible solutions with local minima of mean squared errors, and there exists optimal solution with global minimum value for the mean squared error. The choice of initial guess does not influence the performance of the algorithm in terms of speed or stability. Nevertheless, the factor of initial guesses can affect which of the possible solutions is reached first and usually a good choice is the average of the expanded LR images obtained [21].

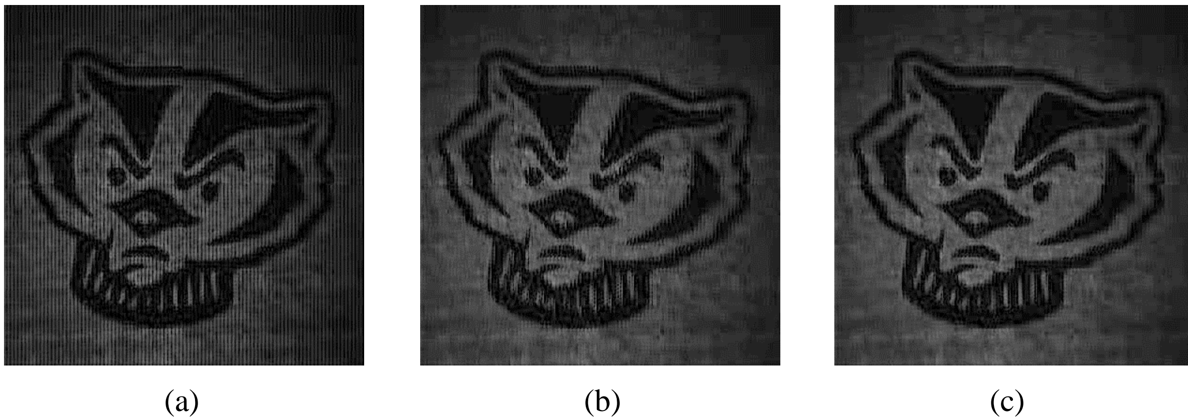

(a) (b) (c)

Figure 4.13. HR images with resolution of 384 x 384 obtained from the IBP super-resolution algorithm based on the initial guesses of (a). blank image; (b). expanded first LR image; (c). average of the 16 expanded LR images.

4.3.4 Image Quality Assessment Based on the Method of Structural Similarity (SSIM) Index

The method of SSIM index was proposed by Z. Wang et al [22] as an alternative full-reference image quality assessment method to the traditional ones such as mean squared error (MSE) and peak signal-to-noise ratio (PSNR). The difference between SSIM index and other traditional methods lies in the fact that SSIM index is designed to be adapted to the perceived visual quality by human eyes.

The SSIM model incorporates three factors that are related to the perception of human

eyes: luminance l(x, y), contrast c(x, y) and structure s(x, y), where x, y are two images or portion of two images to be compared with the following formula:

$$l(x,y) = \frac{2\mu_x\mu_y + c_1}{\mu_x^2 + \mu_y^2 + c_1}$$
$$c(x,y) = \frac{2\sigma_x\sigma_y + c_2}{\sigma_x^2 + \sigma_y^2 + c_2}$$
$$s(x,y) = \frac{\sigma_{xy} + c_3}{\sigma_x\sigma_y + c_3} \quad (4.3)$$

$$SSIM(x,y) = \left[l(x,y)^\alpha \cdot c(x,y)^\beta \cdot s(x,y)^\gamma\right] \quad (4.4)$$

where μ_x is the average of x, μ_y is the average of y, σ_x^2 is the variance of x, σ_y^2 is the variance of y, σ_{xy} is the covariance of x and y. The constants $c_1 = (k_1L)^2$, $c_2 = (k_2L)^2$ are used to stabilize the division with weak denominator in which L is the dynamic range of the pixel-values for the images under investigation. The black and white images in our application have the depth of 8 bits, therefore in our application, L of 255 was chosen. The coefficients $k_1 = 0.01$, $k_2 = 0.03$ and $c_3 = c_2/2$. The exponents α, β and γ are the weights for luminance, contrast and structure terms, respectively.

Local SSIM value for each pixel in x using y as the reference is obtained by the algorithm resulting in an SSIM index map. Although the parameters of luminance and contrast are indispensable for visual perception, they are not considered in our application since our emphasis is given to image feature details of Bucky badger and the reference image was obtained under much more illumination. On the other hand, structure term $s(x, y)^\gamma$ indicates the structural difference between the two images. Therefore, α, β and γ are set to be 0, 0 and 1 respectively in our calculations. According to the definition of s(x, y) in Eqn. (4.3), SSIM index has a maximum value of 1 which occurs if and only if x and y have exactly the same structural details in our

application for which x is the HR images processed by super-resolution algorithm shown in figure 4.13 and y is the reference image shown in figure 4.6. In addition, the average of SSIM values for all pixels among the HR image and reference image reaches maximum value of 1 if and only if HR and reference images are structurally identical. The closer the average SSIM value for the HR image is to 1, the more similar it is to the original distortion-free image.

Figure 4.14(a)-(c) illustrates the index maps for the HR image with initial guess of blank image, HR image with initial guess of expanded first LR image and HR image with initial guess of average of the 16 expanded LR images using the original undistorted image as the reference, respectively. It is apparent that HR image with the guess of average of expanded LR images possesses the highest quality with the SSIM value of 0.8606 while the one with the guess of blank image shows the lowest quality with the SSIM value of mere 0.7690 that further testifies that initially averaging the expanded LR images presents a better quality for the processed HR image using IBP super-resolution technique.

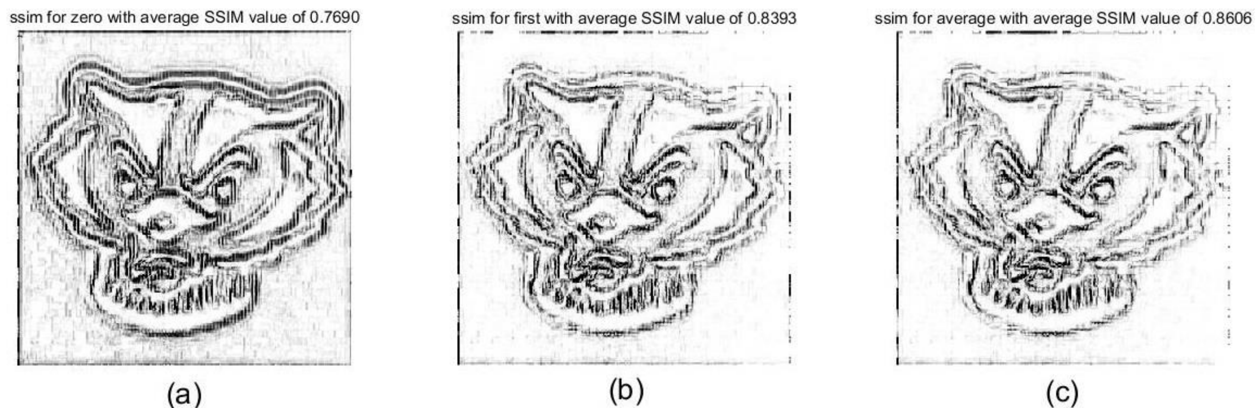

Figure 4.14. SSIM index maps and their average SSIM values using the original distortion-free image as the reference for the HR images obtained by IBP super-resolution algorithm with the initial guesses of (a). completely blank image; (b). expanded first LR image; (c). average of the 16 expanded LR images.

4.4 Conclusion

A bioinspired all-optical approach to achieve scotopic vision is proposed and implemented by fs laser micromachining technique in this work. The manufactured bioinspired photosensitivity enhancer (BPE) possesses excellent performance under extremely low-light conditions and the uniform spectral response across the entire visible spectrum. In order to achieve higher resolution of the images obtained directly from the BPE, a software approach called iterative-back-projection (IBP) super-resolution image reconstruction algorithm is employed to drastically increase the resolution of the obtained images with robust performance that overcomes the difficulty of the hardware limitation. The image quality assessment method called structural similarity (SSIM) index is used to quantitatively gauge the quality of the processed HR image by super-resolution algorithm and it was found the initial guess of average of all expanded LR images yielded the best result that is closest to the original image without any distortion.

The bioinspired low-light image-enhancing strategy presented here leads to a conceptually advantageous, all-optical route to improve scotopic imaging. Our artificial eye has the potential in powerful compact night-vision camera with low-distortion characteristics. Its working spectrum could potentially be expanded to X-ray and far infrared for a host of applications such as endoscopes, robots, and space exploration. In addition, the manufacturing process demonstrated in this work is applicable to other flexible microsystems and bioinspired devices. Finally, the software approach to increase the image resolution provides an economical way to overcome the physical limitations.

4.5 References

1. Lee T-W (2009) Military Technologies of the World (Greenwood, Westport, CT).

2. Weissleder R, Tung C-H, Mahmood U, Bogdanov A, Jr (1999) In vivo imaging of tumors with protease-activated near-infrared fluorescent probes. Nat Biotechnol 17(4): 375–378.

3. Hofmann M, Eggeling C, Jakobs S, Hell SW (2005) Breaking the diffraction barrier in fluorescence microscopy at low light intensities by using reversibly photoswitchable proteins. Proc Natl Acad Sci USA 102(49):17565–17569.

4. Morris PA, Aspden RS, Bell JEC, Boyd RW, Padgett MJ (2015) Imaging with a small number of photons. Nat Commun 6(5913):5913.

5. Boyce PB (1977) Low light level detectors for astronomy. Science 198(4313): 145–148.

6. Dickson JF (1976) On-chip high-voltage generation in MNOS integrated circuits using an improved voltage multiplier technique. IEEE J Solid-State Circuits 11(3):374–378.

7. Wang XF, Uchida T, Coleman DM, Minami SA (1991) Two-dimensional fluorescence lifetime imaging system using a gated image intensifier. Appl Spectrosc 45(3):360–366.

8. Lopez-Sanchez O, Lembke D, Kayci M, Radenovic A, Kis A (2013) Ultrasensitive photodetectors based on monolayer MoS2. Nat Nanotechnol 8(7):497–501.

9. Liu C-H, Chang Y-C, Norris TB, Zhong Z (2014) Graphene photodetectors with ultrabroadband and high responsivity at room temperature. Nat Nanotechnol 9(4): 273–278.

10. Vashchenko VA, Sinkevitch VF (2008) Physical Limitations of Semiconductor Devices (Springer Science+Business Media, New York).

11. Land MF, Nilsson D-E (2012) Animal Eyes (Oxford Univ Press, New York).

12. Lee LP, Szema R (2005) Inspirations from biological optics for advanced photonic

systems. Science 310(5751):1148–1150.

13. Warrant EJ (1999) Seeing better at night: Life style, eye design and the optimum strategy of spatial and temporal summation. Vision Res 39(9):1611–1630.

14. Agi E, et al. (2014) The evolution and development of neural superposition. J Neurogenet 28(3-4):216–232.

15. Kreysing M, et al. (2012) Photonic crystal light collectors in fish retina improve vision in turbid water. Science 336(6089):1700–1703.

16. Floreano D, et al. (2013) Miniature curved artificial compound eyes. Proc Natl Acad Sci USA 110(23):9267–9272.

17. Ko HC, et al. (2008) A hemispherical electronic eye camera based on compressible silicon optoelectronics. Nature 454(7205):748–753.

18. Jung I, et al. (2011) Dynamically tunable hemispherical electronic eye camera system with adjustable zoom capability. Proc Natl Acad Sci USA 108(5):1788–1793.

19. H. Liu, Y. Huang and H. Jiang, "Artificial eye for scotopic vision with bioinspired all-optical photosensitivity enhancer," Proceedings of the National Academy of Sciences of the United States of America (PNAS), vol. 113, no. 15, pp. 3982-3985.

20. S. Gong, master's thesis, West Virginia University, 2007.

21. M. Irani, and S. Peleg, "Improving resolution by image registration", CVGIP: Graphical Models and Image Processing, Volume 53, Issue 3, May 1991, Pages 231-239.

22. Z. Wang, A. C. Bovik, H. R. Sheikh, and E. P. Simoncelli, "Image quality assessment: from error visibility to structural similarity", IEEE Transactions on Image Processing, Volume 13, Issue 4, pp. 600-612, April 2004.

CHAPTER 5

Conclusion and Future Work

5.1 Conclusion

Femtosecond (fs) pulsed laser exhibits superior characteristics in micromachining various materials and provides a promising alternative to conventional manufacturing techniques. The research work described in the preceding chapters demonstrates the versatility of fs laser micromachining technique for manufacturing different microstructures in three types of materials which have great potential in microfluidics used in harsh environment, compact photovoltaics and scotopic imaging science, respectively. The designed structures in these specific material systems cannot be readily accomplished by conventional micromachining techniques or longer pulsed lasers such as nanosecond (ns) laser ablation.

A through-wafer all-SiC fluidic microstructure fabricated by deionized (DI) water-assisted fs laser micromachining is demonstrated initially. Due to the unusual properties such as high melting point and chemical inertness, it is extremely difficult to etch bulk silicon carbide (SiC) substrates quickly using normal chemicals or by reactive ion processing. With the fs laser ablation, nonetheless, SiC material in the laser-affected zone (LAZ) can be removed with ease thanks to the high peak energy and multi-photon absorption mechanism of the fs pulsed laser. A Z-shaped microfluidic channels were realized by layer-by-layer ablation strategy with minimal collateral thermal damage and precise control was achieved. The chosen fluid chosen, i.e. mineral oil, was

found to have a higher wettability with periodic nanostructures induced by laser micromachining process which was conducive to fluidic flow inside the microchannels. Furthermore, microchannels with various cross-sectional shapes were manufactured successfully which is not possible to fabricate using conventional photo-lithography approach.

Then a type of dye-sensitized solar cells (DSSCs) with lateral structure of photoelectrode (PE) and counter electrode (CE) is elaborated. Compared with the lateral DSSCs reported previously in the literature, the designed lateral DSSC with interdigital patterns achieves much higher rate of lateral charge carrier transport causing lower recombination loss that in turn improves the device performance. In addition, the effect of laser pulse energy on ablation morphology and device performance was also investigated. The fill factor (FF) is more than double and the photon-to-electron conversion efficiency (η) is improved tremendously over those lateral devices previously reported. Moreover, the design of such lateral structure makes the DSSCs fabricated much more compact than conventional structures leading to the possibility of integrating other modules such as energy storage unit into the device while maintaining the overall compactness and relative portability.

Finally, an artificial eye for scotopic vision consisting of an array of all-optical parabolic microstructures formed by fs laser micromachining inspired by the unique feature of superposition compound eyes and retinal structure of elephantnose fish is proposed and fabricated. The essential part is a biologically inspired photosensitivity enhancer (BPE) made of thousands of so-called microphotocollectors (μ-PCs) that drastically improves the photosensitivity making it a suitable device under low-light condition. It possesses reasonably uniform responsivity across the entire visible spectrum which is desirable for imaging application. Due to the device limitations, the obtained images have low-resolution jeopardizing the prospect of the artificial eye. Nevertheless,

a software-based image restoration strategy called iterative-back-projection (IBP) super-resolution image reconstruction algorithm was adopted to greatly increase resolution of the obtained images. The high-resolution (HR) images were evaluated quantitatively by the image assessment method of structural similarity (SSIM) index implying that the reconstructed HR image with the initial guess of average of expanded low-resolution (LR) images generates the closest approximation to the original HR image without distortion.

5.2 Future Work

As for the SiC microfluidics research, more complex 3D structures such as curved microchannels with varying channel width and periodic microstructures on the sidewalls can be fabricated in SiC by the fs laser micromachining to achieve vortex and mixing in the channels with micrometer scale. Moreover, micromachining inside bulk SiC substrates without affecting the surface can alter the refractive index for specific regions inside the material that might be a viable way to fabricate optical waveguides ready to be used in harsh environment. In addition, it is imperative to get rid of PDMS cladding layers and manufacture all-SiC microfluidics that can be practically used in harsh environment.

In the design of lateral DSSCs presented in this work, the fill factor (FF) and the efficiency (η) have been improved dramatically over the previous lateral solar cells. However, the area of counter electrode (CE) prevents the device to reach maximum possible η due to the photon loss on CE regions. Future study can be directed toward the decrease of CE width, for example by further reducing the pulsed laser spot. In addition, more in-depth investigation of influence of the laser parameters on the interface of PE and CE fingers is necessary to further improve the device performance.

The super-resolution technique described in this work has generated images with higher resolution, however, the chosen back-projection kernel can still slightly affect the quality of reconstructed high-resolution image. Hence, it is suggested to gain as much prior knowledge as possible from the image acquisition process so that an optimal back-projection kernel as well as regularization constraints can be implemented representing the closest approximation to the parameters introduced in the experiments, since the processed high-resolution images obtained from an image reconstruction observation model incorporating more precise parameters are expected to be more similar to the original distortion-free image.

Appendix A

The following is the Matlab code for the main program that calls the IBP super-resolution Matlab function in Appendix B and reconstructs the high-resolution images shown in figure 4.13.

```
%%%%%%%%%%%%%%%%%%%%%%%%%%%%%%%%%%%%%%%%%%%%%%%%%%%%%%%%%%%%%%%%%%%%%%%%%%%
%   This program is the main program that reconstructs and saves the
%   high-resolution image from a set of 16 low-resolution images for Bucky
%   badger, the mascot of the University of Wisconsin-Madison. The HR image
%   reconstruction is accomplished by iterative-back-projection (IBP)
%   super-resolution algorithm implemented in IBPSuperresolution.m
%   repeatedly called by this main program.
%%%%%%%%%%%%%%%%%%%%%%%%%%%%%%%%%%%%%%%%%%%%%%%%%%%%%%%%%%%%%%%%%%%%%%%%%%%

%% clear all contents and Command Window display
clear
clc

%% Initialize relevant parameters

% total number of LR images
numLRimages = 16;

% super-resolution resolution enhancement factor along either horizontal or
% vertical direction
superResolveFactor = sqrt(numLRimages);

% the sigma value for gaussian spatial filter applied in the HR image
blurDeviation = 1;

% a cell array to store all LR images
LRimages = cell(numLRimages, 1);

% a cell array with LR file paths along with their image names
imageNames = cell(numLRimages, 1);

% global translations along X and Y for all LR images
displacements = zeros(numLRimages, 2);

% the displacement increment between adjacent LR images since the images
% used in this experiment are evenly displaced
increment = 2.0 / 7.0;

% store the image path/name and assign the values of displacements for all
% LR images
p = 1;
for i = 1:superResolveFactor
```

```
    for j = 1:superResolveFactor
        imageNames{p} = strcat('/bucky/', num2str(i), num2str(j), '.jpg');
        displacements(p, 1) = (j - 1) * increment;
        displacements(p, 2) = (i - 1) * increment;
        p = p + 1;
    end
end

% get all LR images
for i = 1:numLRimages
    curImage = rgb2gray(imread(imageNames{i}));
    LRimages{i} = im2double(curImage);
end

% size of all LR images
LRSize = size(LRimages{1});

% size of HR image to be reconstructed
HRSize = superResolveFactor * LRSize;

% all the expanded images obtained from cloning every pixel and expanding
% it to a superResolveFactor-by-superResolveFactor block for all LR images
expandedImages = cell(numLRimages, 1);

for i = 1:numLRimages

    expandedImages{i, 1} = imresize(LRimages{i}, superResolveFactor,
'nearest');
end

% initial guess of HR image in which all pixels have grayscale values of 0
zeroGuessForHR = zeros(HRSize);

% initial guess of HR image which is the expanded first LR image
firstImageGuessForHR = expandedImages{1, 1};

% initial guess of HR
aveImagesGuessForHR = zeros(HRSize);
for i = 1:numLRimages
    aveImagesGuessForHR = aveImagesGuessForHR + expandedImages{i, 1};
end
aveImagesGuessForHR = aveImagesGuessForHR / numLRimages;


%% Compute the Super-Resolution images based on different guesses

% obtain the HR image with the initial guess of all pixels with zero values
HRimage_zeroGuess = IBPSuperresolution(LRimages, displacements,
blurDeviation, zeroGuessForHR);

% obtain the HR image with the initial guess of first LR image expanded to
% match the size of HR image
HRimage_firstImageGuess = IBPSuperresolution(LRimages, displacements,
blurDeviation, firstImageGuessForHR);
```

```
% obtain the HR image with the initial guess of expanded average of all LR
% images
HRimage_aveImageGuess = IBPSuperresolution(LRimages, displacements,
blurDeviation, aveImagesGuessForHR);

%% get the final HR image and other images

% obtain the images of high resolution and initial guesses
imwrite(zeroGuessForHR, 'C:\Users/Yinggang/Documents/MATLAB/bucky/guess of
zero.jpg');
imwrite(HRimage_zeroGuess, 'C:\Users/Yinggang/Documents/MATLAB/bucky/HR image
of bucky with guess of zeros.jpg');
imwrite(firstImageGuessForHR, 'C:\Users/Yinggang/Documents/MATLAB/bucky/guess
of expanded first LR image.jpg');
imwrite(HRimage_firstImageGuess, 'C:\Users/Yinggang/Documents/MATLAB/bucky/HR
image of bucky with guess of first image.jpg');
imwrite(aveImagesGuessForHR, 'C:\Users/Yinggang/Documents/MATLAB/bucky/guess
of average of expanded LR images.jpg');
imwrite(HRimage_aveImageGuess, 'C:\Users/Yinggang/Documents/MATLAB/bucky/HR
image of bucky with guess of average.jpg');
```

Appendix B

The following is the Matlab code implementing the iterative-back-projection super-resolution algorithm that is called by the main program in Appendix A.

```
function HRimage = IBPSuperresolution(LRimages, displacements, blurDeviation,
guessOfHRImage)

%IBPSUPERRESOLUTION High-resolution image from a set of low-resolution
images.
%   IBPSUPERRESOLUTION is used to reconstruct high-resolution images from a
%   set of low-resolution images from the same scene by iteratively back
%   projecting and updating HR image with a kernel consisting of operators of
%   global pixel displacements, uniform gaussian blurring and under-sampling
%   HR image. This program assumes all LR images have identical size and
%   there are same numbers of LR images along horizontal and vertical
%   directions resulting in same resolution enhancement along either
%   orientation.
%
%   LRimages: a cell array that contains all LR images each of which is
%   represented by grayscale values of all pixels in it as a matrix.
%
%   displacements: a m-by-2 matrix where m is the number of total LR images,
%   containing sub-pixel global translations for all LR images in which the
%   first column represents horizontal displacement while second column
%   represents vertical displacement. The values for all elements must be
%   less than 1 denoting sub-pixel translation.
%
%   blurDeviation: the sigma value, or standard deviation for the gaussian
%   filter applied to all pixels in HR image. Only the surrounding pixels
%   closest to the one applied with this filter are included in
%   calculation. This parameter should be a positive scalar.
%
%   guessOfHRImage: initial guess of HR image in the form of a matrix. It
%   must exactly match the required resolution of HR image in specific
%   applications.

%---------------------------program starts here---------------------------%

% the number of LR images used to reconstruct HR image
numLRimages = numel(LRimages);

% factor of superresoltuion here defined as the times by which the
% resolution of HR image along horizontal or vertical directions. Note:
% this program assumes the resolution enhancement along horizontal and
% vertical directions are the same
superResolveFactor = sqrt(numLRimages);
```

```
% resolution of LR images. Note: all LR images should have identical
% dimensions
LRSize = size(LRimages{1});

% resolution of HR image to be reconstructed
HRSize = superResolveFactor * LRSize;

% total number of pixels in LR and HR images that will be used as the size
% of the vectors after LR and HR images are processed after linear
% transformation, also known as vectorization
numPixelsLR = prod(LRSize);
numPixelsHR = prod(HRSize);

% the kernel function that relates HR image to all LR images consisting of
% global translation, gaussian blurring and down sampling operators
kernel = [];

% vectorize the initial guess of HR image to match the kernel operator
guessOfHRImage = guessOfHRImage(:);

%% pixels of all LR images after vectorization
vectorizedLRimages = [];

for i = 1 : numLRimages
    curLRimage = LRimages{i};
    vectorizedLRimages = [vectorizedLRimages ; curLRimage(:)];
end

%% Uniform blur with gaussian filter

% create a 2D gaussian filter that only affects surrounding pixels

% only affect the adjacent pixels
rangeOfFilterStraight = (-1 : 1);
rangeOfFilterDiagonal = [-sqrt(2) 0 sqrt(2)];

% gaussian filter for horizontal or vertical pixels
gaussianBlurForStraight = exp(-(rangeOfFilterStraight.^2) ./ (2 *
blurDeviation^2));

% gaussian filter for diagonal pixels
gaussianBlurForDiagonal = exp(-(rangeOfFilterDiagonal.^2) ./ (2 *
blurDeviation^2));

% first row and first column for creating toeplitz matrix for blur operator
firstRow = zeros(numPixelsHR, 1);
firstCol = zeros(numPixelsHR, 1);

% assign the values to first row and first column before constructing the
% toeplitz matrix
firstRow(1) = gaussianBlurForStraight(2);
firstCol(1) = firstRow(1);
firstRow(2) = gaussianBlurForStraight(3);
firstCol(2) = gaussianBlurForStraight(1);
```

```
firstRow(1 + HRSize(1)) = gaussianBlurForStraight(3);
firstRow(HRSize(1)) = gaussianBlurForDiagonal(1);
firstRow(2 + HRSize(1)) = gaussianBlurForDiagonal(3);
firstCol(1 + HRSize(1)) = gaussianBlurForStraight(1);
firstCol(HRSize(1)) = gaussianBlurForDiagonal(3);
firstCol(2 + HRSize(1)) = gaussianBlurForDiagonal(1);

% normalize the values in the gaussian blurring kernel
totalValue = sum(firstRow(:)) + sum(firstCol(:)) - firstRow(1);
firstRow = firstRow ./ totalValue;
firstCol = firstCol ./ totalValue;

% create the sparse toeplitz matrix that applies the blur to all pixels in
% the image
diagIndices = [-HRSize(1)-1 -HRSize(1) 1-HRSize(1) -1 0 1 HRSize(1)-1 ...
    HRSize(1) HRSize(1)+1];
diagValuesSingleRow = [firstCol(2 + HRSize(1)) firstCol(1 + HRSize(1))
firstCol(HRSize(1)) ...
    firstCol(2) firstCol(1) firstRow(2) firstRow(HRSize(1)) firstRow(1 +
HRSize(1)) ...
    firstRow(2 + HRSize(1))];
diagValues = repmat(diagValuesSingleRow, numPixelsHR, 1);
blurOperator = spdiags(diagValues, diagIndices, numPixelsHR, numPixelsHR);


%% Down sampling the HR image to match the resolution of LR images

% construct the grid so that the element subscripts are obtained for LR
% images
[LR_XSubscripts, LR_YSubscripts] = meshgrid(1 : LRSize(1), 1 : LRSize(2));

% subscripts for pixels in HR images that will be selected for down
% sampling, the selected pixels are in the position (1, 1) in each
% superResolveFactor-by-superResolveFactor pixels block in the HR image
HR_XSubscripts = superResolveFactor * LR_XSubscripts - superResolveFactor +
1;
HR_YSubscripts = superResolveFactor * LR_YSubscripts - superResolveFactor +
1;

% convert these subscripts into linear indices since the images are
% processed after converting them into column vectors
HR_linearIndicesSelectedForDownSampling = sub2ind(HRSize, HR_XSubscripts,
HR_YSubscripts);
LR_linearIndicesOfEntireImage = sub2ind(LRSize, LR_XSubscripts,
LR_YSubscripts);

% obtain the down sampling matrix
downSamplingOperator = sparse(LR_linearIndicesOfEntireImage,
HR_linearIndicesSelectedForDownSampling, ...
ones(1, numPixelsLR), numPixelsLR, numPixelsHR);

%% Obtain the super-resolution kernel with factors of translation, blur and
downsampling
for i = 1 : numLRimages
```

```
    % Translation of each LR image
    % first row and first column for creating toeplitz matrix for
    % translation operator
    firstRow = zeros(1, numPixelsHR);
    firstCol = zeros(1, numPixelsHR);

    % translation distance in horizontal direction
    horizonTranslation = displacements(i, 1);

    % translation distance in vertical direction
    verticalTranslation = displacements(i, 2);

    % construct the linear interpretation of global translation effect
    firstRow(1) = 1 - (horizonTranslation + verticalTranslation)/2;
    firstCol(1) = firstRow(1);
    firstRow(2) = verticalTranslation / 2;
    firstRow(1 + HRSize(1)) = horizonTranslation / 2;

    % create a sparse toeplitz matrix to apply the translation to all
    % pixels in the image
    diagIndices = [0 1 HRSize(1)];
    diagValuesSingleRow = [firstCol(1) firstRow(2) firstRow(1+HRSize(1))];
    diagValues = repmat(diagValuesSingleRow, numPixelsHR, 1);
    curTranslationOperator = spdiags(diagValues, diagIndices, numPixelsHR,
numPixelsHR);

    % combine translation, blurring and down sampling operators to get the
    % kernel relating LR images and HR image
    curImageKernel = downSamplingOperator * blurOperator *
curTranslationOperator;
    kernel = [ kernel ; curImageKernel ];
end

%% Iterative Back Projection (IBP) process to reconstruct HR image

% set a maximum number of iterations to restore the HR image regardless of
% final mean squared error (MSE).
maxIBPtimes = 1000;

% HR image updated in each iteration starting with the initial guess
curHRimage = guessOfHRImage;

% set a maximum tolerable mean squared errors between the real LR images and
% back-projected LR images from the final HR image
maxIBPMSE = 0.05;

% set a maximum tolerable squared discrete Laplacian transformation of the
% final HR image that limits the overall pixel values varying rapidly
% across the HR image
maxSquaredLaplacian = 1;

% a constant coefficient for the incremental update of HR image with IBP
% error in each iteration
cIBP = 0.01;
```

```
% a constant coefficient for the incremental update of HR image with
% Laplacian operator
cLap = 0.1;

% IBP process begins
for i = 1 : maxIBPtimes

    % Laplacian smoothness
    curLaplacian = del2(curHRimage);

    % total squared Laplacian values for all pixels in HR image
    curSquaredLaplacian = curLaplacian' * curLaplacian;

    % limit the squared Laplacian value for the HR image so as it is not
    % greater than maximum value allowed
    while curSquaredLaplacian > maxSquaredLaplacian
        curHRimage = curHRimage + cLap * curLaplacian;
        curLaplacian = del2(curHRimage);
        curSquaredLaplacian = curLaplacian' * curLaplacian;
    end

    % obtain all the back-projected LR images
    curBP_LRimages = kernel * curHRimage;

    % error between the real LR images and back-projected LR images from
    % the HR image applied with the kernel
    curIBPError = vectorizedLRimages - curBP_LRimages;

    % sum of squared errors between the pixels in real LR images and
    % back-projected LR images
    curIBPSquaredError = curIBPError' * curIBPError;

    % mean squared error between the pixels in real LR images and
    % back-projected LR images
    curIBPMSE = curIBPSquaredError / (vectorizedLRimages' *
vectorizedLRimages);

    % the process is done if and only if both the squared error between the
    % real and computed LR images, and the Laplacian value are limited to
    % their maximum values allowed, respectively. The latter condition has
    % been checked earlier in the while loop, therefore it does not need to
    % be checked in this if statement
    if curIBPMSE <= maxIBPMSE
       break
    end

    % update the current HR image
    curHRimage = curHRimage + cIBP * kernel' * curIBPError;
end

% obtain the vectorized HR image
vectorizedHRimage = curHRimage;
```

```
% obtain the final HR image
HRimage = reshape(vectorizedHRimage, HRSize);

end
```